



Ana Carolina Guimarães Alves Rebello

**Rheological study of ethane gas hydrates
formation from water-in-model oil emulsion in
a high pressure cell**

Tese de Doutorado

Thesis presented to the Programa de Pós-graduação em Engenharia Mecânica do Departamento de Engenharia Mecânica da PUC-Rio in partial fulfillment of the requirements for the degree of Doutor em Engenharia Mecânica.

Advisor : Prof. Mônica Feijó Naccache
Co-advisor: PhD. Gustavo Alonso Barrientos Sandoval

Rio de Janeiro
April 2023



Ana Carolina Guimarães Alves Rebello

**Rheological study of ethane gas hydrates
formation from water-in-model oil emulsion in
a high pressure cell**

Thesis presented to the Programa de Pós-graduação em Engenharia Mecânica do Departamento de Engenharia Mecânica da PUC-Rio in partial fulfillment of the requirements for the degree of Doutor em Engenharia Mecânica. Approved by Examination Committee.

Prof. Mônica Feijó Naccache

Advisor

Departamento de Engenharia Mecânica – PUC-Rio

PhD. Gustavo Alonso Barrientos Sandoval

Co-advisor

Departamento de Engenharia Mecânica – MINES

Prof. Roney Leon Thompson

Departamento de Engenharia Mecânica – UFRJ

Prof. Cezar Otaviano Ribeiro Negrão

Departamento Acadêmico de Mecânica – UTFPR

Prof. Paulo Roberto de Souza Mendes

Departamento de Engenharia Mecânica – PUC-Rio

Prof. Ricardo Jorge Espanhol Andrade

Departamento de Engenharia Mecânica – UPM

Rio de Janeiro, April the 26th, 2023

All rights reserved.

Ana Carolina Guimarães Alves Rebello

Graduou-se em Engenharia de Recursos Hídricos e do Meio Ambiente pela Universidade Federal Fluminense (UFF). Participou da empresa junior Agrha Consultoria. Fez pós graduação e especializou-se em Engenharia de Segurança do Trabalho pela Universidade Federal Fluminense (UFF), onde escreveu um projeto sobre Análise de Risco em um tipo de ambiente de trabalho. Depois entrou para o programa de Mestrado em Engenharia de Biosistemas pela Universidade Federal Fluminense (UFF) e estudou os principais acidentes na indústria de petróleo e gás, com foco nas questões ambientais.

Bibliographic data

Guimarães Alves Rebello, Ana Carolina

Rheological study of ethane gas hydrates formation from water-in-model oil emulsion in a high pressure cell / Ana Carolina Guimarães Alves Rebello; advisor: Mônica Feijó Naccache; co-advisor: Gustavo Alonso Barrientos Sandoval. – Rio de Janeiro: PUC-Rio, Departamento de Engenharia Mecânica, 2023.

v., 101 f: il. color. ; 30 cm

Tese (doutorado) - Pontifícia Universidade Católica do Rio de Janeiro, Departamento de Engenharia Mecânica.

Inclui bibliografia

1. Engenharia Mecânica – Teses. 2. Engenharia Química – Teses. 3. Hidratos de etano;. 4. Reologia;. 5. Célula de alta pressão;. 6. Preocupação offshore;. 7. Emulsões;. 8. Reômetro rotacional.. I. Naccache, Mônica. II. Alonso B. Sandoval, Gustavo. III. Pontifícia Universidade Católica do Rio de Janeiro. Departamento de Engenharia Mecânica. IV. Título.

CDD: 621

Acknowledgments

First, I would like to say how much doing a PhD has been one of the biggest professional challenges of my life so far. I never thought of doing a postgraduate course at this level and especially getting out of my comfort zone. I have a degree in environmental engineering from Universidade Federal Fluminense and entering a doctorate in mechanical engineering was a great adventure. Going through the qualification was psychologically very difficult for me but with a lot of effort, study and support I managed. From the qualification, a new professional emerged and I am very grateful to the doctorate for this strength and feeling that we are capable of anything. Today I am here still dreaming alive that I ventured into a PhD.

If I am here today writing this text, it's thanks to God and to all my guides who didn't let me give up even in those most difficult moments and anxiety crises. Faith provided me with one of the greatest pillars I needed to go through this challenge of pure study and dedication for more than 4 years.

I would like to thank my family. Thank you to my mother Selma, my father Luis, my sister Juliana, my grandmother, my lucky charm Dona Maria and my little dog Chiquinho for all your love. What would become of me in this process if it weren't for you supporting me and not letting me give up? Without you absolutely none of this would be possible. If I'm here today, at this stage, it's because you certainly played a fundamental part in this whole process. I love each one of you very much. Thank you so much for everything always. This achievement is yours.

Friendship also makes a lot of difference in these processes. A friendly shoulder, advice, a smile, a word of support, a hug boosts my world. Thank you to my great friend Marina Ribeiro for having entered my life precisely in my doctorate. Thank you for opening my eyes and for going through the pandemic and qualifying period with me. Hours of hard study, laughter over the days and exchange of ideas were so worth it, look where we are now. My eternal gratitude. I also thank my friend Márcio, my best friend Jéssica Duarte, my great friend Thais Ribeiro, Claudia Nunes, my dear friends from school and my friends for life.

Professor Mônica Naccache, thank you very much. I remember as if it were today, the day I went to her room to ask about her work in the laboratory, her research and work topics. Deciding to continue in the area of hydrates was one of the best choices I could have made. Thank you Monica for accepting me as a PhD student in your rheology laboratory, thank you for your time, your teachings, your dedication, advice and empathy. My gratitude is also dedicated to Gustavo Alonso for all the exchanges he had with me over the years. I am

very grateful for having given me his knowledge about hydrates formed under high pressure, for having taught me how to use the rheometer and the pump. Thank you so much for all the partnership and for the dialogues throughout the days and routines. I thank Priscila, Isabela, Jô, Yago, and all the colleagues at the PUC-Rio Rheology laboratory who crossed my path on this journey.

My complete gratitude to the institution PUC-Rio for providing the possibility of studying a postgraduate course of extreme excellence completely free of charge. I never thought about that possibility and I am extremely happy to live it. I applied for a position in the Graduate Program in Mechanical Engineering without really believing that it was possible. I received an email, it was the 13th of a month, saying that I had been approved and with a scholarship. What happiness. Thank you.

And all this work that was carried out would not be possible without the supporters, sponsors. Many thanks to the institution CAPES for the financial support and thanks to Petrobras for funding the research in Brazil and for all the meetings, exchanges of knowledge and advice throughout the realization of this work. Thanks to Adriana Teixeira and Leonardo Valim for their availability and collaboration. Thanks to Professor Amadeu Sum for all the partnership and exchange of knowledge.

To all those who helped me during the Ph.D journey, my deep gratitude. This study was financed in part by the Coordenação de Aperfeiçoamento de Pessoal de Nível Superior - Brasil (CAPES) - Finance Code 001.

Abstract

Guimarães Alves Rebello, Ana Carolina; Naccache, Mônica (Advisor); Alonso B. Sandoval, Gustavo (Co-Advisor). **Rheological study of ethane gas hydrates formation from water-in-model oil emulsion in a high pressure cell.** Rio de Janeiro, 2023. 101p. Tese de doutorado – Departamento de Engenharia Mecânica, Pontifícia Universidade Católica do Rio de Janeiro.

In the oil and gas industry, the stoppage of the production and transportation flowlines caused by the deposition of organic and inorganic compounds yields huge financial losses and environmental concerns. One of the most common and critical inorganic deposition is related with gas hydrates, which are crystalline water-based solids, physically similar to ice, formed in conditions of high pressure and low temperatures. Due to the worrying facts, phenomena related to hydrates, as formation, dissociation, and forms to its mitigation have been studied for years by researchers. In this work, experiments were carried out to analyze ethane gas hydrate formation in water-in-model oil emulsions, through a rheological analysis based on the variation of pressure, shear rate and water volume fraction, and using the vane and concentric cylinder geometries. High pressure time sweep tests were performed, and the results were presented through viscosity and pressure curves. The amount of water converted to hydrate was also estimated through the equation of state and related to the viscosity of the hydrate slurries formed. The results obtained showed that the induction period was reduced by increasing the subcooling, water cut, and shear rate. The higher the water volume fraction, the higher the level reached by viscosity when hydrate formation is identified. The relative viscosity after hydrate formation was studied. This knowledge provided a more effective understanding of some differences observed between the two geometries. And to complement the study, shear rate ramps were performed showing similarities between results with concentric cylinders but differences with vane. Both geometries, vane and concentric cylinders, seem to be adequate to study hydrate formation and similar qualitative results were obtained.

Keywords

Ethane Hydrates; Rheology; High-Pressure Cell; Offshore issue; Emulsions; Rotational rheometer.

Resumo

Guimarães Alves Rebello, Ana Carolina; Naccache, Mônica; Alonso B. Sandoval, Gustavo. **Estudo reológico da formação de hidrato de gás de etano a partir de emulsão modelo água em óleo em uma célula de alta pressão**. Rio de Janeiro, 2023. 101p. Tese de Doutorado – Departamento de Engenharia Mecânica, Pontifícia Universidade Católica do Rio de Janeiro.

Na indústria de óleo e gás, a paralisação da produção e do transporte nas linhas de fluxo causadas pela deposição de compostos orgânicos e inorgânicos rendem enormes perdas financeiras e preocupações ambientais. Um dos fatores mais comuns e críticos na deposição orgânica está relacionado com a formação de hidratos de gás, que são sólidos cristalinos de base aquosa, fisicamente semelhantes ao gelo, formados em condições de alta pressão e baixas temperaturas. Devido a esses fatos preocupantes, fenômenos relacionados aos hidratos, como formação, dissociação e formas de mitigação, vêm sendo estudados há anos por pesquisadores. Neste trabalho foram realizados experimentos para analisar a formação de hidrato de gás de etano em emulsões água em óleo, através de uma análise reológica baseada na variação de pressão, taxa de cisalhamento e fração de volume de água, e usando as geometrias vane e de cilindros concêntricos. Testes de varredura de tempo de alta pressão foram realizados, e os resultados foram apresentados através de curvas de viscosidade e pressão. A quantidade de água convertida em hidrato também foi estimada através da equação de estado e relacionada com a viscosidade das pastas de hidratos formadas. Os resultados obtidos mostram que o período de indução foi reduzido pelo aumento do subresfriamento, corte de água e taxa de cisalhamento. Quanto maior a fração de volume de água, maior o nível atingido pela viscosidade quando identificada a formação de hidratos. A viscosidade relativa, após a formação do hidrato, foi estudada. Esse conhecimento proporcionou uma compreensão mais efetiva de algumas diferenças observadas entre as duas geometrias. E para complementar o estudo, foram realizadas rampas de taxa de cisalhamento mostrando semelhanças entre os três resultados com cilindros concêntricos, mas diferenças entre os resultados com geometria vane. Ambas as geometrias, vane e cilindros concêntricos, foram consideradas adequadas para estudar a formação de hidratos e resultados qualitativos semelhantes foram obtidos.

Palavras-chave

Hidratos de etano; Reologia; Célula de alta pressão; Preocupação offshore; Emulsões; Reômetro rotacional.

Table of contents

1	Motivation	15
2	Literature Review	19
2.1	Gas hydrate history and formation	19
2.2	Hydrate nucleation process	23
2.3	Induction time and metastability	25
2.4	Hydrate inhibitors	26
2.4.1	Thermodynamic hydrate inhibitors (THIs)	27
2.4.2	Kinetic hydrate inhibitors (KHIs)	28
2.4.3	Anti-Agglomerants (AAs)	29
2.5	Experimental methods of rheology	30
2.5.1	Rotational rheometer	30
2.6	Studies of gas hydrates	31
2.7	Objectivies	39
3	Experimental Methods	40
3.1	Materials	40
3.2	Emulsification and microscopy	41
3.3	Rheometry features and pressure cell	46
3.4	High-pressure system	48
3.5	Experimental procedure	49
3.6	Amount of water converted to hydrate	51
4	Results and discussion	53
4.1	Effect of Span80	53
4.2	Influence of rheological parameters on hydrates formation	56
4.2.1	Effect of pressure with concentric cylinder geometry	56
4.2.2	Effect of pressure with vane geometry	58
4.2.3	Effect of shear rate with concentric cylinders geometry	60
4.2.4	Effect of shear rate with vane geometry	63
4.2.5	Effect of water volume fraction with concentric cylinders geometry	65
4.2.6	Effect of water volume fraction with vane geometry	66
4.3	Amount of water converted to hydrate	67
4.3.1	Influence of pressure	67
4.3.2	Influence of shear rate	69
4.3.3	Influence of water volume fraction	71
4.4	Correlation between relative viscosity and the amount of water converted to hydrates	73
4.5	Rheological behavior with shear rate ramp	75
4.5.1	Concentric cylinders tests	76
4.5.2	Vane geometry tests	81
5	Final remarks	86

6	Future work	89
7	Bibliography	90

List of figures

Figure 1.1	Gas hydrate that has formed in a pipeline during an operation. Taken from Jozian and Vafajoo [1].	15
Figure 1.2	Example of Carbon dioxide guest molecule (represented by the green coloring) on the sI clathrate hydrate structure. Taken from Izquierdo-Ruiz et. al., [2].	16
Figure 1.3	Gas hydrate (white material) formed beneath mussel-coated carbonate rock on the seafloor of the Gulf of Mexico. Taken from Levin et. al., [3].	17
Figure 2.1	Structural types of gas hydrates characterized using neutron or X-ray diffraction techniques: a) cage shapes, b) sI, c) sII, and d) sH of gas hydrate structures. Adapted from Kirchner et. al., [4].	20
Figure 2.2	Illustration of the entire hydrate formation process. Taken from Qin et. al., [5].	21
Figure 2.3	Formation over time of a thin hydrate film in a droplet of water-in-model oil emulsion. Adapted from Taylor [6].	21
Figure 2.4	Hydrate growth model description: a) water droplet in oil, b) nucleation site in the water-oil interface. For static systems: c) tangential growth, and d) hydrates form as shells. For dynamic systems: e) relative motion between crystal and droplet causes no preferential growth direction, and f) evolution of the porous structure of the hydrates. Taken from Bassani et. al., [7].	22
Figure 2.5	Particles remain together for enough time and crystalline bridges consolidate the particles into an agglomerate. Adapted from Bassani et. al., [8].	23
Figure 2.6	Depiction of interaction of particle during collision with the flowline wall: a) water layer can contour the particle, b) capillarity bridges between the wall and particle, and c) stickiness of the particle to the wall. Adapted from Bassani et. al., [8].	23
Figure 2.7	Gibbs free energy barrier of hydrate nucleation and critical nuclei size as a function of clusters radius. Adapted from Ke et.al., [9].	24
Figure 2.8	Non-hydrate, metastable, and hydrate regions. Adapted from Ke et.al., [9].	26
Figure 2.9	Hydrate formation phases as a function of gas consumption and time. Taken from Warriar et.al., [10].	27
Figure 2.10	KHIs example structures. Taken from Wang and Lang, [11].	29
Figure 2.11	Rotational rheometric measurement systems: a) concentric cylinder, b) parallel-plate, and c) cone-and-plate. Taken from Boger [15].	31
Figure 2.12	Modified bob (P = pitch, d = depth, all dimensions are in mm). Taken from Pandey et. al., [16].	33

- Figure 2.13 a) Pressure, b) fraction of water converted to hydrate and, c) viscosity over time as hydrates form in water-in-mineral oil emulsions at 0 °C, 1500 of psig initial pressure, and 100 s⁻¹. Taken from Webb et. al., [17]. 34
- Figure 2.14 Schematic of the experimental setup: (a) Double-threaded modified bob geometry used for the rheological measurements of hydrate and (b) dimensions of the modified bob geometry. Taken from Nair et. al., [18]. 35
- Figure 2.15 Simulation of a vane geometry using the (a) 3D view of the impeller, (b) 3D view of the geometry, and (c) 2D view. Method taken from Nazari et. al., [19]. 36
- Figure 2.16 Tangential velocity magnitudes (m/s) at 10 rpm for the fluid with viscosity: (a) 98 mPa s, (b)12,000 mPa s. Taken from Nazari et. al., [19]. 37
- Figure 2.17 Top and side cutting planes showing isovalues of the velocity magnitude for a gap of 5 mm. Taken from Rabia et. al., [20]. 37
- Figure 2.18 Effect of ILs on gas hydrate induction time in comparison with pure water. Standard deviations are shown for each condition. Taken from Maiti et. al., [21]. 38
- Figure 3.1 Surfactant: a) structure and b) parts interaction with the oil and water, which in this case is a water-in-model oil emulsion. Adapted from Kale e Deore, [22] and Myers et. al., [23]. 42
- Figure 3.2 Molecular structure for surfactants: (a) sorbitan monooleate (Span 80); (b) sodium di-2-ethylhexylsulfosuccinate (AOT). Taken from Kale e Deore, [24]. 43
- Figure 3.3 Cross section of a rotor-stator type stirrer. Taken from Fujii et. al., [25]. 44
- Figure 3.4 Appearance of the prepared water-in-model oil emulsion. 45
- Figure 3.5 Micrographs and histograms of the 30% water-in-model oil emulsions used with the vane (A) and the concentric cylinder measuring system (B). 47
- Figure 3.6 Geometries used in the experiments: a) concentric cylinders and b) vane. 47
- Figure 3.7 Diagram of the high pressure cell employed in this study. Figure taken from Sandoval et. al., [26]. 48
- Figure 3.8 Representation of the high-pressure system used to conduct the experiments. Gas reservoir (1), control panel (2), syringe pump (3), pressure cell (4), rheometer (5), needle valve, (6) and thermostatic bath (7). 49
- Figure 3.9 Example of a test performed with an initial pressure of 26 bar, 30% water volume fraction, shear rate of 700 s⁻¹ and with concentric cylinder geometry. 51
- Figure 4.1 Effect of Span 80 concentration (wt%) on hydrate formation: (a) viscosity *versus* time, and (b) pressure *versus* time. Tests performed with 30% WVF, initial pressure of 35 bar, and shear rate $\dot{\gamma} = 700 \text{ s}^{-1}$. 54

- Figure 4.2 Effect of pressure on hydrate formation: (a) viscosity *versus* time, and (b) pressure *versus* time. Run 1 and run 2 represent two tests made with the same conditions, and different samples. Pressure of 25, 30, and 35 bar were represented by gray/losangle, blue/triangle down, and green/circle lines, respectively. The temperature was represented by the red curve. 57
- Figure 4.3 Effect caused by the subcooling on hydrate formation: (a) viscosity *versus* time, and (b) pressure *versus* time. Tests performed with 30% WVF and 40 s^{-1} . 58
- Figure 4.4 Hydrate block (a) being pulled out of the cell and (b) hydrate removing from the cell using the vane geometry. 59
- Figure 4.5 Repeatability tests of subcooling on hydrate formation: (a) viscosity *versus* time, and (b) pressure *versus* time. Tests performed with 30% WVF and 40 s^{-1} . 60
- Figure 4.6 Effect caused by the shear rate on hydrate formation: (a) viscosity *versus* time, and (b) pressure *versus* time. Tests performed with 30% WVF and initial pressure of 31 bar. 61
- Figure 4.7 Repeatability tests with shear rate variation: (a) viscosity *versus* time, and (b) pressure *versus* time. Tests performed with 30% WVF and initial pressure of 31 bar. 62
- Figure 4.8 Behavior of: (a) viscosity *versus* time and (b) pressure *versus* time for different shear rates. Tests performed with 30% WVF, and pressure of 31 bar. 63
- Figure 4.9 (a) Variation of viscosity *versus* time, and (b) pressure *versus* time for different water volume fraction. Pressure of 31 bar, and shear rate of 800 s^{-1} . 65
- Figure 4.10 Effect caused by the water volume fraction on hydrate formation: (a) viscosity *versus* time, and (b) pressure *versus* time. Tests performed with a shear rate of 32 s^{-1} , and initial pressure of 31 bar. 66
- Figure 4.11 Effect of the pressure on the water converted to hydrate. The pressure used was 30 bar with 30% of water cut in the emulsion and with a shear rate of 700 s^{-1} . 68
- Figure 4.12 Water converted to hydrate for different pressures using the vane rotor. The water cut used was 30% and the shear rate applied was 40 s^{-1} . 69
- Figure 4.13 Water converted to hydrate for different shear rates. The pressure used was 31 bar with 30% of water cut in the emulsion. 70
- Figure 4.14 Water converted to hydrate for different shear rates. The water cut used was 30% and the pressure applied was 31 bar. 71
- Figure 4.15 Water converted to hydrate for different amounts of water in the emulsion. The pressure used was 31 bar and the shear rate applied was 800 s^{-1} . 72
- Figure 4.16 Water converted to hydrate for different emulsion compositions. The pressure used was 31 bar and the shear rate applied was 32 s^{-1} . 73

Figure 4.17 Relative viscosity <i>versus</i> water converted to hydrates for differents shear rates. For each shear rate a variation of water volume fraction was applied. Pressures of 31 bar.	74
Figure 4.18 Relative viscosity <i>versus</i> water converted to hydrates for differents shear rates. For each rate a variation of water cut was applied. Pressures of 31 bar.	75
Figure 4.19 Shear rate ramp with initial rate of 800 s^{-1} varying as a function of time.	76
Figure 4.20 Shear rate ramp with initial rate of 750 s^{-1} varying as a function of time.	78
Figure 4.21 Shear rate ramp with initial rate of 700 s^{-1} varying as a function of time.	79
Figure 4.22 The experimental points (triangular) and the curves fitting of power-law. The blue and red color represents the shear rates decreases [A] and the shear rates increases [B] to 800 s^{-1} , respectively.	80
Figure 4.23 The experimental points (circular) and the curves fitting of power-law. The blue and red color represents the shear rates decreases [A] and the shear rates increases [B] to 750 s^{-1} , respectively.	80
Figure 4.24 The experimental points (quadrate) and the curves fitting of power-law. The blue and red color represents the shear rates decreases [A] and the shear rates increases [B] to 700 s^{-1} , respectively.	81
Figure 4.25 Shear rate ramp with initial rate of 30 s^{-1} and with 2 hours of a period time between rates.	82
Figure 4.26 Shear rate ramp with initial rate of 30 s^{-1} and with 4 hours of a period time between rates.	83
Figure 4.27 Shear rate ramp with initial rate of 32 s^{-1} and with 4 hours of a period time between rates.	84

List of tables

Table 3.1 Mean droplet diameter of the emulsions with the standard deviation (in parenthesis).	46
Table 4.1 Power law parameters obtained by curve fitting of experimental curves.	81

1

Motivation

The oil and gas industry stands out for being a globalized activity and for presenting an intensive generation of capital. Several segments depend on this market, such as fuel, plastics, fertilizers, rubber, medicines, and others. Due to this, petroleum and gas are main products internationally traded. Brazil, which is considered a high potential of oil producer, has about 95% of its production derived from the subsea wells, located in deep and ultra-deep waters. These, deep and ultra-deep water depths are defined as those situated, respectively, between 300 m and 1000 m, and above 1000 m [27]. In the deep ocean, the use to transport the oil and gas are usually subjected to conditions of high pressures and low temperatures [28]. Such a thermodynamic condition increase the possibility of formation and agglomeration of gas hydrates into the production lines, see Fig.1.1. The formation of hydrates is one of the major concerns in the oil industry as it can cause production stoppages, wich renders financial losses, material and environmental damage, and others. Gas hydrates are crystalline solids composed of water and gas. The gas molecules (guests) are trapped in water cavities (host) that are composed of hydrogen-bonded water molecules [29] (see Fig.1.2).



Figure 1.1: Gas hydrate that has formed in a pipeline during an operation. Taken from Jozian and Vafajoo [1].

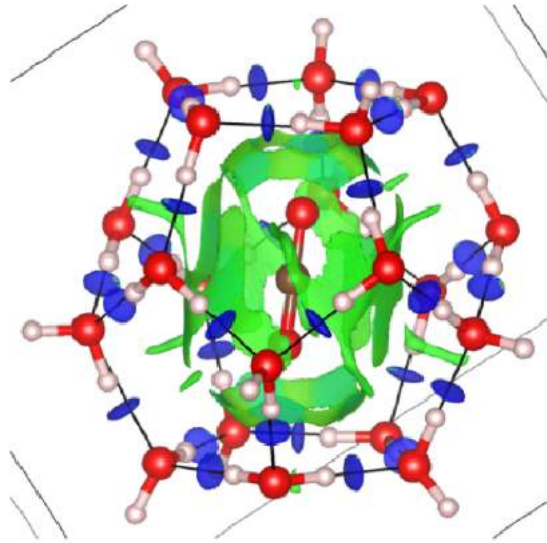


Figure 1.2: Example of Carbon dioxide guest molecule (represented by the green coloring) on the sI clathrate hydrate structure. Taken from Izquierdo-Ruiz et. al., [2].

Other events can occur which hinder or fully stop flow in the pipeline including wax precipitation, scale formation, asphaltene precipitation, and sand deposition. Paraffins (wax) can precipitate during crude oil production operations when the oil is cooled because of heat losses to the surroundings [30]. On the other hand, the asphaltene is the heaviest and most polar constituent of crude oil and is soluble in aromatic fluids and insoluble in alkanes [31]. The definition of asphaltene as a solubility class does not only account for crude oil aromatic fraction but also compounds that aggregates causing problems and possible production stoppages in the oil and gas pipelines [32]. Among all these phenomena, hydrates formation occurs much more rapidly than the others, so it can be considered as the most critical of all [28].

In addition to the motivation with a focus on the oil and gas industry, the hydrate is still widely studied due to its energy recovery, gas storage/transportation and climate change. When small (0.9 nm) hydrocarbon guest molecules are engaged in hydrates, with typically one molecule per cavity, the guests are separated approximately 0.5 nm by the water cages. So the main point is that the energy density in hydrates is approximately the same as that of a compressed gas, that is, less than the energy density of liquefied natural gas (LNG) [33]. Kvenvolden et. al., [34] suggest that the amount of energy in hydrates is equivalent to twice that of all other fossil fuels combined. Most of the natural-gas-containing hydrates are in the ocean bottom, and although production of gas from such deeplying hydrates is now too expensive, it is

likely that within the next two decades we will tap that fuel source to meet growing energy demands. Most of the natural gas hydrates around the world are biogenic, that is, the guest gas comes from bio-degraded plant and animal matter that have been buried in the sea floor at low temperature over long periods [35]. In addition to forming in a natural way, natural gas hydrates provide unique gas storage properties because the hydrates can contain 150 – 180 v/v (standard temperature and pressure) of gas [36]. Using the storage properties of natural gas in hydrates, natural gas storage and transportation can be more secure than liquefied natural gas or pipeline transportation. For a medium or small-scale natural gas field where it is not appropriate to use liquefied natural gas or pipeline transportation, natural gas hydrates become a more economical solution. For a natural gas hydrate storage and transportation process, the most important step is the formation of hydrates, for which the key problems are hydration rate and storage capacity. Higher hydration rate can reduce operation costs, and larger storage capacity can decrease capital equipment requirements [37].

But when the hydrate is formed by methane gas certain climate concerns arise. Gas hydrate is widespread in the sediments of marine continental margins and permafrost areas (see Fig.1.3), locations where ocean and atmospheric warming may perturb the hydrate stability field and lead to release of the sequestered methane into the overlying sediments and soils.



Figure 1.3: Gas hydrate (white material) formed beneath mussel-coated carbonate rock on the seafloor of the Gulf of Mexico. Taken from Levin et. al., [3].

Methane and methane-derived carbon that escape from sediments and soils and reach the atmosphere could exacerbate greenhouse warming.

Appropriate evaluation of the two sides of the climate-methane hydrate synergy requires assessing direct and indirect observational data related to gas hydrate dissociation phenomena and numerical models that track the interaction of gas hydrates/methane with the ocean and/or atmosphere [3,38].

Due to these mentioned facts, hydrates are studied on a large scale in order to control and minimize their possible formations. Thus, this work aims to contribute to the study of the formation of hydrates through an emulsified system with controlled pressure in a high pressure system. The formation of hydrates and their behavior were analyzed through the variation of parameters such as subcooling, shear rate, and water cut variation. The experiments were carried out using two rheometric geometries that provide a comparison of the results obtained in a qualitative way. The droplet size of the prepared emulsions was also verified through the use of a microscope, and the amount of water converted into hydrates was also determined using the equation of state. It was also possible to make a relationship between the steady-state viscosities, and with the amount of water that was converted into hydrates. The shear rates ramps were also performed for the hydrate slurries and the rheological results were correlated with relative viscosity, and the amount of water converted into hydrate.

The gas chosen to work with was ethane because it is a gas that allows the formation of hydrates at low pressures in laboratory scale and in the literature there is a greater study applied to methane gas. Thus, bringing the study of rheology applied to ethane gas provides greater innovation in the study of hydrate formed under high pressure. The data that were raised in this study provide a strong application of knowledge to the industry. The motivation also contemplates this possibility of providing the industry with new learning, concepts and points of view on the formation of hydrates.

The thesis is organized as follows: initially, in chapter 2, a literature review is carried out addressing the history of the hydrates phenomenon. The main hydrate inhibitors, rheology, the hydrates slurry, the main studies already carried out on the formation of gas hydrates, and the main objectives are also covered. In chapter 3, materials, the high pressure system used, and the experimental procedure are presented. In chapter 4, the main results are presented for both geometries, concentric cylinders and vane rotor. The conclusion and the main relevance of the results are discussed in Chapter 5. Finally, suggestions for futures works are described in Chapter 6.

2

Literature Review

In this chapter, some concepts and a literature review about hydrates will be discussed. At the end, the objectives of this thesis will be presented.

2.1

Gas hydrate history and formation

According to Sloan et. al., [29] historically the discovery of the gas hydrate can be divided into three important periods. The first period, in 1810, refers to the phase where the scientific academy was curious to study the transformation into solid from a mixture of water and gas but having no idea what that mixture represented, how it was formed and dissociated. The second period in 1934 already includes a phase where artificial hydrates were generated for study. So the mixture that was not understood could be reproduced at laboratory scales. And the third period, which is from 1960, was related to the discovering of hydrate formation. Hammerschmidt in 1934 reported the observation of hydrates formation in a natural gas transportation system in a *Industrial and Engineering Chemistry* journal [39]. The detection of hydrates in pipelines was a milestone marking both the importance of hydrates to industry and the beginning of the modern research era [39]. From this milestone, the study of hydrates was emphasized to avoid the damage they can cause in the oil and gas industry.

During the research that followed, Von Stackelberg and coworkers summarized two decades of x-ray hydrate crystal diffraction tests studying on a microscopic scale the structure of hydrates, its formation, and if there were differences in its structure [40]. In fact, they discovered two hydrate crystal structures called sI and sII [41]. The existence of a third hydrate structure (sH) was discovered by Ripmeester in 1987. Structure H is formed when the water hydrogen bonds capture both a small molecule such as methane and larger molecules typical of a condensate or an oil fraction [29]. On the other hand, small guest molecules like methane or ethane form sI hydrates whereas larger molecules like propane or iso-butane form sII hydrates [41]. Fig.2.1 shows the common hydrates structures explain below. The sI type comprises two different cage types, a small pentagonal dodecahedral cage, denoted 5^{12} (contains 12

pentagonal faces on the cage), and a large tetrakaidecahedral cage (contains 12 pentagonal and 2 hexagonal faces on the cage). The sII also includes the small 5^{12} cage in addition to a large hexacaidecahedral cage (contains 12 pentagonal and 4 hexagonal faces on the cage). And sH is composed of the small 5^{12} cage, a mid-sized cage (contains 3 square, 6 pentagonal, and 3 hexagonal faces on the cage), and a large icosahedral cage (contains 12 pentagonal and 8 hexagonal faces on the cage) [42–44]. As mentioned by Sloan et. al., [29] all hydrate structures have an asymmetric and spherical cage type of water molecules that are linked together by hydrogen bonds. Each cage contains at most one host molecule held together by scattering forces.

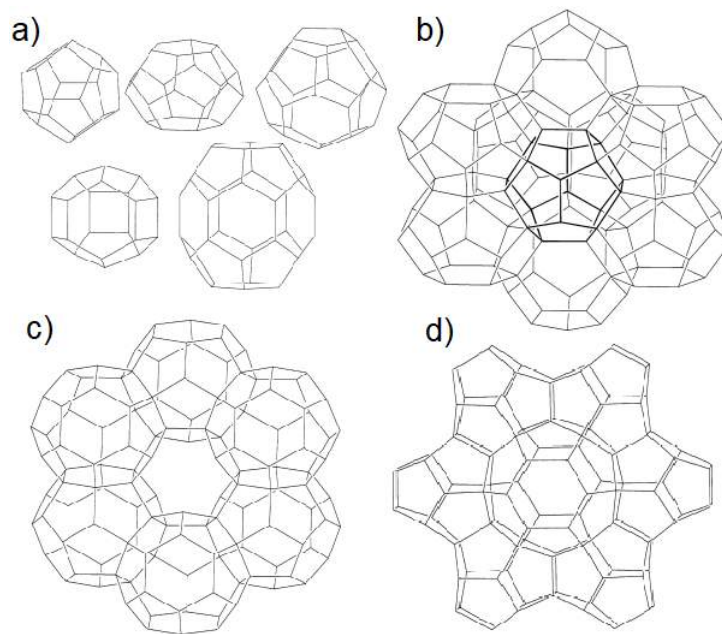


Figure 2.1: Structural types of gas hydrates characterized using neutron or X-ray diffraction techniques: a) cage shapes, b) sI, c) sII, and d) sH of gas hydrate structures. Adapted from Kirchner et. al., [4].

There are two mechanisms of hydrate formation: under static conditions and under dynamic conditions. Under static conditions, the mechanism of hydrate formation for oil-dominated systems basically consists of four steps: (i) water entrainment in the oil phase, (ii) hydrate shell growth at the oil-water interface, (iii) aggregation of shell, and (iv) plug formation [5]. In steps (i) and (ii) the occurrence of nucleation is noted, that is, the formation of a new structure. Hydrate nucleation requires emulsified water droplets, as can be seen in the Fig.2.2. In the production and transportation through the oil pipelines the free water extracted is dispersed with the crude oil when turbulent mixing conditions are observed during operations. These mixtures often form from water-in-model oil emulsions [45]. At the oil-water interface in the droplets present in these emulsions formed, a thin layer of hydrate

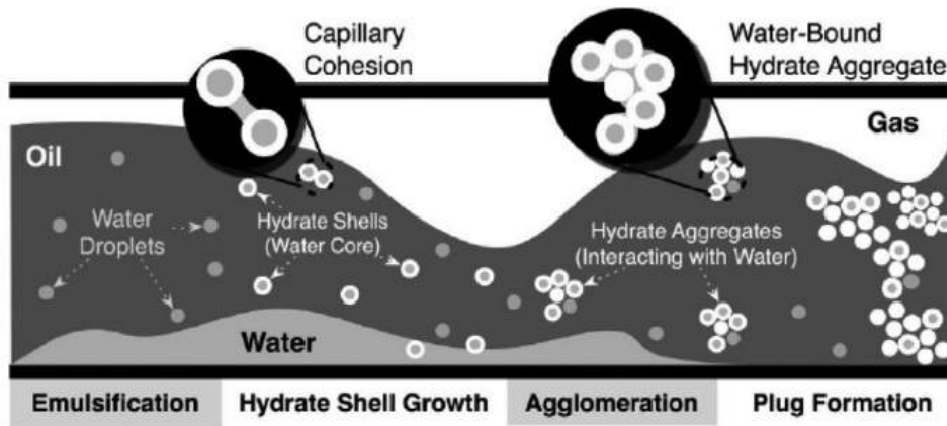


Figure 2.2: Illustration of the entire hydrate formation process. Taken from Qin et. al., [5].

develops, see Fig.2.3. This thin layer grows over time and forms a shell particles. Therefore hydrate nucleation and growth is a kinetic process, meaning that hydrates do not appear instantaneously with the onset of thermodynamically favourable conditions [46].

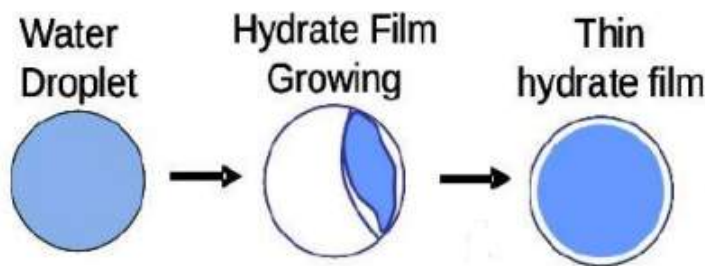


Figure 2.3: Formation over time of a thin hydrate film in a droplet of water-in-model oil emulsion. Adapted from Taylor [6].

It is worth mentioning that the kinetic process has a limitation due to mass or heat transfer process. At a given moment, the hydrate structure will be fully saturated, consuming no more water or gas. This behavior justifies the asymptotic characteristic presented in the results related to the amount of water converted into hydrate which will be shown in the following results. The hydrate structure saturates quickly and then stabilizes [8].

A work that brought new perspectives regarding the formation of hydrates in dynamic conditions and complemented the idea of this study was published by Bassani et. al., [8]. For static systems, growth will predominantly happen in the tangential direction, since axial growth would require either gas diffusion or water permeation through the formed hydrate film (Fig.2.4). This causes the hydrates to form as a shell encompassing the water droplets,

which is currently the hypothesis favored in the literature about gas hydrates growth kinetics in water-in-model oil emulsions [47, 48]. Therefore, it is highly improbable that it occurs in dynamic (nonstatic) systems, since crystal rotation and relative motion will not promote a preferential growth direction, and a shell is not formed [7].

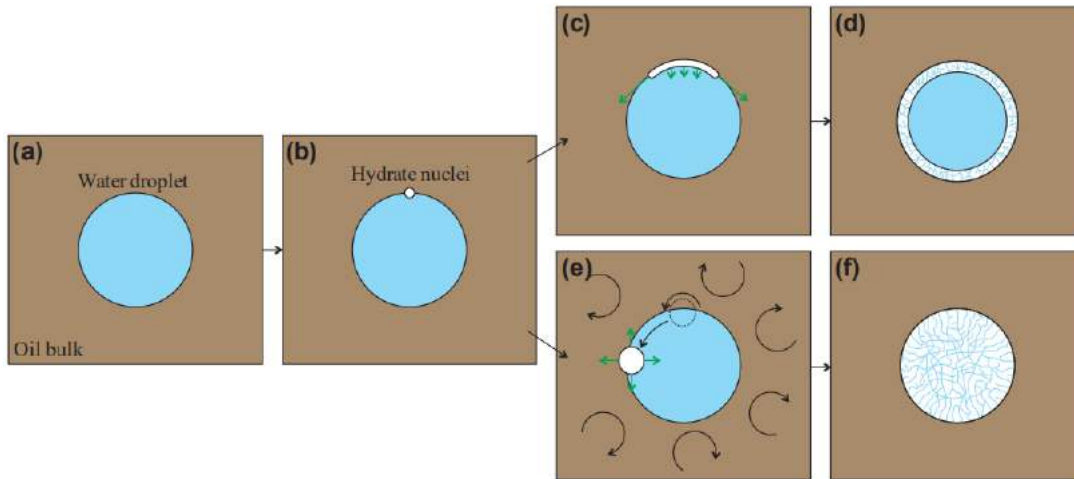


Figure 2.4: Hydrate growth model description: a) water droplet in oil, b) nucleation site in the water-oil interface. For static systems: c) tangential growth, and d) hydrates form as shells. For dynamic systems: e) relative motion between crystal and droplet causes no preferential growth direction, and f) evolution of the porous structure of the hydrates. Taken from Bassani et. al., [7].

The just-formed crystal in dynamic systems, at the water-oil interface, growth in the presence of impurities, ionic forces, and/or high driving forces that induce initial preferential growth directions, and the gas can not reach deeper regions of the formed particles due to heat generation and gas consumption, forming the pores, see Fig.2.4f. The particles of hydrates will therefore form a sponge-like structure. After that, the hydrate particles form will agglomerate during mixture flow rate oscillations [49, 50]. Depending on the morphology of the particles and on the evolution of the porous structure of the hydrates, capillarity bridges may form, causing particles to be sticky, and water may be available at the outer surface of the particles and may promote consolidation of particle - particle (agglomeration), see Fig.2.5, or particle - wall (deposition), see Fig.2.6 [8, 51].

Knowing the main processes through which the hydrate can develop, rheology enters as a study that effectively complements this understanding. In Fig.2.2 and Fig.2.4, the rheology provides an understanding of the flow of the agglomerates, the response of the hydrate particles to an applied stress,

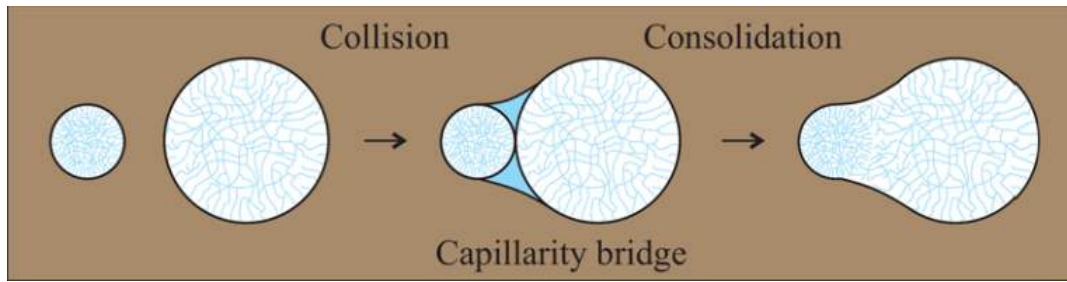


Figure 2.5: Particles remain together for enough time and crystalline bridges consolidate the particles into an agglomerate. Adapted from Bassani et. al., [8].

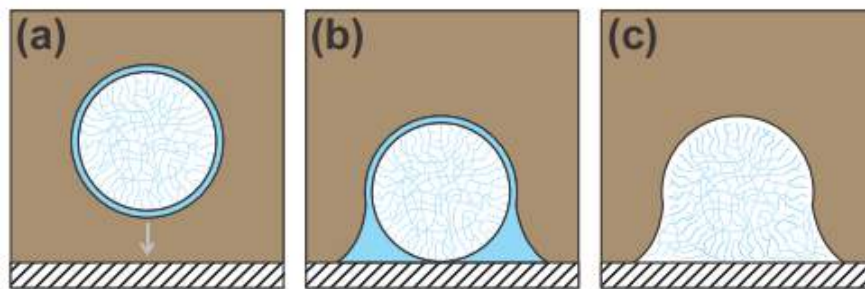


Figure 2.6: Depiction of interaction of particle during collision with the flowline wall: a) water layer can contour the particle, b) capillarity bridges between the wall and particle, and c) stickiness of the particle to the wall. Adapted from Bassani et. al., [8].

the viscosity presented when the agglomerates are dispersed in the mixture of water and oil, the breakage of the agglomerate formed along the drain and others.

2.2 Hydrate nucleation process

As mentioned before, hydrate nucleation is a kinetic process and is a challenging step in understanding the process of crystallization of gas hydrates. In general, nucleation can be either a homogeneous or heterogeneous process. Homogeneous nucleation occurs only in the absence of impurities with only two phases involved: the solute and the nuclei/growing crystal [52]. Homogeneous nucleation is rarely observed in the real world because it is practically impossible not to have the interference of any impurity during the nucleation process. Hydrate nucleation often occurs at a gas–water interface and the phases most probably contain impurities. Foreign surfaces such as a pipe wall or container wall may be involved in the process. Thus, hydrate nucleation in real systems is expected to be a heterogeneous process [10, 53].

Nucleation study is difficult because it occurs at the molecular level and

it is stochastic. By nature, hydrate nucleation is a free energy-driven. Surface excess free energy and volume excess free energy battle against each other when embryos nucleate [54]. These driving force for nucleation caused by free energy are governed by Gibbs equation. This equation is a thermodynamic quantity that seeks to measure the energy attached to a system and can be used to interpret the nucleation behavior of critical cluster size formation and spontaneous growth [55]. Fig.2.7 illustrates the free energy barrier and critical size for hydrate nuclei to become stable particles in terms of Gibbs free energy [9, 56, 57].

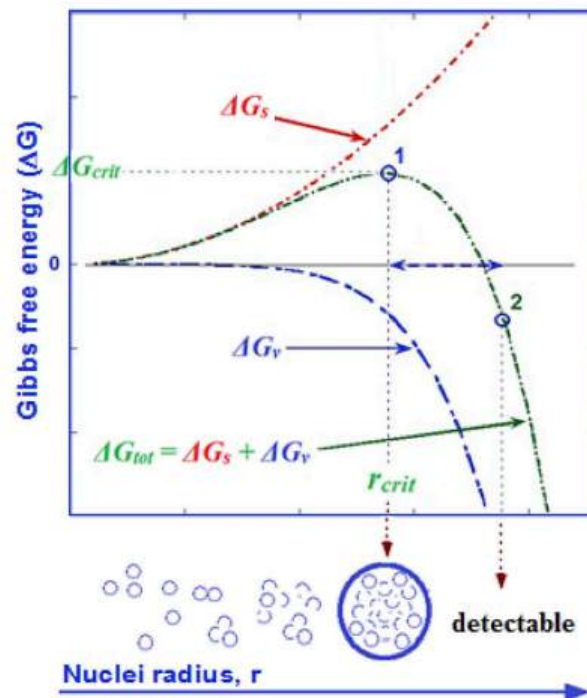


Figure 2.7: Gibbs free energy barrier of hydrate nucleation and critical nuclei size as a function of clusters radius. Adapted from Ke et.al., [9].

As shown in Fig.2.7, the total excess free energy (ΔG_{tot}) is the addition between the surface excess free energy (ΔG_s) and the volume excess free energy (ΔG_v) as a function of cluster radius (r). It is possible to note that the bigger ΔG_s and ΔG_v , the bigger ΔG_{tot} until it reach a peak at point 1. The energy level at this peak is termed the energy barrier for hydrate nucleation (ΔG_{crit}). It corresponds to a specific size of hydrate's nucleus. The nucleus size at this moment is termed the critical size (r_{crit}). Hydrate nuclei with $r \geq r_{crit}$ are energetically favorable to sustain growth and become macroscopically detectable at point 2 [9, 58, 59]. The critical radius has the length scale approximately on the order of 0.001 and 0.01 μm , and agglomerate of 0.1 and 0.01 μm to cause a pressure drop and mixture flow rate oscillations [116].

Assuming a spherical shape for clustering embryos, the excess Gibbs free energy (ΔG_{tot}) takes the following form [59]:

$$\Delta G_{tot} = \Delta G_s + \Delta G_v = 4\pi r^2 \gamma + 4/3\pi r^3 \Delta g_v \quad (2-1)$$

where γ is the surface tension at cluster–liquid interface (tension between the crystal and liquid), and Δg_v is the free energy change per unit volume. By setting the derivative of Eq. 2-1 upon cluster radius (r) to zero, both the critical size and energy barrier could be obtained:

$$r_{crit} = -2\gamma/\Delta g_v \quad (2-2)$$

and

$$\Delta G_{crit} = 4/3\pi\gamma r_{crit}^2 \quad (2-3)$$

The Eq.2-3 shows that a smaller critical size would lead to a lower energy barrier that has to be overcome to form the critical sized clusters. Continuously increasing the supersaturation/subcooling level will eventually cause spontaneous nucleation when the free energy barrier is reduced to be sufficiently small [9, 54, 55].

2.3 Induction time and metastability

The lag between the time when system conditions favour hydrate formation (metastable region) and the appearance of hydrates is known as induction/period time. Due to the stochastic nature of hydrate nucleation process, the induction time of hydrate formation is also stochastic and depends on many parameters, including impurities, driving forces, contact areas, etc [9]. The induction time is a measure of the ability of a supersaturated system to remain in the state of metastability and its occurrence and significance in gas hydrate crystallization have been evidenced and recognized by many authors [52].

The metastable state was defined as “a define equilibrium which is, nevertheless, not the most stable equilibrium at the given temperature” [60]. Jan Lubas [61] proposed that the area of hydrate metastability is the area between the curves of hydrate formation and dissociation (see Fig.2.8). Fig.2.8 shows the lines AA' and BB' called equilibrium and spinodal curves, respectively. In non-hydrate regions which comes before the line AA' (point N), the system is superheated and no hydrate will form. In region, at point C, the

system enters into the metastable region at crossing the equilibrium curve. In the metastable region, C–D, spontaneous crystallization is improbable unless seed crystal is added. Across the spinodal line with further increased supersaturation levels along the path D–H, spontaneous crystallization may occur and the probability of nucleation increases with decreasing temperature (point H). The thermodynamic spinodal line refers to the limit of metastability [9, 62, 63].

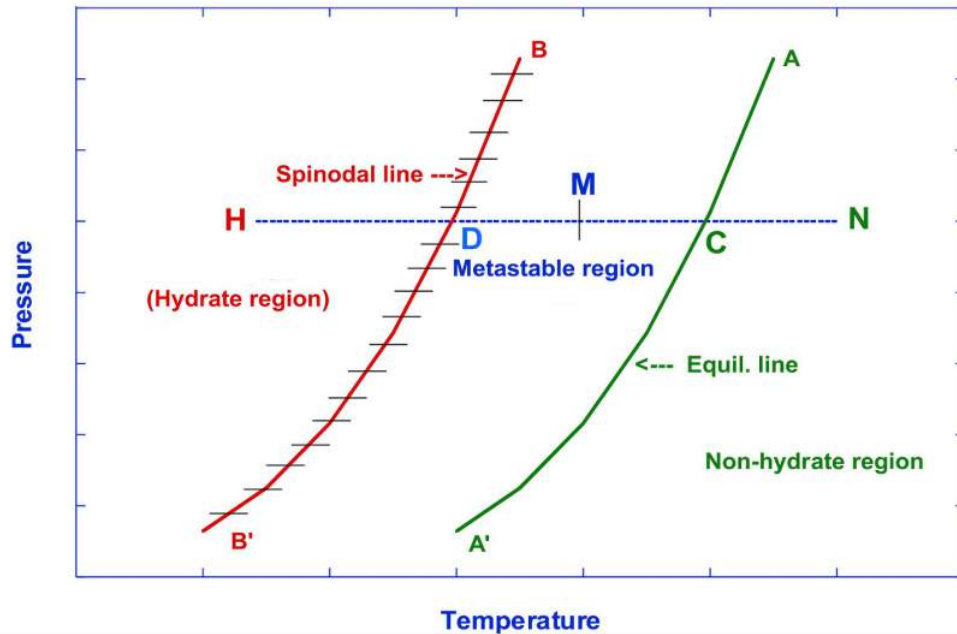


Figure 2.8: Non-hydrate, metastable, and hydrate regions. Adapted from Ke et.al., [9].

Thermodynamically, the system is in metastability region during the induction time. Once hydrates begin to form, they grow very rapidly as seen in Fig.2.9 [10]. In Fig.2.9, it is still possible to notice that the gas consumption during the induction time is minimal, considered not significant when compared to the moment when the hydrate particles agglomerate, gas consumption is very strong.

2.4 Hydrate inhibitors

Formation of gas hydrates can be eliminated or slowed by several methods. Thermodynamic prevention methods control or eliminate elements necessary for hydrate formation: the presence of hydrate forming guest molecules, the presence of water, high pressure or low temperature [64]. Eliminating any one of these four factors from a system precludes the formation of hydrates. Unfortunately, the elimination of these hydrate elements is often

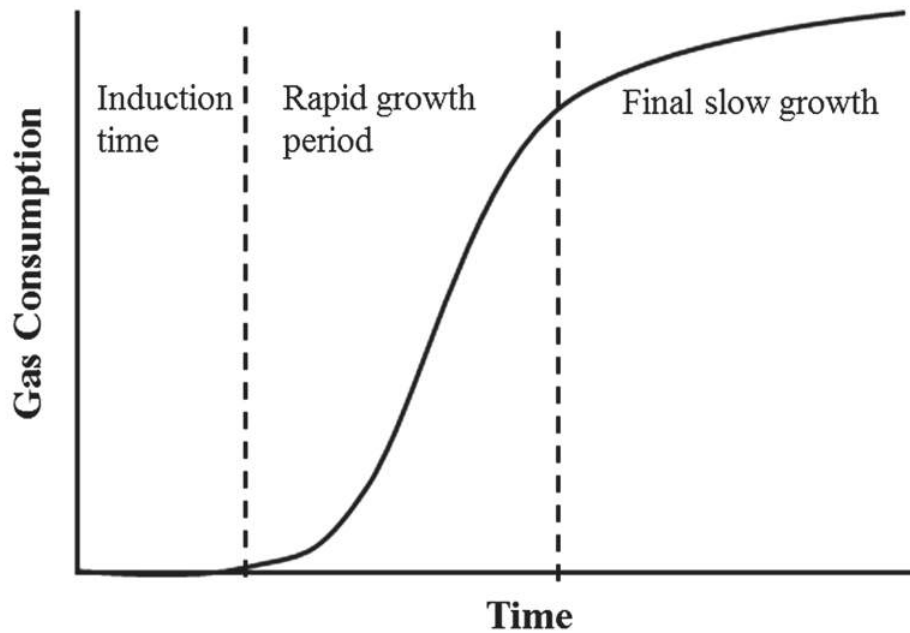


Figure 2.9: Hydrate formation phases as a function of gas consumption and time. Taken from Warriar et.al., [10].

impractical or even impossible. For long subsea transmission lines, heating and insulating is a common mechanical solution to hydrate problems [65].

Heating, using insulated pipelines, can in some cases allow that the system conditions transfer from hydrate stable zone to hydrate-free zone. But for the long distance pipes, heating and insulating pipelines become costly [66]. Water removal is an essential method to prevent the hydrate formation. It has been used in many long distance transportation lines. But it is difficult or expensive to remove water totally from the gas and oil, especially in the production well pipes. A practical method to prevent the hydrate formation is to inject chemical agents into the pipes to prevent hydrate formation, which are called hydrate inhibitors. Hydrate inhibitors include thermodynamic hydrate inhibitors (THIs), kinetic hydrate inhibitors (KHIs) and anti-agglomerant inhibitors. The last two are named low-dosage hydrate inhibitors (LDHIs) [11].

2.4.1

Thermodynamic hydrate inhibitors (THIs)

According to Wang et. al., [11] Thermal hydrate inhibitors are a kind of materials that can alter the thermodynamic conditions of hydrate by shifting the hydrate formation region to lower temperature and higher pressure. Typical THIs include methanol (MeOH), monoethylene glycols (MEG), and electrolytes. These compounds can form hydrogen bonds with water molecules to avoid the formation of ordered cages. Just because THIs act with water

molecules, the usage of THI is very high, which concentration used is 10 to 50 wt% based on water.

Alcohol is usually more employed in gas field, because it is less corrosive. On the other hand, the advantage of MeOH includes its low cost and high efficiency, especially at low concentrations. But has the disadvantage of a high degree of toxicity and loss of the material - due to its evaporation, during its application. Comparing with MeOH, MEG has larger chemical stability, is less poisonous and causes less environmental problems, and it's low solubility in the final gas products, makes it more applied in the gas fields [67,68]. MeOH is applied an intermittently application in most cases, such as in restarting well, or removing hydrate blockage [69–71].

Electrolytes are the other kinds of THIs, shifting the hydrate dissociation conditions to lower temperature and higher pressure. The ions dissolved in aqueous solution will interact with the dipoles of water molecules through electrostatic forces which are much stronger than the hydrogen bonds hindering the formation of hydrate particles [72]. Though the use of salts as THIs directly into the systems is avoided because they will rot the pipeline, salts always exist in produced water and are also widely prevalent in the gas production [11,73].

2.4.2 Kinetic hydrate inhibitors (KHIs)

The most outstanding advantage of KHIS over THIs is the low amount required in its used to be effective. Lederhos et. al., [74] observed an extension in the period taken to form hydrates by inserting a crystal stabilizer (KHIs) among hydrate crystals. Tests proved that this kind of inhibitors was effective in prolonging the hydrate nucleation and growth time.

Kinetic hydrate inhibitors do not alter the gas hydrate phase equilibrium condition but prolong the hydrate nucleation and growth. So, KHIs are called low - dosage hydrate inhibitors. KHIs are mainly water soluble polymers, such as poly (vinyl pyrrolidone - PVP), poly(vinyl caprolactam - PVCap), (polyvinylpiperidone - PVPip) and (N-vinyl pyrrolidone copolymer - VP/VCap), see Fig.2.10.

These inhibitors have certain groups adsorbing on the hydrate surface and bonded with the water molecules that form the hydrate structure. There are two classes of KHIs: synthesized and natural [11,65]. Synthetic inhibitors are those produced in laboratories using chemical substances already existing and studied (PVP and PVCap, for example) while natural inhibitors are found in nature. These natural inhibitors are called green inhibitors. Antifreeze proteins (AFPs) is an example of natural inhibitor and exist in some deep ocean fish

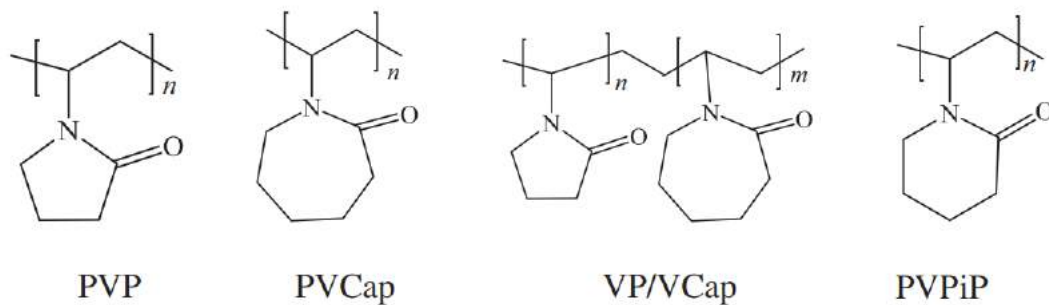


Figure 2.10: KHIs example structures. Taken from Wang and Lang, [11].

or some frigid zone animals. These substances have the ability of protecting organisms against freezing at low temperature. AFPs have been tested to inhibit the formation of ice crystals, which can bind to the surface of ice nuclei [75].

2.4.3 Anti-Agglomerants (AAs)

Just like the KHIs, the AAs are classified in the low - dosage hydrate inhibitors group. Anti-Agglomerants operate via different mechanism regarding the KHIs. AAs allow hydrate crystals to form but the hydrate crystals are kept small and non-adherent [76]. The small hydrate crystals are formed and are kept well dispersed in the available liquid hydrocarbon. This allows the hydrates be transported in the production flow lines as a material with low viscosity. The hydrate inhibition mechanism of the AAs is related to how the AAs molecule works. The AA operates via two chemical groups within its structure that have two important functions. Firstly, part of the AAs is incorporated into the hydrate crystal structure [77]. This is typically an organic quaternary ammonium or phosphonium salt. Secondly, the AAs has a long hydrocarbon 'tail' that makes the combined 'hydrate crystal - AA's structure soluble in hydrocarbon fluids preventing the formation of larger hydrate crystals [78].

AAs have the advantage that they are not restricted by the subcooling of the system [77]. AAs have also been seen to perform well regardless of the system's residence time in the hydrate region, including extended shut-ins larger than 2 weeks. With this in mind, the application of AAs becomes the most cost effective treatment at higher subcoolings. This is especially relevant as unlike other flow impediments, such as paraffins, asphaltenes and scale, nearly every deepwater system is at risk of hydrate formation [79].

2.5

Experimental methods of rheology

The experimental techniques used to determine the rheological properties of materials, both qualitative and quantitative, are governed by rheometric techniques. The flow properties of fluids are possible to determine through the use of devices called rheometers, while measuring systems used for viscosity measurements are specified as viscometer. The rheometers can be categorized by the flow type in which materials properties are investigated: simple shear and extensional flow. The shear rheometers can be divided into rotational and capillary. In the rotational, the shear is generated between fixed and moving solid surfaces and in the capillary the shear is generated by a pressure difference over the channel through which the material flows [12]. Capillary rheometry allows assessing the material properties at high shear rates flow properties relevant for industrial applications [108]. Some of its advantages are the easiness to placed the sample wich is crucial when dealing with high viscous melt at high processing temperature. Second, the shear rate and flow geometry are similar to the conditions found in processes such as extrusion and injection moulding [109]. A capillary rheometer has a pressure driven flow for which the velocity gradient or strain rate, and also the shear rate, will be maximum at the wall and zero at the center of the capillary, making the flow non-homogeneous [110].

The extensional rheometers are relatively less developed than shear rheometers because of the difficulties to generate homogeneous extensional flow especially for liquids with low viscosity [12, 111]. Many different experimental techniques have been developed to characterize the eleongational properties of fluids and predict their processing and application behaviour.

2.5.1

Rotational rheometer

The rotational rheometer works with two different regimes of deformation: imposition of a constant rotational speed or a constant torque, corresponding to controlled shear rate and controlled shear stress, respectively [12]. Rotational rheometry is higly used because it is capable of evaluate properties under a considerable range of shear rates generated through the variation of the rotation speed of the impeller or sample container [112]. The concentric cylinder, cone-and-plate, and parallel-plate are the most common rheometric systems used in laboratory tests, see Fig.2.11.

The measuring system of concentric cylinders is composed of an external cylinder (cup) and an internal cylinder (bob), as shown in Fig.2.11a. It is worth

mentioning that the bob can have the shape of a cylinder, as well as the shape of other types of geometries such as a vane or a helical shape. The system can basically operate in two ways, the outer cylinder can move and the bob remains stationary or vice versa.

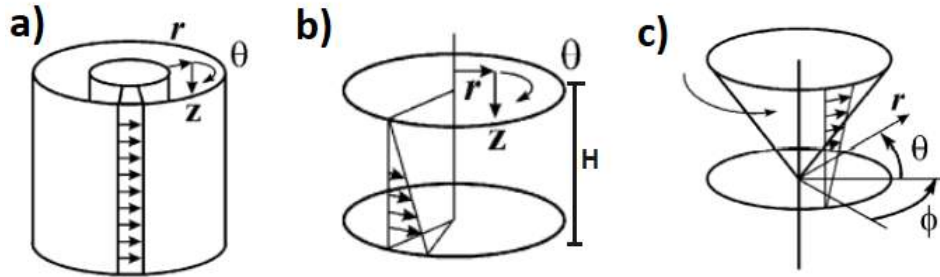


Figure 2.11: Rotational rheometric measurement systems: a) concentric cylinder, b) parallel-plate, and c) cone-and-plate. Taken from Boger [15].

In the parallel plate geometry the sample is confined between the two coaxial parallel plates (gap H) and is sheared by the rotation of one of the plates, see Fig.2.11b, and for a cone-and-plate geometry the sample is contained between a rotating relative flat cone and a stationary plate, see Fig.2.11c [12].

2.6 Studies of gas hydrates

The gas hydrate phenomenon have been continuously studied by several researchers in order to get a better understanding of its formation, dissociation or flowability through the oil . Most of these studies are conducted in high pressure systems, since similar thermodynamic conditions can be applied which that found in the practical applications.

The rheological behavior of hydrates slurries formed by a mixture of water and Tetrahydrofuran (THF) under high pressure and low temperature conditions were studied by Silva et. al., [113]. THF hydrate slurries tests were performed for concentrations of 30, 40, and 50% of THF by mass. The shear rate was set equal to 300 s^{-1} , chosen to avoid wall slip effects. For the concentration of 30% of THF, the tests were carried out with a pressure variation of 5, 10, 20, 30, 50 and 60 bar. For 40% of THF it was 10, 30, 50, 70, 90 and 100 bar and for 50% it was with the initial pressure of 1.2 bar, then 10 bar and then the same pressure variations of 40% up to the final pressure of 100 bar. It should be noted that the geometry used has a smooth wall, so wall slip could be an issue. The gas used to pressurize the system was nitrogen. The tests performed showed that the torque limits in the rheometers dramatically reduced the range of reliable data. Moreover, wall slip was an

issue difficult to be considered inside the pressure cell. The rheological data showed the increase of the viscosity with the pressure. So, higher pressures tend to increase and accelerate hydrates formation because the agglomeration of the crystals becomes more intense. They observed a large variation in the slope of the viscosity curve which indicated the formation of hydrate crystals, that was accompanied by a reduction in pressure. This decrease in pressure was due to the nitrogen gas consumption during the process of the hydrate formation [113]. Oscillatory tests performed showed that the slurries have a yield stress, below which they present a viscoelastic behavior.

Charin et. al., [114] studied the formation of hydrates in non-emulsifying systems in a high-pressure cell coupled to a rheometer. Mineral oil and kerosene were used. From the results obtained was possible to calculate the gas consumed to form hydrate and the hydrate fraction that was formed. A vane geometry was used with a modification to prevent the accumulation of hydrate particles between the blades. The experiments were carried out at constant pressure with mineral oil and kerosene as oily phases. Different mixing rates (200, 300 and 450 rpm) and water content (5, 10, 20, and 30 vol%) were used. Six stages were employed by the authors during the experimental protocol: saturation, cooling, hydrate formation, steady state, closing and restarting. It was seen that for a given water content with mineral oil, mixing at 450 rpm showed the lower viscosity values compared with 200 and 300 rpm, suggesting that the suspension maintained by higher shear has lower viscosity because the higher mechanical energy input makes the hydrate particles smaller and better dispersed. The results using kerosene showed that the systems have a noticeably high relative viscosity when compared to systems with mineral oil, suggesting that hydrate formation caused a substantial increase in viscosity in the systems with kerosene. This result evidence that the system containing kerosene is more detrimental, with respect to flow assurance concerns, than systems with mineral oil. In this work, the gas consumption was determined by the volume of gas measured in a syringe pump for the different experiments performed. It was observed that the amount of hydrate fraction formed increased with the increment in the water cut and with increasing shear rate.

A modified couette geometry was also introduced by Pandey et. al., [16], as shown in Fig.2.12, for the study of gas hydrates in multiphase systems. According to the authors, modified couette geometry helps to achieve enough mixing of multiphase systems when measuring viscosity or other rheological properties. The conventional cup and bob have poor mixing capabilities, especially at low shear rates, therefore unstable, pre-mixed emulsions and slurries tend to separate out. The results obtained on the viscosity of hydrates

systems showed a clear increase in viscosity from 0.001 to 25 Pa.s when the systems were analyzed at the same shear. This characteristic increase was not evident for the experiments performed with conventional couette geometry.

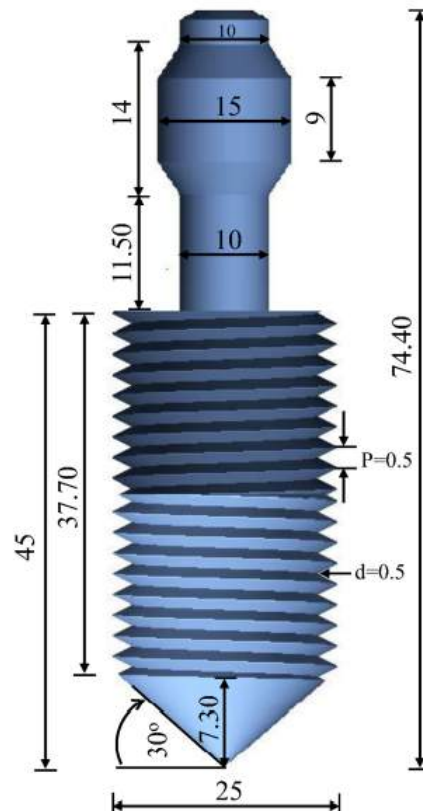


Figure 2.12: Modified bob (P = pitch, d = depth, all dimensions are in mm). Taken from Pandey et. al., [16].

Recently, Webb et. al., [17, 115] studied the high pressure rheology of methane hydrates formed from water-in-model oil emulsions. In that work, the viscosity profile was measured during the formation, growth, and dissociation of hydrates. In the tests performed by the authors the water fraction, temperature, initial pressure, and shear rate were varied. They used a high pressure pre-mixer to mix the oil with water and methane gas. Subsequently, the emulsion was transferred to the concentric cylinder geometry to measure the viscosity of the hydrate systems. It is to say, two different cells were used, one to saturate the emulsion and the other for rheological measurements. The results reached by the authors showed an increased in the hydrate slurry viscosity when the driving force was reduced. In general, both works achieve the same results where the increase of the water cut in the emulsion provokes an increase in the hydrate viscosity. And complementing his study, Webb et. al., [17] analyzed the fraction of hydrate formed. The higher the water cut, the smaller the amount of hydrate fraction formed. The Fig.2.13 showed that 0.10

and 0.20 wt% convert all water to hydrate. But this statement is contested in the literature by several authors. Bassani et. al., [116] reported that water is never entirely converted into hydrates, due a phenomenon of kinetic limitation, usually interpreted as a limitation due to the mass or heat transfer processes. Melchuna et. al., [117], Turner et. al., [47], Joshi et. al., [118], and Shi et. al., [48] are some of the authors who also studied the amount of water converted into hydrates in a high pressure system and did not identify 100% conversion of the water into hydrates.

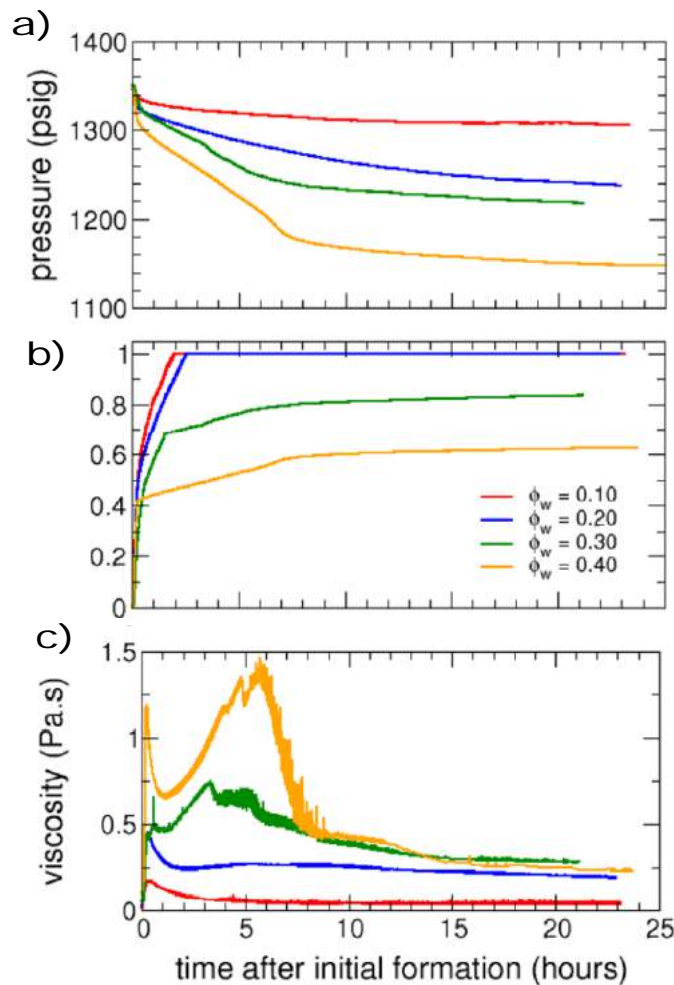


Figure 2.13: a) Pressure, b) fraction of water converted to hydrate and, c) viscosity over time as hydrates form in water-in-mineral oil emulsions at 0 °C, 1500 of psig initial pressure, and 100 s⁻¹. Taken from Webb et. al., [17].

Recently Nair et. al., [18] investigated the flow properties of methane hydrate in the presence of natural sediments containing minerals and complex salts from the Krishna-Godavari Basin of offshore India. A high pressure rheometer with a modified couette geometry was used as shown in Fig.2.14. The conventional couette geometry has several shortcomings such as poor

mixing capabilities particularly at low shear rates as noted by Pandey et. al., [16]. Rheological investigations were carried out using three concentrations of different sediments of 10, 35 and 50 wt% at 10 MPa each at four different temperatures of 273.15, 277.15, 281.15, and 285.15 K. The viscosity was analyzed for each concentration with a variation of the shear rate during hydrate formation. It was found that the volumetric fraction of hydrate varied directly with the sediment concentration and inversely with the temperature. During the shear scan measurements, it was found that the viscosity gradually decreased with increasing shear rate. That confirms the shear dilution behavior of the slurry of hydrate. However, at lower temperatures (273.15 and 277.15 K), it was observed that the viscosity profile did not show this gradual behavior.

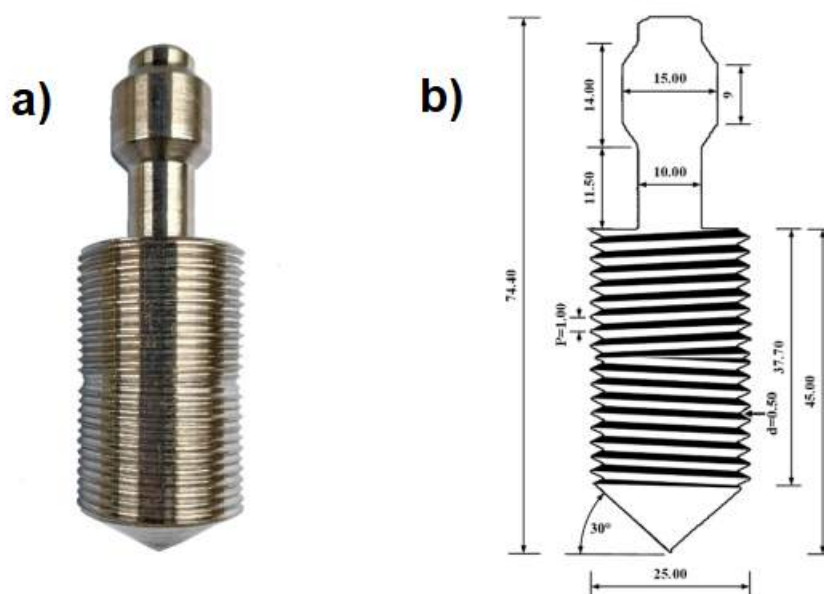


Figure 2.14: Schematic of the experimental setup: (a) Double-threaded modified bob geometry used for the rheological measurements of hydrate and (b) dimensions of the modified bob geometry. Taken from Nair et. al., [18].

The rheological properties of methane hydrate formed from water in crude oil emulsions were also studied by Qin et. al., [5]. The experiments were performed in a high-stress-controlled rheometer. A vane rotor was used to maintain sufficient methane saturation in the oil phase during the hydrate growth period. Dynamic measurements were made with the rheometer capable of analyzing changes in viscosity due to the formation of hydrate and due to the reduction of methane content in the continuous oil phase. Systems with water cut from 5 to 30% per vol. were used. It was noticed a viscosity increase of the hydrate slurry between 20 and 60 times during the growth of the hydrate. The results showed that the hydrate paste at steady state conditions demonstrated shear thinning behavior at 1 and 5°C. After the annealing period of eight

hours to simulate a subsea stoppage, the viscosity did not decrease as well as the pressure. The vane blade rotor was able to maintain saturation of the crude oil phase and the ability to maintain dissolved gas content suggests the presence of secondary axial flows, which may function to increase the apparent viscosity.

One of the goals of this work is to analyze the hydrate formation under different rheometric geometries. The vane geometry (used in this work), has been previously studied and in addition to the experimental tests it was also studied in numerical form. Nazari et. al., [19] calculate the isothermal flow parameters in a vane geometry through the finite element method (Fig.2.15). The mass and momentum continuity equations were used to obtain the velocity, pressure, and then stress fields. The numerical model was validated by comparing the results with experimental data reached in a torque at different angular velocities [19]. An important issue raised in that study was the main points of highest speeds between the geometry and the cup where it is inserted. It was evidenced that the highest speeds occur near the geometry palettes. In the areas adjacent to the cylinder walls (cup) there were almost stationary residual regions. As can be seen in the Fig.2.16, the red color represents the highest speeds, while the blue colors represent the lowest speeds. The same behavior regarding the velocity fluid fields were observed for two fluids with different viscosities. Rabia et. al., [20] also showed similar results for the vane geometry regarding the points of higher and lower velocities when the fluid was subjected to a shear rate, as can be seen in the Fig.2.17.

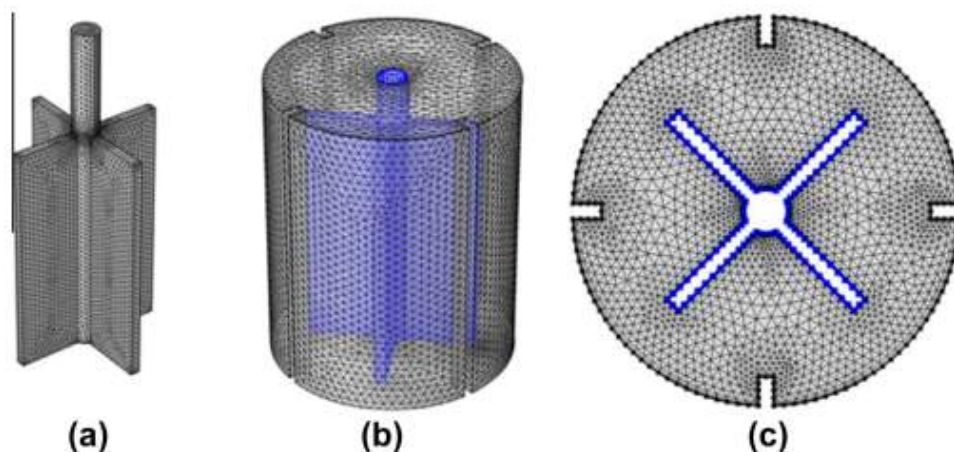


Figure 2.15: Simulation of a vane geometry using the (a) 3D view of the impeller, (b) 3D view of the geometry, and (c) 2D view. Method taken from Nazari et. al., [19].

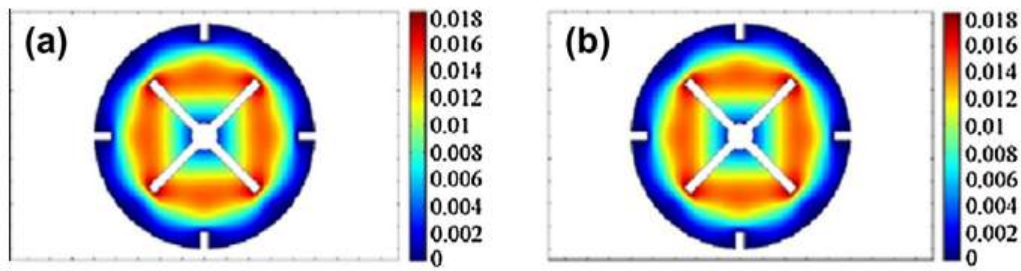


Figure 2.16: Tangential velocity magnitudes (m/s) at 10 rpm for the fluid with viscosity: (a) 98 mPa s, (b) 12,000 mPa s. Taken from Nazari et. al., [19].

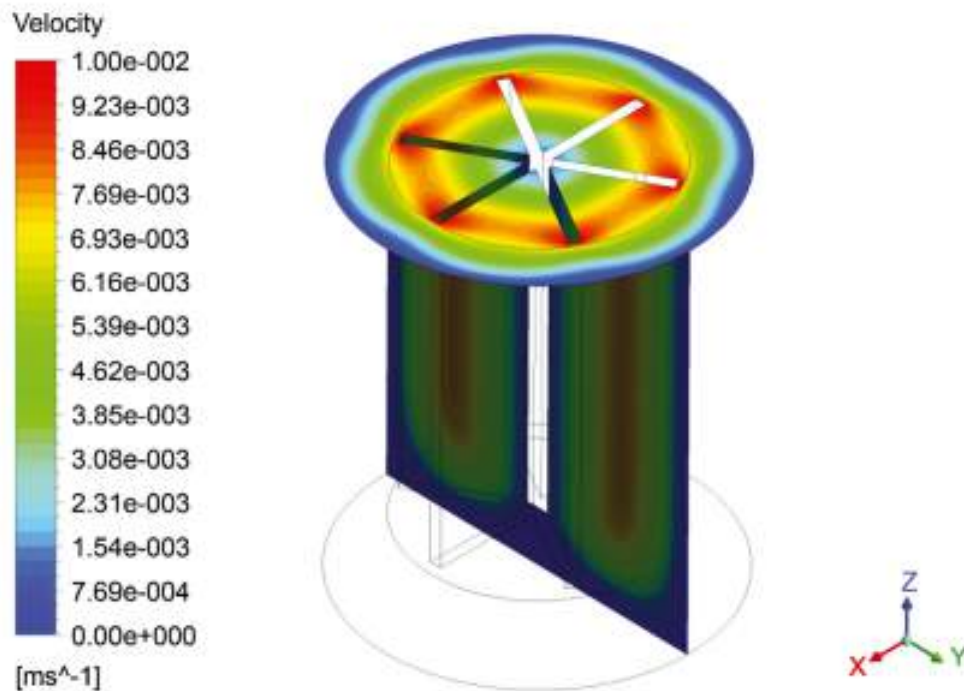


Figure 2.17: Top and side cutting planes showing isovalues of the velocity magnitude for a gap of 5 mm. Taken from Rabia et. al., [20].

A shear rate is an important variable that influence on hydrate formation. Most of the studies indicate that the time taken for hydrates formation is reduced with the increment of the shear. Turner et. al., [47], Lim et. al., [119], Zheng et. al., [120], and Douieb et. al., [121] are some of authors who achieved this result. One of the explanation was that this could primarily be attributed to a decrease in the time required for stable gas hydrate nuclei to be generated and to grow to a macroscopically detectable size [121]. This same variable has been studied for Muhlstedt et. al., [122]. The authors assessed the hydrate formation with a shear rate and at stationary conditions - without agitation. The results showed that the elastic modulus and the yield stress of the statically (without shear) formed hydrate slurry were more than 1 order of magnitude larger than those dynamically formed (imposing shear). These

findings are important because can bring new perspectives for improving the techniques and procedures for the flow startup of hydrate slurries in drilling fluid operations [122].

In recent years, ionic liquids (ILs) are considered as potential thermodynamic and kinetic inhibitors of gas hydrate formation. According to Rogers and Volt [123], ionic liquids are being defined as salts composed solely of ions with melting points below 100 °C. Ionic liquids as being non-volatile, non-flammable, intrinsically ‘green’, highly electrochemical stable, highly thermally stable, and comprising simple ionic species [124]. Maiti et. al., [21], study the effect of two ILs, (C8mimBF4) and (C12mimBF4), on the formation and dissociation of hydrates thermodynamically and kinetically. The study reveals that the performance of IL solutions in hydrate inhibition was effective and has the ability to prevent the formation of hydrates both thermodynamically and kinetically. The results show that ILs significantly increase the induction time. These ILs not only change the equilibrium mixture hydrate dissociation curve but also slow down the nucleation and/or growth rate of mixture hydrate. The IL solution decreases the hydrate formation rate in comparison with pure water Fig.2.18.

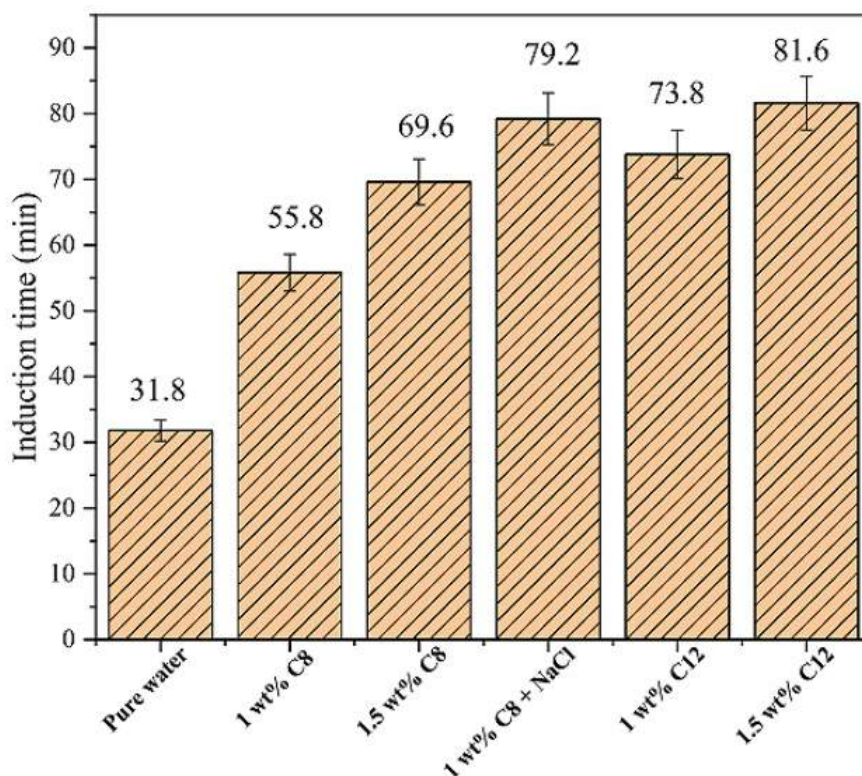


Figure 2.18: Effect of ILs on gas hydrate induction time in comparison with pure water. Standard deviations are shown for each condition. Taken from Maiti et. al., [21].

2.7

Objectives

The main objective of this work is to study the formation of ethane gas hydrate from the rheological point of view using two different measuring geometries with a controlled rate rheometer.

Other complementary objectives for the study are listed below:

- Investigate the influence of parameters such as subcooling, shear rate, and water volume fraction on ethane gas hydrate formation at high pressures using two types of rheological geometries;
- Evaluate the amount of water that was converted into hydrates for the tests where the formation of hydrates was evinced;
- Analyze the rheological approach between the relative viscosity curves and the amount of water converted to hydrate. The tests selected for this relationship had the same initial pressure;
- Study the behavior of hydrate slurries through shear rate ramps performed immediately after the steady-state of hydrate formation was reached;
- Analyze qualitatively the relation between the shear rate ramp results;
- Verify the effectiveness of the rheological geometries employed to form hydrates.

3 Experimental Methods

In this section the materials and experimental methods employed in this work are explained. Ethane was selected as a hydrate former molecule since this gas allows hydrate formations at relatively low pressures with similar subcooling found in practical applications (e.g., at 20 bar the subcooling was around 9 °C). The experiments were conducted in a high-pressure cell with a shear rate controlled rheometer. Two different rheometric geometries were used: concentric cylinder and vane rotor.

3.1 Materials

A standard oil, a surfactant, deionized water, and basic laboratory equipments were used to prepare the emulsion.

Deionized water was obtained from a ultra-purified water system composed of a reverse osmosis membrane and a deionizing resin (GEHAKA). The oil employed was known as Primol oil 352 (ExxonMobil Specialties), characterized as a highly refined oil, composed of saturated aliphatic hydrocarbons, with a density of 860 kg/m³ at 20 °C. The oil-aqueous phases were stabilized by adding the nonionic oil-soluble surfactant sorbitan monooleate (Span 80, Sigma Aldrich) at a concentration of 0.08% (m/m) of the total mass of the emulsion. Such a concentration was selected in order to satisfy both criteria, reasonable time to hydrate formation (20 h inside the hydrate forming conditions) and emulsion stabilization time of at least 2 h. This ensures enough time to place the emulsion inside the cell and conduct the experiment where the emulsion was subjected to a controlled shear rate.

The results at high-pressure conditions suggested that Span 80 acts as a hydrate inhibitor, analogous to what was observed by Karanjkar et. al., [125] who performed experiments at atmospheric pressures in cyclopentane systems. The effects of Span 80 are presented in the results section.

3.2

Emulsification and microscopy

An emulsion is a mixture of two immiscible liquids in which droplets of one of the liquids become stably suspended in the other [126]. Emulsions are more stable when settling, flocculation, or coalescence is inhibited. With water-in-model oil emulsions, the electrostatic forces are usually weak because the continuous oil phase has a low dielectric constant and a correspondingly low ion concentration [127, 128]. Hence, the water droplets usually do not remain dispersed but are free to flocculate and/or settle. As two droplets approach each other, their surfaces dimple to form a planar region at the point of closest contact. Fluid drains from this region as the droplets continue to approach. As well, the surface active material on the interface is spread more thinly when the surface deforms creating openings for water to bridge the gap between the droplets. When the gap is bridged, the droplets rapidly merge. A highly elastic film will resist deformation. As well, there will be a greater driving force for surfactant to diffuse to the depleted region between the droplets. Both factors will inhibit coalescence [127, 129].

Emulsions can be categorized into the following three classes: water-in-oil, oil-in-water, and multiple or complex emulsions. Water-in-oil emulsions comprise water droplets in an oil-continuous phase, and oil-in-water emulsions are attributed to droplets of oil in a continuous aqueous phase. Multiple emulsions are more complicated and are made of tiny droplets in larger droplets, which are suspended in a continuous phase [130].

Adequate mixing and the presence of a surface-active agent are two important factors that lead to the emulsion formation when the oil and water phases are brought together. During the production of crude oils, there are a variety of mixing sources that create shear forces. Generally, the larger the amount of shear, the smaller the droplet size of the dispersed phase which result in more stable emulsions [131]. The second most important factor in the emulsion formation is the presence of an emulsifying agent. They are classified into the following two types: finely divided solids and surface-active agents [132].

Fine solids generally stabilize a emulsions mechanically, thereby, assisted by providing mechanical energy of some form, such as slight shaking, mixing or sonication [133]. These materials, which are wetted by both water and oil, should be smaller than the emulsion droplets and should accumulate at the water/oil interface. The effectiveness of these particles in stabilizing emulsions is strongly dependent on various factors, such as inter-particle interactions, particle size, and wettability of the material [134]. Fine solid materials existing

in the produced oil include clay particles, sand, asphaltene/wax, silt, and mineral scales deposited on the water/oil interface [135,136].

Surface-active agents or surfactants are the particles that are soluble in one or both oil and water phases. They have a hydrophilic branch, which has tendency to interact with water, and there is a hydrophobic branch that does not have the characteristic of interacting with water, no affinity, see Fig.3.1. Due to their special chemical structure, surfactants tend to create an interfacial film at the oil-water interface [137]. This phenomenon generally leads to a reduction in the interfacial tension and, consequently, enhances the droplet dispersion and emulsification. The chemical structures of two important surfactant molecules are shown in Fig.3.2 [132].

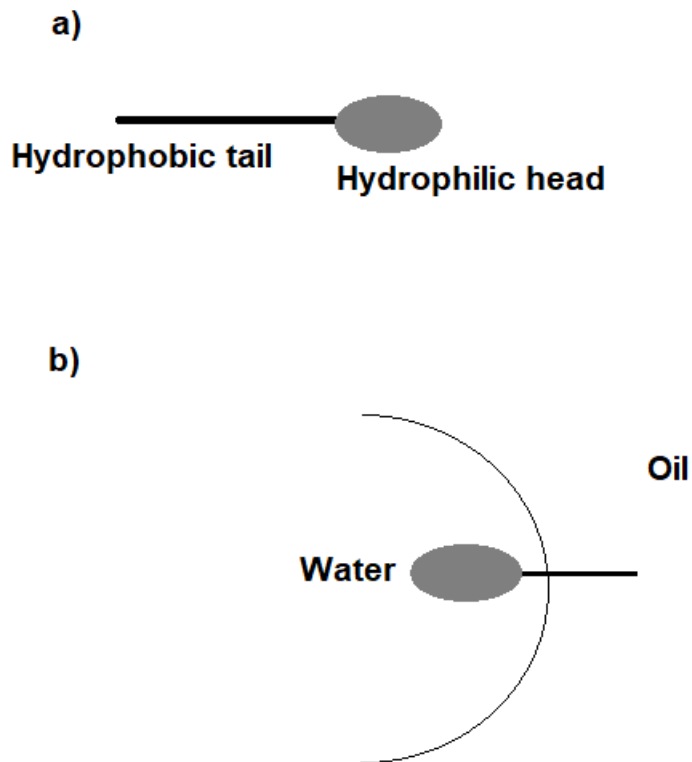


Figure 3.1: Surfactant: a) structure and b) parts interaction with the oil and water, which in this case is a water-in-model oil emulsion. Adapted from Kale e Deore, [22] and Myers et. al., [23].

From a thermodynamic perspective, an emulsion is an unstable system due to its natural tendency for a liquid/liquid mixture to minimize its interfacial interactions (and/or interfacial energies) [126]. However, most emulsions demonstrate kinetic stability after a period of time. Oil-field emulsions are usually categorized based on their degree of kinetic stability. The interactions between the surface-active agents and water/oil interfaces are

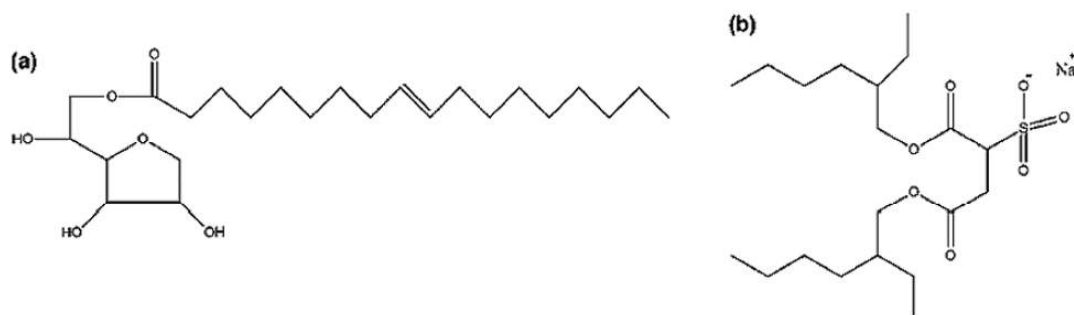


Figure 3.2: Molecular structure for surfactants: (a) sorbitan monooleate (Span 80); (b) sodium di-2-ethylhexylsulfosuccinate (AOT). Taken from Kale e Deore, [24].

primarily responsible for emulsion stability. During emulsification, emulsifying agents are adsorbed to the freshly formed interfacial film, which weakens the interfacial forces and allows the immiscible phases to be partially mixed [132, 138, 139]. After the emulsion formation, it begins to be altered due to different time-dependent processes, which are coalescence, flocculation, sedimentation, and creaming [140]. The stabilizing mechanisms is that water/oil emulsions are assumed to be liquid/liquid colloidal dispersions. Their kinetic stability is a result of droplets with a small size and the formation of an interfacial layer between the water and the oil droplet [132].

The droplets size can be obtained by optical microscopy. A fresh sample of an emulsion is transferred into a rectangular glass tube and through the microscope it is possible to analyze the droplets sizes present in the emulsion sample. From that, photomicrographs and drop size distribution histograms present a frequency distribution from the sample [141]. The size of droplets dispersed in the emulsions is a vital characteristic as it can modify the rheological behaviours and stability of emulsions. This property can be used to calculate the surface area required for gas hydrate formation, since the area/interface controls the mass and heat transfer rate [142]. In general, the heterogeneous dispersion of liquid/liquid systems can be classified into the following two categories: a) emulsions with a droplet size of microns, which are thermodynamically unstable, and b) micro-emulsions with a droplet size in the nanometer scale, which are considered thermodynamically stable emulsions [143].

The characteristics of an emulsion change constantly, from the beginning of its formation until its complete separation, and still vary with temperature, pressure, formation time, degree of agitation, and others [144]. There are

several types of mechanical stirrers used for the preparation process of emulsion, from simple stirring paddles, which can produce droplets of dispersed phase with about 10 μm , to rotor-stator type stirrers (see Fig.3.3), which are generally used in the production of emulsions [25].



Figure 3.3: Cross section of a rotor-stator type stirrer. Taken from Fujii et. al., [25].

Rotor-stator type agitators operate by pumping the phases of the emulsion. This pumping takes place through a narrow opening between a perforated cylinder (the stator) and the blades of a rotary stirrer (the rotor) that rotate at high velocities [25].

In this present study water-in-model oil emulsions were formed with deionized water, mineral oil, and Span 80 employed as a stabilizing agent (surfactant). The emulsions (see Fig. 3.4) were prepared using the following methodology:

1. Weigh the required mass of Span 80;
2. Weigh the required mass of Primol oil;
3. Add the Primol oil in the same beaker of the Span 80;
4. Magnetic homogenization of Span 80 with Primol oil at a temperature of 35 °C and 1000 rpm for 5 min;
5. Addition of deionized water in the mixture of Span 80 and Primol oil at room temperature;

6. Homogenization of the components obtained in step 5 in the Turrax mechanical stirrer (model of a mixer IKA T25, rotor 18G), at 10,000 rpm for 5 min.

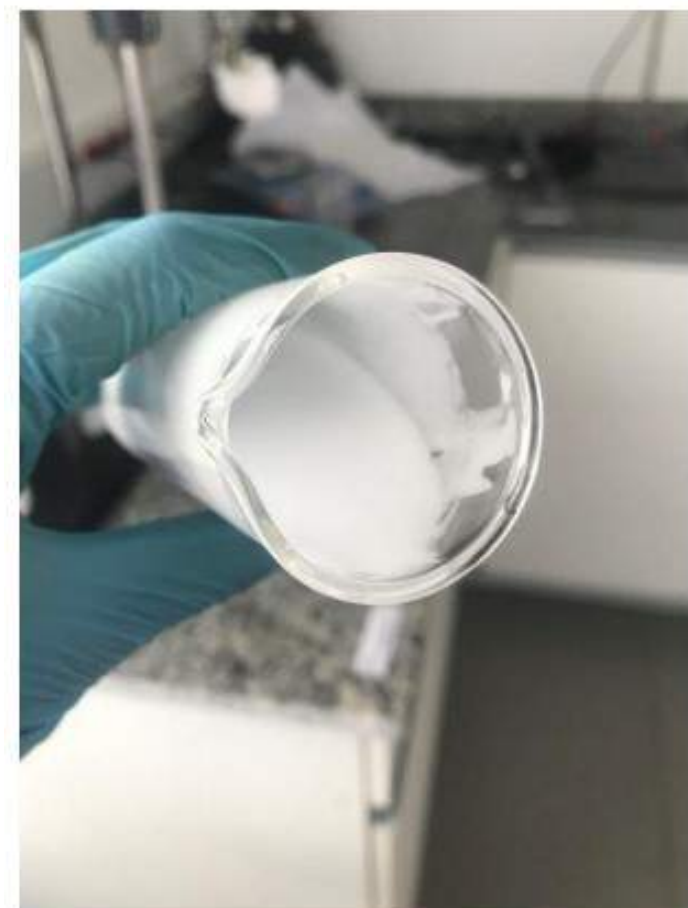


Figure 3.4: Appearance of the prepared water-in-model oil emulsion.

Depending on the geometry employed to perform the experiments, two different emulsions weights were used, 70 g for concentric cylinders, and 90 g for the vane geometry. This difference in quantity was due to the different configuration geometry. For the emulsion of 90 g, the homogenization velocity in the Turrax was different from that of 70 g, being the first 3 min at 10,000 rpm and the last 2 min at 12,000 rpm. This increase in agitation velocity in the final two minutes was necessary to produce a more effective mixing of the larger amount of emulsion. This agitation velocity was not set constant in the total 5 min because it was verified an increase in the temperature of the emulsion at the end of the mixing process. Therefore, it was decided to increase the speed only in the final minutes.

The stabilization of our emulsion was monitored through the droplet size distribution. The droplets were observed in a polarized light microscope

WVF (%)	MDD - 70 g of Emulsion (μm)	MDD - 90 g of Emulsion (μm)
25	38 (24)	70 (44)
30	38 (18)	57 (71)
35	19 (7)	19 (57)

Table 3.1: Mean droplet diameter of the emulsions with the standard deviation (in parenthesis).

(Nikon, Eclipse LV100 POL). The micrographs were captured at room temperature roughly two hours after the beginning of the experiment, and were processed through the software NIS-Elements. Fig.3.5 shows the micrographs and the mean droplet diameter distributions for the 30% water-in-model oil emulsions used with the vane and concentric cylinders geometries, corresponding to 90 g and 70 g, respectively. Fig.3.5 shows that although the proportion of the constituents of the emulsions was similar, the emulsion of 90 g (Fig. 3.5a) has larger and more non-circular shaped droplets, indicating an emulsion with less stability than the one used for the concentric cylinder system, showed in Fig. 3.5 b). The measurements of the mean droplet diameter (MDD) obtained for the different samples are presented in table 3.1. As noted, the MDDs have a tendency to decrease with the increment in the water cut for both systems considered.

3.3

Rheometry features and pressure cell

The rheological experiments were conducted in a rotational rheometer (Haake Mars III, Thermo Fisher Scientific), using two different geometries. Initially, a series of experiments with a smooth concentric cylinder geometry was performed, with bob height and radius of 80 mm and 17.5 mm, respectively. Subsequently, a homebuilt vane sensor was employed to conduct other battery of tests. The vane sensor consists of four blades connected to a shaft in a cross-format (see Fig. 3.6).

Each blade was designed with the aim of circumscribing the radius of the circle formed by the rotor of the concentric cylinders measuring system. Therefore, each blade has a length of 80 mm and circumscribes a circle with diameter equal to 35 mm [145]. The same cup, with a radius of 19.5 mm, was used for both the vane and concentric cylinder so that the horizontal gap was equal for both geometries. The validation of our homebuilt vane geometry was performed with standard fluids in the same range of torque used for the hydrate slurries measurements reached with concentric cylinders.

The pressure cell used comprises basically of a rotor (measuring

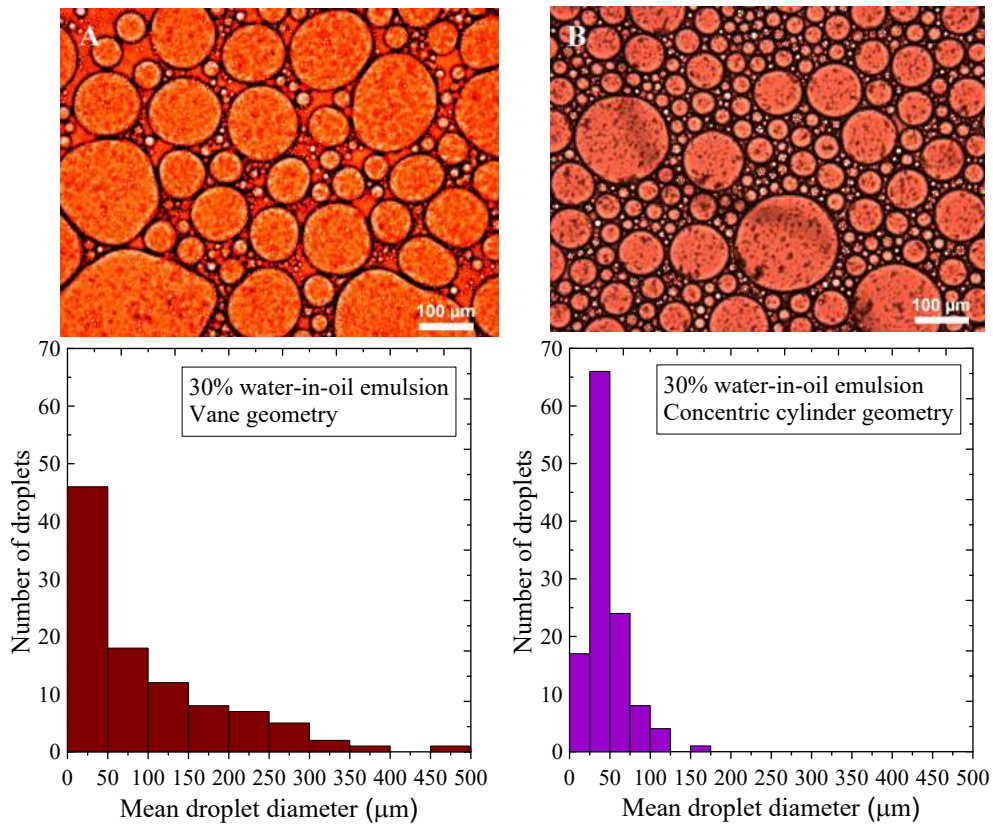


Figure 3.5: Micrographs and histograms of the 30% water-in-model oil emulsions used with the vane (A) and the concentric cylinder measuring system (B).

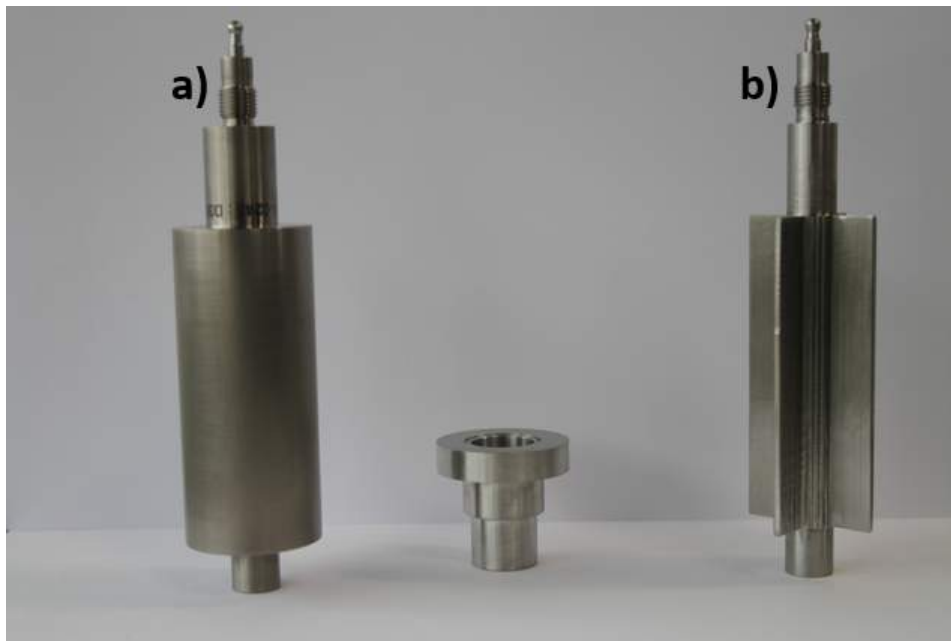


Figure 3.6: Geometries used in the experiments: a) concentric cylinders and b) vane.

geometry) and a stator (cup), and two magnets, as shown in Fig. 3.7. The cell allows measurements over a wide viscosity range under pressure up to 400 bar and temperature up to 300 °C. The rotor was supported by a lower and an upper sapphire bearing to achieve an optimal radial stability and accuracy. Once the magnet (inner one) was attached to the rotor, the sample was placed inside the cup. After that, the cup was sealed with a screwed lid. That is to say, there was not direct contact between the rotor and the rheometer shaft (as occur with conventional geometries).

Driving the rotor inside the cell was possible due the magnetic field created by the inner magnet and the outer magnet which was attached to the shaft of the rheometer measuring head (magnets are represented by the red color Fig. 3.7). The magnet that was inside the cell was the same used equally for the experiments performed with concentric cylinders and vane rotor. For a schematic drawing of the pressure cell and the magnetic coupling, see Fig. 3.7.

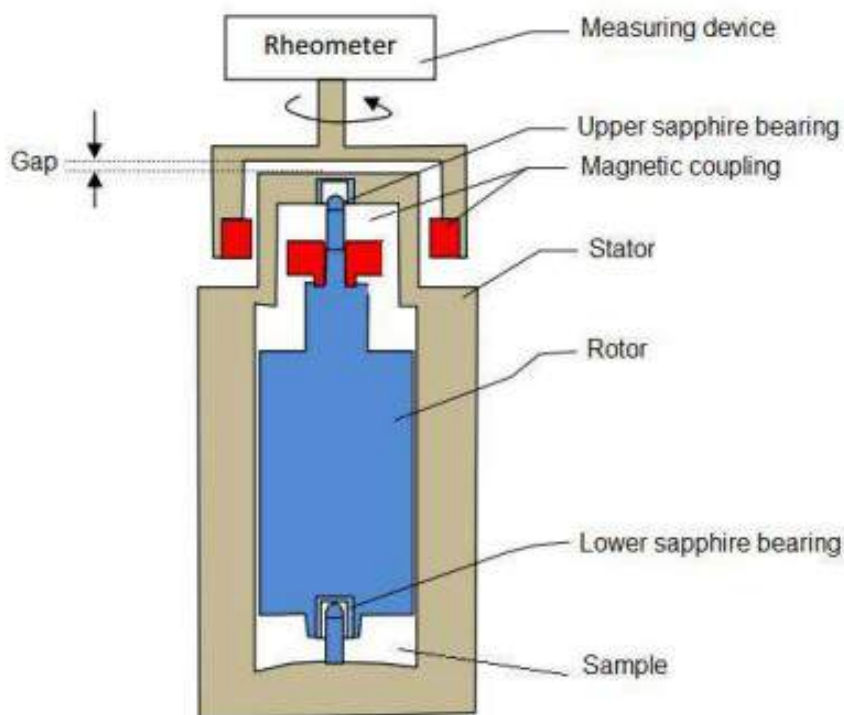


Figure 3.7: Diagram of the high pressure cell employed in this study. Figure taken from Sandoval et. al., [26].

3.4 High-pressure system

The high-pressure system included the gas reservoir located outside the laboratory (see the number (1) in Fig. 3.8). The gas was conveyed to a control

panel (2) inside the laboratory. From the control panel, the gas was driven to a double syringe pump 260D (TELEDYNE ISCO) (3), which allowed to set up and keep the pressure constant inside the pressure cell (4). The pressure cell (Thermo Fisher Scientific) was placed in the shear-stress-controlled rheometer Haake Mars III (5). The stator was the rheometric cup and comprises three connections in its upper part, for the pressure sensor, safety valve, and the gas inlet. The gas passage was controlled through a needle valve (6) placed before the gas inlet. Calibrations of the system were required since there was no direct contact between the rheometer-driven shaft and the sample. Furthermore, the additional torque created due to the friction between the rotor and the sapphire bearings needed to be discounted from the total torque. All calibrations were performed as indicated in the user manual provided by the manufacturing company, and several experiments with standard fluids were conducted to assess the validity of the measurements. The temperature control of the system was made with a cooling fluid circulating from a thermostatic bath (7) to a jacket coating the rheometer cup.

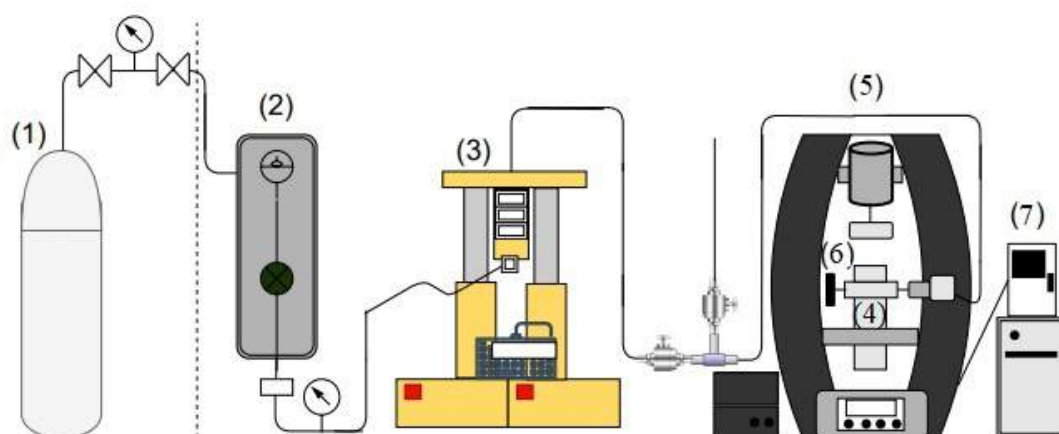


Figure 3.8: Representation of the high-pressure system used to conduct the experiments. Gas reservoir (1), control panel (2), syringe pump (3), pressure cell (4), rheometer (5), needle valve, (6) and thermostatic bath (7).

3.5 Experimental procedure

The experiments were conducted in three stages: gas dissolution, cooling until a temperature inside the hydrate stable zone, and induction time for hydrate formation (up to 20 h). Therefore, once the pressure cell was placed in the rheometer and coupled to its connections (pressure transducer and gas

inlet), the external magnet was coupled to the rheometer and the process was carried out where the zero gap was recognized by the rheometer. Then, the working gap of the test was programmed, which was 3 mm and 1 mm for the concentric cylinders and vane geometries, respectively. The experiment started by the rotation of the external magnet, previously connected to the rheometer. Subsequently, ethane gas at the set pressure was delivered to the cell. The gas dissolution step was conducted at 25 °C for a period of 4 h. During this period, the pressure inside the cell remained constant by means of the syringe pump. A complete gas dissolution was observed through the output gas flow rate in the syringe pump, which was null after a while within the 4 h period.

Once the dissolution process ended, the needle valve was closed and no more gas entered into the cell. At that moment, the two syringe pump was turned off and no longer was used during the rest of the test. The gas dissolution period of 4 h was followed by the cooling step, from 25 to 4 °C, at a cooling rate of 0.7 °C/min. The final temperature of 4 °C was kept constant until the end of the experiment. All experiments presented in this work were inside the hydrate envelope at 4 °C, and no hydrate formation was observed during the cooling process. Fig. 3.9 shows the typical results obtained during the dissolution and cooling process for the viscosity (represented by full symbols), and the pressure (represented by empty symbols).

The viscosity decreases because the dissolution of the gas in the emulsion. As a result, the emulsion was more foamy and less viscous. During the cooling, the viscosity increased and the pressure decreased. Wright [146], studied the microscopic relationship between viscosity, temperature and pressure. Molecules in a gas act appreciably on each other only if they are in close proximity. So, in atmospheric air, each molecule was for most of the time relatively far away from the rest, but when the gas was sufficiently compressed, the molecules were closed enough together for to be interacting with others. However, at a lower temperature the molecules will on the average have low velocities and so be not able in an encounter to approach more closely against the repulsive forces between them [147, 148]. So, having more space between molecules, more gas was dissolved (pressure decreases) and greater viscosity.

The final stage of our experimental protocol consisted of monitoring the hydrate formation occurrence, which was noticed by two concomitant physical variations, namely an abrupt increase of the shear viscosity and a reduction of the system pressure. In this work, the time elapsed between the instant when the system crosses the hydrate equilibrium curve until the onset of the severe viscosity increment was defined as the induction period. The tests were concluded if hydrate formation does not occur in an induction period of 20 h.

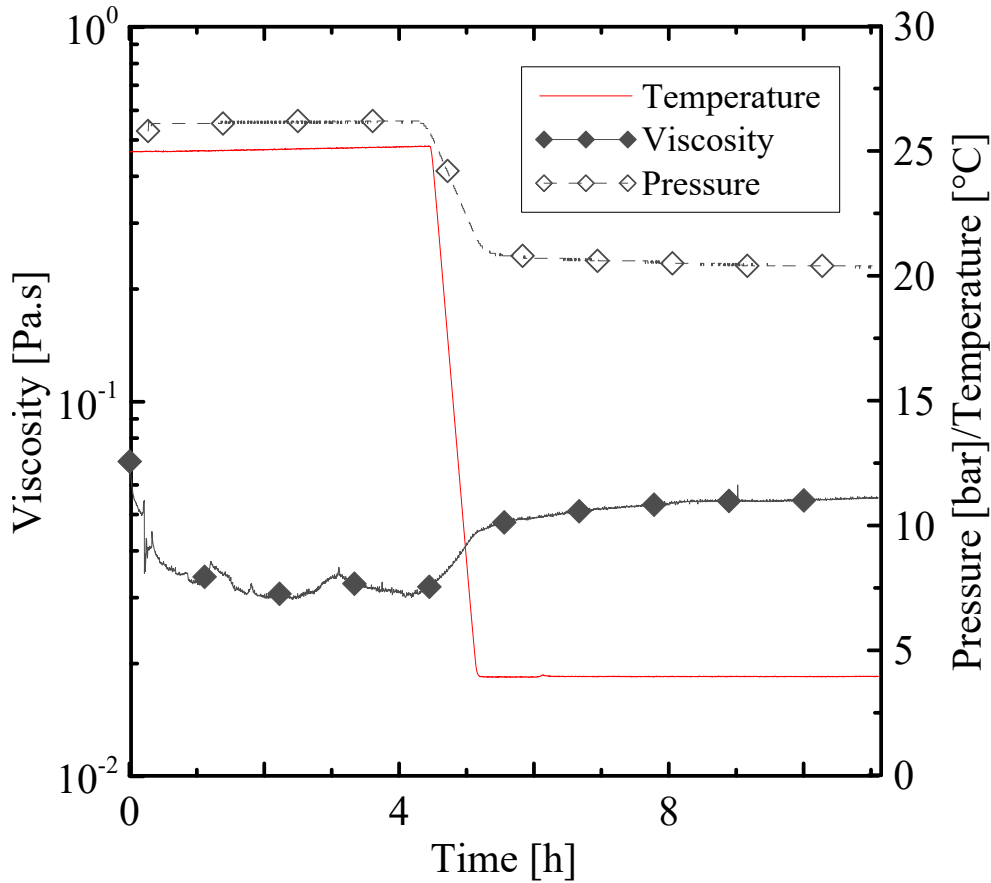


Figure 3.9: Example of a test performed with an initial pressure of 26 bar, 30% water volume fraction, shear rate of 700 s^{-1} and with concentric cylinder geometry.

3.6 Amount of water converted to hydrate

The amount of water converted to hydrate was determined using the data during the experiments conducted with the system closed, after the dissolution step. The real equation of state was applied through time following the procedure used by Sa et. al., [149], where $t = 0$ corresponds to the onset of hydrate formation, characterized by an abrupt increase in viscosity. Then, the fraction of water converted to hydrate was obtained by the following equation:

$$\frac{\eta_{w,t}}{\eta_{w,t_0}} = N \times \left[\left(\frac{PV}{zRT} \right)_0 - \left(\frac{PV}{zRT} \right)_t \right] \times \frac{1}{\eta_{w,t_0}} \quad (3-1)$$

where $\eta_{w,t}$ is the number of moles of water consumed to form hydrates at time t and η_{w,t_0} is the number of existing moles from the water volume fraction (WVF) of the emulsion inside the cell at the beginning of the test. The subscripts 0 and t correspond to the beginning and final test time, respectively.

N is the hydration number, P is the pressure of the system, V is the gas volume inside the cell, z is the compressibility factor, R is the gas constant, and T is the temperature of the system. The hydration number N was calculated by PVTsim Nova (Calsep A/S, Version 5.2) and the value employed was equal to 8.

4

Results and discussion

In this section, the experiments are presented through time sweep curves of viscosity and pressure during the dissolution, cooling, and induction time for hydrate formation. Important parameters like water volume fraction, shear rate, and degree of subcooling were assessed to analyze their effects on the amount of hydrate formation and the induction time. Also, some repeatability tests were done with different samples, to show the random behavior of hydrate formation and the reliability of the tests. For the experiments where the steady-state value of viscosity was captured, the water converted to hydrate was calculated and presented as a function of time, and a correlation between the steady-state relative viscosities and the amount of water converted into hydrate was proposed. A shear rate ramp was also performed for the tests that showed hydrate formation, which allowed a rheological analysis between rates and viscosities. In addition to the information already collected, the power-law model was applied. This section begins presenting the results obtained regarding the quantification of Span 80 needed in the emulsion using the concentric cylinders geometry. The next results address the rheological parameters that were varied to analyze the formation of hydrates contemplating the tests of the two geometries used.

4.1

Effect of Span80

As the surfactant employed (Span 80) to stabilize the emulsions acts as a hydrate inhibitor [125], some preliminary tests were performed to evaluate the effect of its concentration on hydrates formation. Those tests were performed using the geometry of concentric cylinders since the objective was only to evaluate the quantitative limitations of surfactant. All tests showed similar qualitative rheological characteristics in the first hours of the experiment. As it can be seen in Fig. 4.1, during the first 4 hours of experiments, the temperature was kept fixed and equal to 25 °C. The shear viscosity of the system decreased until reaching a plateau value that indicates the total saturation of the gas in the emulsion. The pressure also decreased due to the gas dissolution in the emulsion. It is worth mentioning that these tests in particular were carried out

with the valve closed from the beginning, when the experimental set pressure was reached. Then, during the dissolution step the needle valve was already closed, not allowing more gas to enter into the cell.

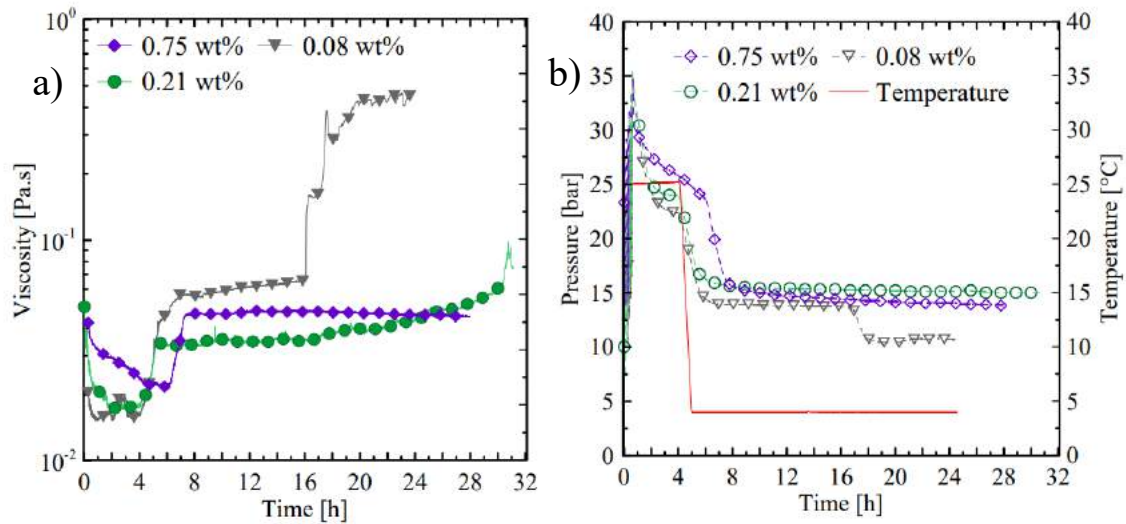


Figure 4.1: Effect of Span 80 concentration (wt%) on hydrate formation: (a) viscosity versus time, and (b) pressure versus time. Tests performed with 30% WVF, initial pressure of 35 bar, and shear rate $\dot{\gamma} = 700 \text{ s}^{-1}$.

During the second step, that is, in the temperature decreasing ramp where the temperature was linearly reduced from 25 to 4 °C at a rate of 0.7 °C/min, the viscosity had a slight increment and the pressure dropped around 6 bar. The decreased in pressure occurred as a consequence of the reduction in temperature. Regarding the viscosity, it increased with the reduction in temperature, but it can also decreased due to the higher dissolution of the gas in the liquid phase during this step. All tests took place with a shear rate of 700 s^{-1} , a initial pressure of 35 bar, with a subcooling of around 14.2 °C, and with 30% of water volume fraction (WVF). As noted in Fig. 4.1a, the first test performed was with 0.75 wt% of Span 80 (represented by the purple/losangle symbols). It is important to remember that this Span 80 percentage was calculated relative to the total amount of emulsion. The viscosity increased due to temperature decreased, and then remained constant. There was no hydrate formation, even after 20 h of testing in the stability zone. Moreover, Fig. 4.1b shows that pressure also reached a constant value, reinforcing that hydrates were not formed. So, the experimental condition was changed, reducing the concentration of Span 80.

As mentioned before, Karanjkar et al. [125] reported that Span 80 acts as an anti-agglomerant agent for hydrates. The authors observed that the

viscosity of the hydrate slurry was reduced as the Span 80 content was increased, improving the fluidity of the material. This fact was explained by the availability of surfactant in the oil phase, which readily and efficiently adsorbs on the hydrate-oil interface and thus prevents a strong interaction between hydrate particles. Therefore, to reduce the inhibiting effect of Span 80, another experiment was conducted with 0.21 wt% (represented by the green/circle symbols). It can be observed that the viscosity decreased in the dissolution step in comparison to the test performed with 0.75 wt% of Span 80, indicating that more gas was dissolved. Then, the viscosity slightly increased during the cooling, reaching a plateau, and at the time of around 16 h, it began to increase gradually until a small peak was noted, but no significant change was observed in the pressure. In this case, it seems that some hydrates crystals were formed, but the surfactant, together with sample shearing, attempted against hydrates crystals agglomeration.

Another test was performed by further reducing the Span 80 concentration to 0.08 wt% (represented by the gray/triangle symbols). This amount of surfactant guarantee the emulsion stability at rest for 2 h - enough time to initiate our test. After 16 h of the experiment, an abrupt increase in viscosity of approximately seven times in relation to the prior viscosity value and a concomitant pressure drop were observed, indicating gas consumption during a typical process of hydrate formation. The increment in viscosity was related to both a change from liquids drops to small solid particles (crystals) of hydrate and to the agglomeration of these crystals [17, 115]. At the end of the test, a steady state regime was reached due to an equilibrium between the cohesion forces among hydrate particles and shear forces that tend to break up the hydrates agglomerates [150–152]. It is important to note that in this work the steady state was always considered a few hours after the formation of the hydrate due to the fact that the gas consumption was minimal after formation and therefore there were no relevant changes in viscosity. It is worth noting that at the end of the cooling step the pressure was equal to 14 bar, and for these thermodynamic conditions the subcooling is 7 °C. Based on these results, it was considered a surfactant concentration of 0.08 wt% to be used in all the subsequent tests. Similar to what was indicated by Karanjkar et al. [125], it can be concluded that Span 80, in addition to helping the emulsion stability, acts as a hydrate inhibitor. The following tests were all done with the valve open only during the dissolution process step, allowing more gas to enter the system, and consequently, greater subcooling and shorter hydrate formation time.

4.2

Influence of rheological parameters on hydrates formation

4.2.1

Effect of pressure with concentric cylinder geometry

To verify the effect of pressure in the formation of hydrates, tests were performed with 30% WVF and with a shear rate of 700 s^{-1} . The results obtained are shown in Fig. 4.2. The temperature set during the entire test was represented by the red line. Importantly, repeatability tests were represented by dashed lines for viscosity and filled symbols for pressure. Fig.4.2a shows that during the gas dissolution step, a viscosity decrease was observed, as expected, while Fig. 4.2b shows the pressure variation during the test, where it can be observed that it remained constant for the first 4 hours. For the experiment with the pressure of 35 bar, it was noted that right after the cooling process, a strong viscosity peak was observed, which was associated with the growth and aggregation of the hydrate crystals [115]. However, the viscosity peak was followed by a sharp drop, indicating that the rheometer reached its maximum torque allowed and the assembly magnet-rotor of the pressure cell lost its communication with the external propulsion magnet [153–155]. Therefore, the experiment had to be stopped. This same behavior was observed by Silva et. al., [113] during their nitrogen tests. In this case, it was not possible to obtain steady-state values of pressure and viscosity after the formation, consequently, the water converted to hydrate could not be determined.

Due to this equipment limitation, two other tests were performed for lower pressures, at 30 and 25 bar. For the test conducted at 30 bar it was possible to identify the hydrate formation, since the viscosity increased about 10 times its value, and the pressure dropped around 7 bar close to 12 h of test. This steep increase in viscosity was followed to a smooth decrease until a steady-state regime was observed. As discussed above, increasing subcooling produces higher driving forces, leading to lower induction period [26,156,157]. This behavior can also be observed by the results of the test conducted at 35 bar, which presented a shorter induction period than the test performed at 30 bar.

The gas amount also increases with the subcooling, which can lead to higher mass transfer rates to the hydrates and, therefore, lower induction times [47]. Fig. 4.2b shows the characteristic pressure drop during the hydrate formation for the test conducted at 30 bar. After this drop in pressure, an asymptotic value was reached, indicating that the rate of water converted to hydrate was substantially reduced at the end of the test. For the experiment

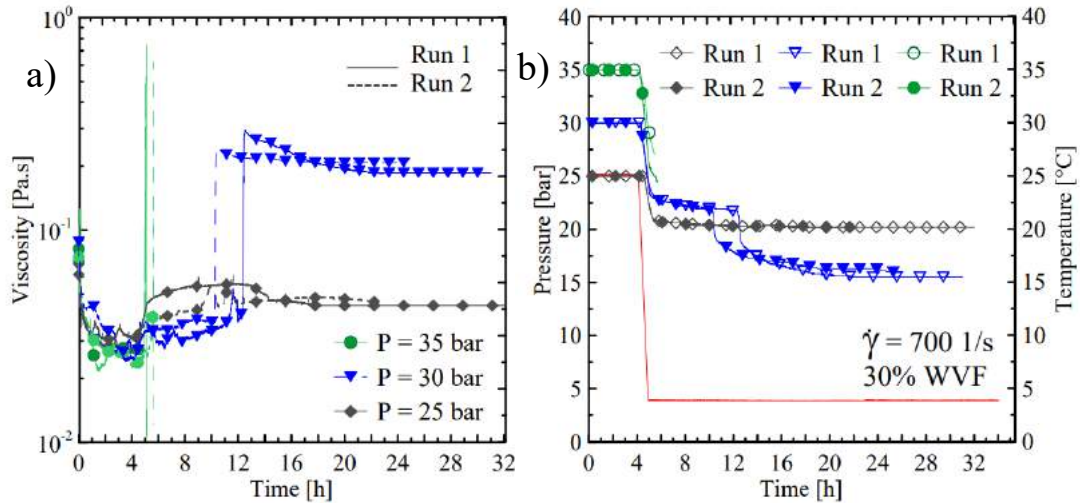


Figure 4.2: Effect of pressure on hydrate formation: (a) viscosity *versus* time, and (b) pressure *versus* time. Run 1 and run 2 represent two tests made with the same conditions, and different samples. Pressure of 25, 30, and 35 bar were represented by gray/losangle, blue/triangle down, and green/circle lines, respectively. The temperature was represented by the red curve.

at 25 bar (subcooling of 8 °C) no hydrate formation was verified for up to 20 h of test it was because the driving force for hydrate formation was decreased. These results were in qualitative agreement with the results observed by Webb et. al., [153] with methane hydrates.

The results presented in Fig. 4.2 showed that there was a hydrate formation window for the system employed, emulsion, thermodynamic conditions applied, and equipment limitations. Below this window, hydrates did not form, and above this, hydrates formation was so strong that the maximum torque of the rheometer was exceeded. The hydrate formation window stated showed good confidence as can be observed in the repeatability tests. Only the test with 30 bar showed a difference in the induction period, of around two hours. It is noteworthy that the hydrate structure formed in the experiments was similar to that seen in Fig.2.4f. The hydrate structure removed from the cell had a porous aspect because it was dynamically formed due to the imposed shear rate. It is noteworthy that the greater the applied pressure, the greater the subcooling. This is due to the fact that the temperatures during the tests were the same, and subcooling is the difference between the test temperature and the temperature where the gas is in the metastable zone at constant pressure.

4.2.2

Effect of pressure with vane geometry

To analyze the effect of pressure, tests were performed with different subcooling, for a pressure range from 26 to 31 bar, with a shear rate of 40 s^{-1} , and 30% WWF.

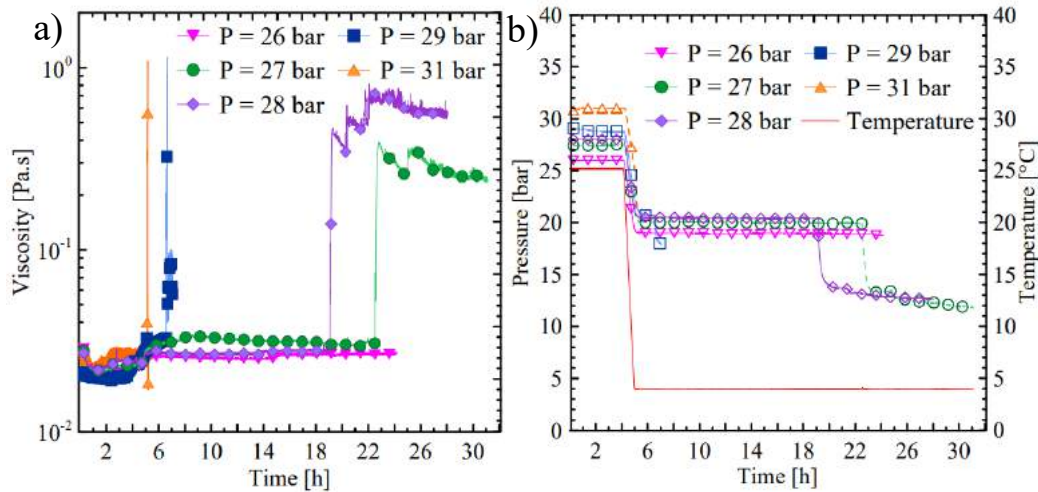


Figure 4.3: Effect caused by the subcooling on hydrate formation: (a) viscosity versus time, and (b) pressure versus time. Tests performed with 30% WWF and 40 s^{-1} .

The experiments at 31 and 29 bar showed similar behavior as seen in Fig. 4.3. After the cooling process, an abrupt increase in viscosity was verified, and the rheometer reached the maximum possible torque, indicating that a high amount of hydrates were formed [153–155]. In these cases, when the tests were completed and the rotor removed from the cell, it was possible to observe a hydrate block formed in the shape of the geometry (see Fig. 4.4). The hydrate block had a porous structure with a spongy appearance. It was possible to notice that the block was not a rigid structure like ice and the contained gas began to dissipate. Inside the cell a small amount of liquid emulsion was checked. This same scenario was observed in the concentric cylinder geometry experiments discussed previously, and shown in Fig. 4.2. Both geometries reached the maximum rheometer torque when the tests were submitted to the highest subcooling.

For this reason the subcooling was reduced in order to obtain the slurry rheology within the measuring torque of the rheometer. As discussed earlier, higher pressures increases the driving forces and, therefore, the agglomeration of the hydrate particles becomes more intense, and hydrates form faster [113]. This behavior was verified in the tests performed at 28 and 27 bar (see Fig. 4.3).

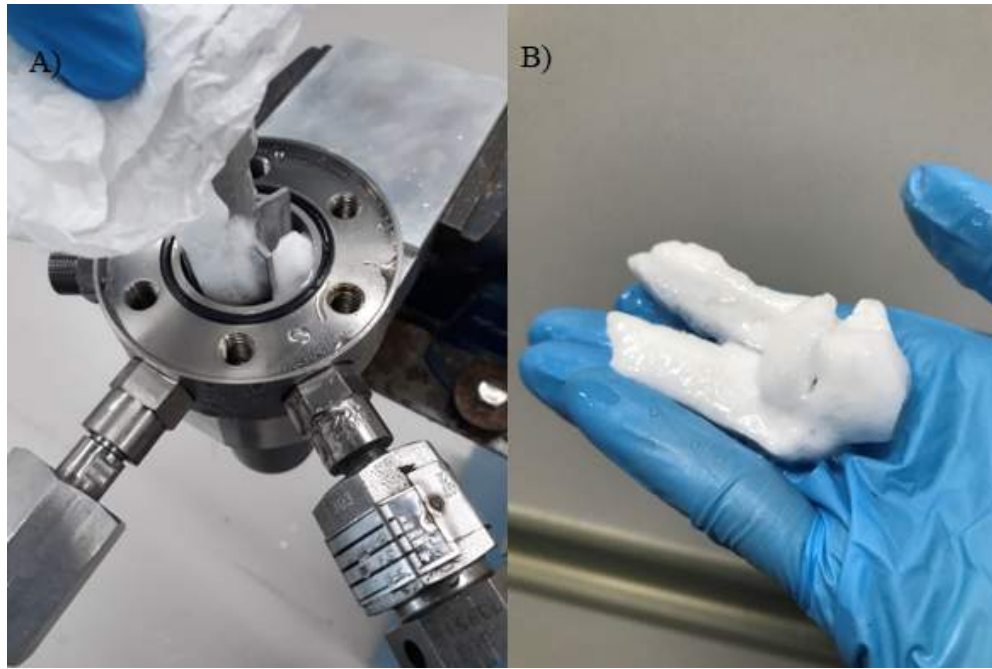


Figure 4.4: Hydrate block (a) being pulled out of the cell and (b) hydrate removing from the cell using the vane geometry.

It was noted that the induction period was different in 4 h between the test performed with 28 and 27 bar and different times to reach the steady state were also detected.

To complete this analysis, another test was done at 26 bar, represented by the downward pink triangle. After 22 hours of experiment, hydrates formation was not observed, which could be associated with the small subcooling obtained with the experiment at 26 bar in comparison with the other tests. To gain more confidence about the results obtained with the test performed at 26, 28, and 31 bar, another similar experiments were conducted, and the same behavior was confirmed, indicating a good repeatability (see Fig. 4.5). In the repeatability tests it was possible to notice a small drop in viscosity after the formation of hydrates for the test performed with 28 bar, which did not happen in the first test with this same pressure (see Fig. 4.3). Even with this small drop, the pressure remained stable after the formation of the hydrate, as seen in Fig. 4.5b. That is, this drop did not interfere in gas consumption. The test with the pressure of 31 bar only showed a difference around 1 hour in the induction period as well as with the pressure of 28 bar. This behavior enhanced the repetitive pattern of the hydrate for formation but showed that the same peak viscosity will not necessarily be reached.

Similar to what was observed in the concentric cylinders geometry, hydrate formation was restricted to a small operational window. Regarding the results obtained with both geometries, and recalling that the shear rates

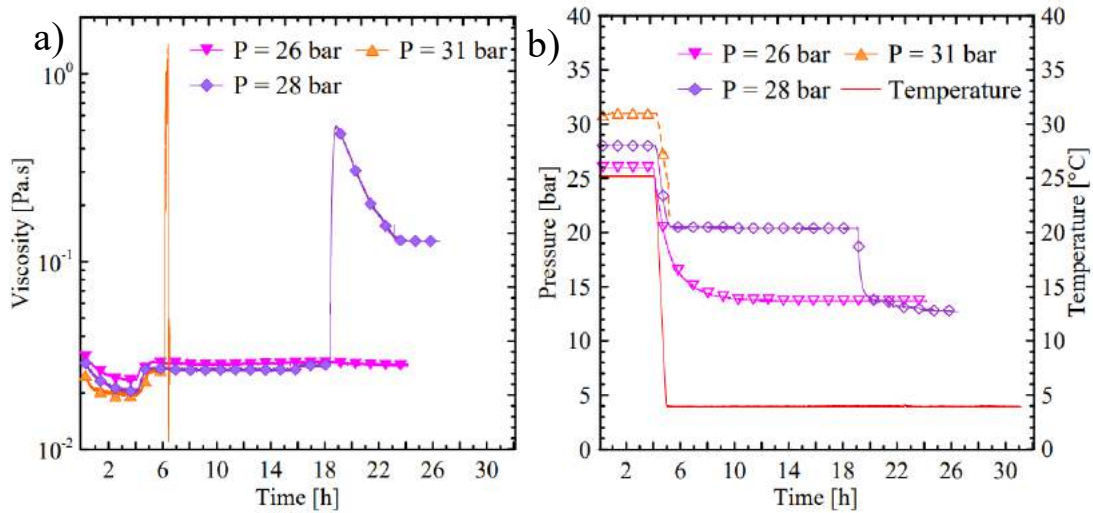


Figure 4.5: Repeatability tests of subcooling on hydrate formation: (a) viscosity versus time, and (b) pressure versus time. Tests performed with 30% WVF and 40 s^{-1} .

used in the concentric cylinder geometry ($\dot{\gamma} = 700 \text{ s}^{-1}$) was much higher, it was observed that the operational range of pressure for the vane geometry was slightly lower: 27-28 bar, while it was 30-31 bar for the concentric cylinders. Different shear rates were used for each geometry because the vane geometry was built in the PUC-Rio laboratory and had to undergo calibrations. During this process it was noticeable that for this geometry small shear rates would be enough to work. Reiterating that both geometries presented the same non-Newtonian rheological behavior where the greater the subcooling applied, the shorter the induction time, and the higher the value reached by the viscosity. Webb et. al. [153], Anklam and Firoozabadi [157], Silva et. al. [113], and Arjmandi et al. [156] have also reported this same behavior in literature.

Webb et. al. [153] reported that the rheological behavior of hydrate slurries depends on the experimental conditions like initial pressure and temperature. Hydrate viscosity increased with increasing initial pressure and decreasing temperature. The driving force for hydrate formation increases with increasing pressure and decreasing temperature.

4.2.3

Effect of shear rate with concentric cylinders geometry

To analyze the effect of shearing on hydrate formation, tests were performed for emulsions with 30% WVF and pressure of 31 bar. The results are presented in Fig. 4.6. The shear rates applied were 600, 700, 750, and 800 s^{-1} .

It was possible to notice in Fig. 4.6a that all tests showed a viscosity decrease during the time of gas dissolution, and an increase in viscosity during the cooling process, as expected and analyzed previously. The pressure variation at these steps also followed the same trend as described above (see Fig. 4.6b). The pressure drop during the cooling step, around 8 bar, was similar for all cases.

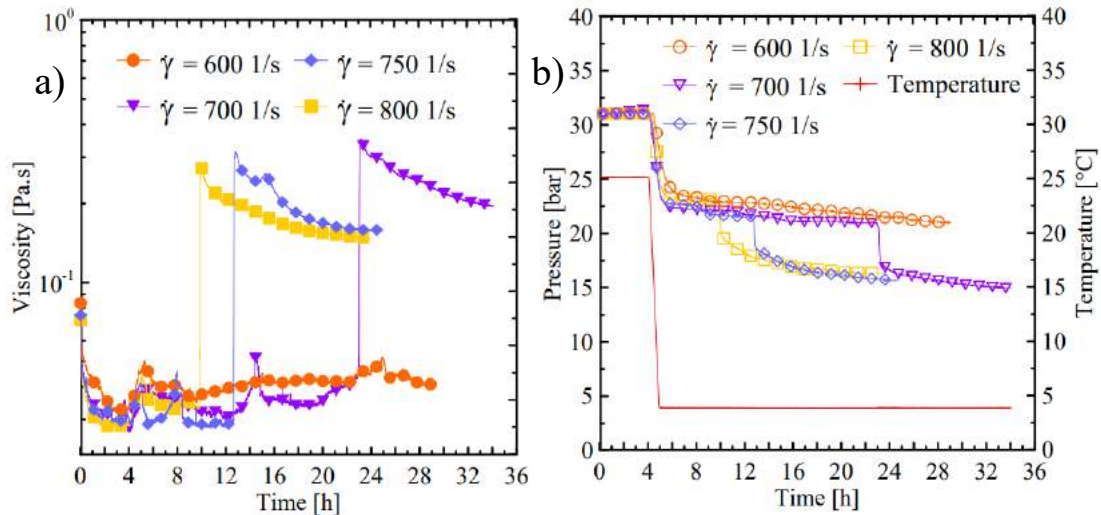


Figure 4.6: Effect caused by the shear rate on hydrate formation: (a) viscosity *versus* time, and (b) pressure *versus* time. Tests performed with 30% WVF and initial pressure of 31 bar.

Regarding the effect of shear rate, for the case of the lowest shear rate used, equal to 600 s^{-1} , there was a slight increase due to the temperature ramp as explained above and, after more than 28 hours of testing, the viscosity remained roughly at this same value, indicating no hydrate formation, see Fig. 4.6a. Also, Fig. 4.6b shows that after the cooling process, the pressure dropped around 2 bar in 24 hours, but at this condition insufficient mixing of the constituents was generated and no hydrates were formed in the experimental period analyzed [114, 158].

For higher shear rates, 700, 750, and 800 s^{-1} , it was observed an abrupt increase in viscosity and decrease in pressure after some time from the cooling, indicating that hydrates were formed. For the experiment conducted at $\dot{\gamma} = 800 \text{ s}^{-1}$, represented by yellow/square symbols, a shorter induction period was noted, compared to the other tests. The onset of hydrate formation was perceived in approximately 5 h. As the shear rate decreased, the induction period increased [47]. This behavior had already been previously studied. Douieb et al., [121] and Sandoval et. al., [152] attributed it to a higher interfacial contact among hydrate constituents [114, 159]. It was also

noteworthy that the morphology of the hydrate aggregates generated may differ significantly when they are formed at different shear rates [160].

After the viscosity increased, a steady state regime was obtained in all cases considering that the consumption of gas occurs slowly indicating that no more hydrate structure will be formed, so it can be considered a steady state. So it can be noted that, for this results, a steady state regime was reached for the higher shear rates. It is well-known from the literature that the time to reach steady state increases as the shear rate decreases, due to a slower rearrangement of the microscopic state [161, 162]. In other words, when a balance between cohesion and shear forces (agglomerate and break) is obtained, a steady-state regime is reached [152].

It can still be seen in Fig. 4.6a some viscosity instabilities during the hydrate stability zone for the tests performed with shear rates of 600, 700, and 750 s^{-1} . This behavior can be related with a possible formation of some hydrate particles and dissociation (without achieving the critical nucleus). Some of these tests were repeated and the same qualitative trends were found in the induction period, although the viscosity value showed a slight difference. These results can be seen in Fig. 4.7

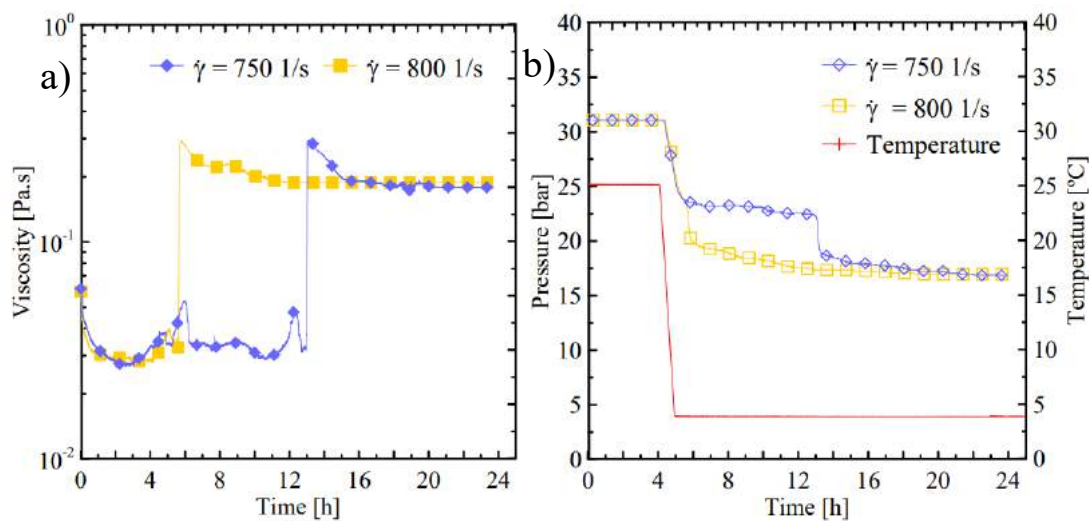


Figure 4.7: Repeatability tests with shear rate variation: (a) viscosity versus time, and (b) pressure versus time. Tests performed with 30% WVF and initial pressure of 31 bar.

Repeatability tests performed with the shear rates of 800 and 750 s^{-1} are represented by the yellow/square and blue/lozenge lines, respectively. It was notorious the similar behavior to the initial tests carried out at the same rates, where the higher rates tend to form hydrates more quickly. And just like

in Fig. 4.6 similar viscosity values were reached during the steady state. For the experiments in Fig. 4.7b it was still possible to notice that the pressures reached the same levels in 22 hours of test. This same behavior was seen in Fig. 4.6b with 16 hours of testing.

4.2.4

Effect of shear rate with vane geometry

To analyze the influence of shear rate with the vane geometry, tests were at 31 bar, and 0.08 wt% of span 80 for emulsions of 90 g. Figure 4.8 shows the results obtained for the shear rates range from 28 to 40 s^{-1} . It can be noted that when the highest shear rates were applied, 40 and 35 s^{-1} , the same scenario of large hydrate formation was measured, and the maximum rheometer torque was reached.

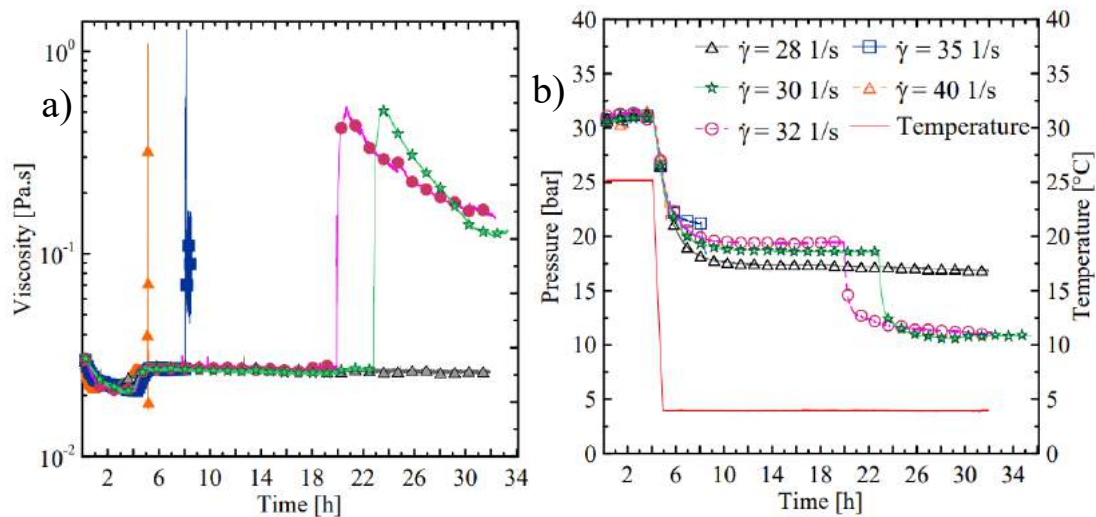


Figure 4.8: Behavior of: (a) viscosity versus time and (b) pressure versus time for different shear rates. Tests performed with 30% WVF, and pressure of 31 bar.

For lower shear rates, 30 and 32 s^{-1} , hydrates were also formed, but the viscosity peak was not so severe, being possible to capture the behavior of the material during the steady-state at the end of the test. A drop in viscosity was verified soon after forming hydrate and this happened because the cohesive force was lower than the rupture force. The vane geometry provides formation and soon after there was some level of breakdown of the formed compound until it stabilizes and remains permanent. It can be seen in Fig. 4.8a that within the hydrate formation envelope but before the onset of hydrate formation, between 6 and 18 hours, the viscosities of both tests had a similar value of 0.028 Pa.s.

After 20 hours of testing at $\dot{\gamma} = 32 \text{ s}^{-1}$, an increase in viscosity of more than 10 times was noted, while for $\dot{\gamma} = 30 \text{ s}^{-1}$ this increase was observed in 23 hours, so the induction times were 0.5, 3, 15, and 18 h for the experiments performed with $\dot{\gamma}$ of 40, 35, 32, and 30 s^{-1} , which means that this period for hydrate formation increased as the shear rate decreased, in accordance to what was observed in the concentric cylinders geometry [47, 153, 160]. Just after the viscosity peak of hydrate formation, the viscosity dropped, due to the break down of hydrate agglomerates caused by the imposed shear rate. Fig.4.8b shows the asymptotic pressure drop in both tests until reaching a steady state, similar behavior obtained for the geometry of concentric cylinders. In the last experiment, a shear rate of 28 s^{-1} was applied, and it was observed that the viscosity and the pressure remained constant throughout the test, even after 27 h on the hydrate equilibrium zone, indicating that hydrates were not formed.

The pressure drop during the cooling step increased with the reduction in the shear rate. This fact was because, at the end of the dissolution step, each test departed from the same pressure but with a different amount of gas. The amount of ethane gas sent from the pump to the cell for the tests with shear rates of 32, 30, and 28 s^{-1} at the end of the dissolution process were 356.6 ml, 344.6 ml, and 327.3 ml, respectively. That is, at the beginning of the cooling process, the test conducted with the shear rate of 28 s^{-1} had the lowest amount of gas inside the cell, and it was the one that consumed more gas during the cooling process, yielding the largest pressure drop. Clearly, this fact affects the subcooling and, therefore, the hydrate formation kinetic.

As for concentric cylinders, the vane geometry showed the same behavior where the higher the rate, the shorter the induction and steady state time [121, 152]. And even with the variation of the shear rate, the values that the viscosity reached at the time of hydrate formation were very similar among the rates of 30 and 32 s^{-1} . This similarity can be justified in the vane geometry due to the small difference between the applied rates of 30 and 32 s^{-1} . With this, it can be verified that the rates make a difference in the induction and steady state time but not necessarily in the viscosity value reached in the steady state.

This behavior is opposite to that observed by Ding et. al. [159] with natural gas hydrates, where the higher the rate the lower the viscosity, but they also varied the amount of water at the same time which was not performed in the experiments above. With a mixture of methane and propane gas, Charin et. al., [114] also found a different behavior. There was no standard behavior between rate and viscosity value at steady state. It is noteworthy that none of the geometries used in these experiments were the same as those used in this study, where the cited authors used an external mixer and a modified vane

geometry with an opening between vanes, respectively.

4.2.5

Effect of water volume fraction with concentric cylinders geometry

Another important parameter that influences the formation of hydrates is the water volume fraction (WVF). The amount of water droplets dispersed in the continuous phase of the emulsion affects its viscosity and stability [24]. Moreover, since the water is responsible for encapsulating the gas molecules, the water cut will directly affect the amount of hydrates formed [117].

Fig. 4.9 shows the results for a series of tests performed with 25, 30, and 35% WVF. All experiments were subjected to a shear rate of 800 s^{-1} and a pressure of 31 bar. Hydrate formation occurred in all the experiments. The induction periods for the experiments performed with 25, 30, and 35% WVF were 6, 5, and 4 h, respectively. So, the induction period was reduced with the increment in the WVF. Regarding the steady-state slurry viscosity after hydrate formation, it can be observed that it increased as the water volume fraction increased. In Fig. 4.9b, it is possible to notice that after 16 hours of testing the pressures were equal in the same steady state by differentes WVF. That is, the steady state of the hydrate slurry viscosity indicated that capillary bridges no longer appeared and, consequently, there was no more attraction among hydrate crystals in the system, and therefore gas was not consumed, and pressure remains constant [163].

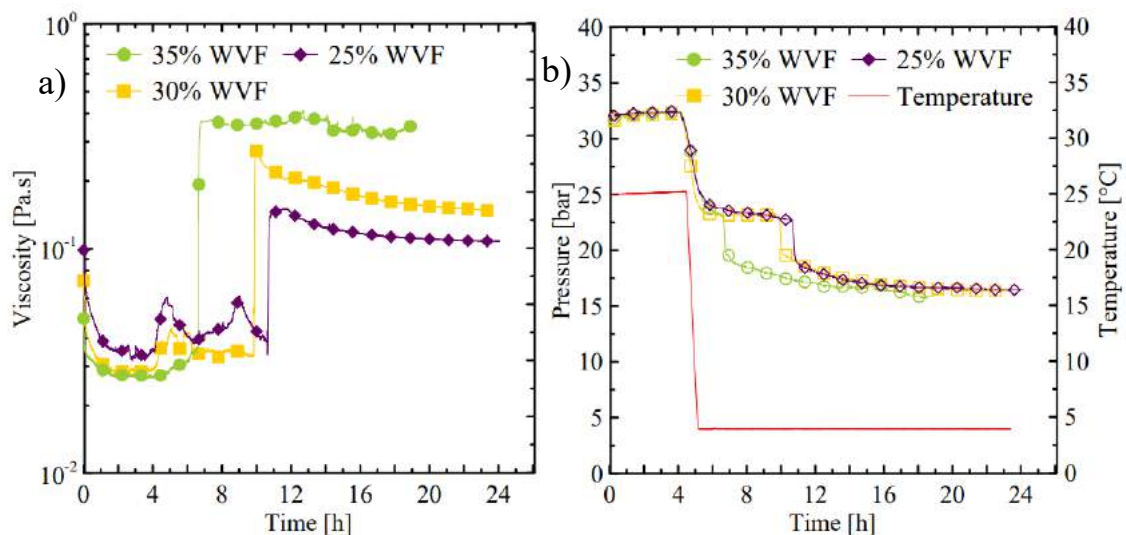


Figure 4.9: (a) Variation of viscosity *versus* time, and (b) pressure *versus* time for different water volume fraction. Pressure of 31 bar, and shear rate of 800 s^{-1} .

Yang et al. [163] observed that the effect of water volume fraction (WVF) on the viscosity achieved just after hydrate formation can be associated with the appearance of more capillary bridges in the system enhancing the attraction among hydrate crystals, and therefore, increasing the agglomerate size [164]. Ding et al. [159] and Qin et al. [5] also observed that the emulsions with higher water volume fractions generate larger amount of hydrates. Sandoval et. al., [152] also reported this same behavior with them experiments performed at atmospheric pressure. They even varied the shear rate during the experiments for different WVF and noted the shear thinning behavior of the emulsion prior to hydrate formation for the experiments with 20, 30, and 40% WVF, where the viscosity dropped about 60, 40, and 27 times, respectively, when the shear rate was increased from 0.1 to 10 s⁻¹. In general, the greater the amount of water in the emulsion, the greater the number of water molecules with hydrogen bonds between them. Due to this, more gas encapsulated and faster the nucleation process explained in Fig.2.4.

4.2.6

Effect of water volume fraction with vane geometry

The tests were performed at 31 bar and a shear rate of 32 s⁻¹ using a water volume fraction equal to 25, 30, and 35%. Fig. 4.10 shows the viscosity and pressure varying with time obtained throughout the tests.

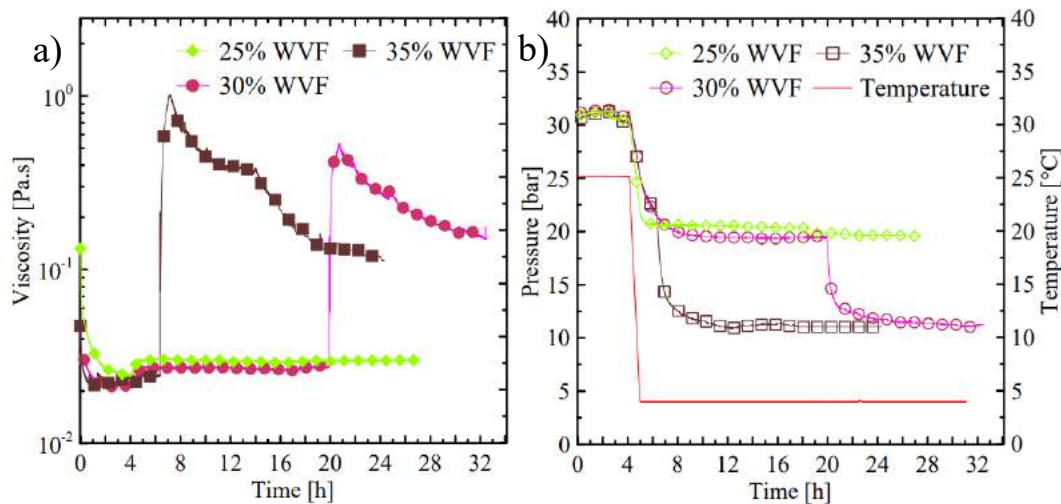


Figure 4.10: Effect caused by the water volume fraction on hydrate formation: (a) viscosity versus time, and (b) pressure versus time. Tests performed with a shear rate of 32 s⁻¹, and initial pressure of 31 bar.

The test revealed that hydrate formation did not occur for 25% WVF.

The performed tests for higher water volume fraction than 25% showed hydrate formation, with the induction period decreasing as the water cut increased, following the same trend of the concentric cylinders experiments. It was possible to notice more two similarities with the geometry of concentric cylinders: the greater the amount of water in the emulsion, the greater the peak viscosity reached during the hydrates formation; and in Fig. 4.10b, after 23 hours of testing, the pressures reached similar steady state regardless of the WVF value applied in the test, which also indicates that capillary bridges no longer appeared [152]. The vane geometry presents a different profile of viscosities when compared to what was seen for concentric cylinders. This fact can be justified due to the breakdown of hydrate particles caused by the blades of the geometry [145,165]. As the particles break down and become smaller in size, the viscosities begin to stabilize until they reach a steady state.

The water volume fraction parameter is one of the most assessed in literature. Yan et. al. [163], Qin et. al., [5], Ding et. al., [159], Webb et. al., [17], and Charin et. al., [114] have been some of the authors who have studied this issue. The discussions raised by the authors was discussed above for concentric cylinders and in the part where some studies on hydrates were presented.

4.3

Amount of water converted to hydrate

The amount of water converted to hydrate is an important information that indicates the change from liquid water droplets to a solid phase. Indeed, it is essential to correlate this phase change with the rheology. The pressure drop data after hydrate formation presented for the different parameter assessed was used to calculate the amount of water converted to hydrate using the equation of state (equation 3-1).

4.3.1

Influence of pressure

Fig. 4.11 and Fig. 4.12 shows the amount of water converted to hydrate for different pressures, referring to the tests of the Fig.4.2 for the concentric cylinder geometry and Fig. 4.3 for the vane geometry, respectively.

The Fig. 4.11 shows that the amount of water converted to hydrate gradually increased with time, tending to an asymptotic value. That means, that gas was consumed during the formation of hydrates and the asymptotic trend reached was due to mass transfer limitation proving that a phenomenon of kinetic limitation occurs [47, 166], therefore, the percentage of water converted never reaches 100% [116].

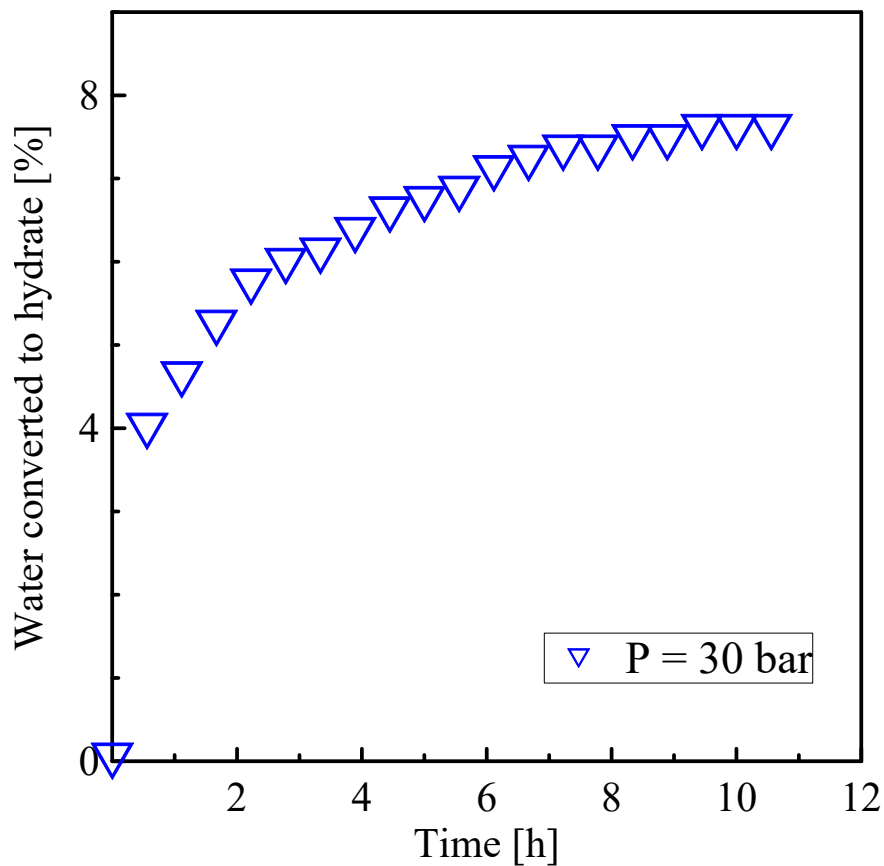


Figure 4.11: Effect of the pressure on the water converted to hydrate. The pressure used was 30 bar with 30% of water cut in the emulsion and with a shear rate of 700 s^{-1} .

Fig. 4.12 related to vane geometry shows that the fraction of water converted to hydrate formed in both tests was roughly the same, around 10%. Since the viscosity for 28 bar was almost the double of that found in the 27 bar test (see Fig. 4.3), it can be concluded that this difference was due to the presence of agglomeration of hydrate crystals. Majid et. al., [164] and Webb et. al., [153] studied that this behaviour could be associated with the appearance of more capillary bridges in the system enhancing the attraction among hydrate crystals, and therefore, increasing the agglomerate size, and consequently the viscosity. It can be noted that the vane geometry converted more water than the concentric cylinders and presented a better efficiency in terms of converting water. But a specific comparison was more limited in making because the geometries have been subjected to different shear rates.

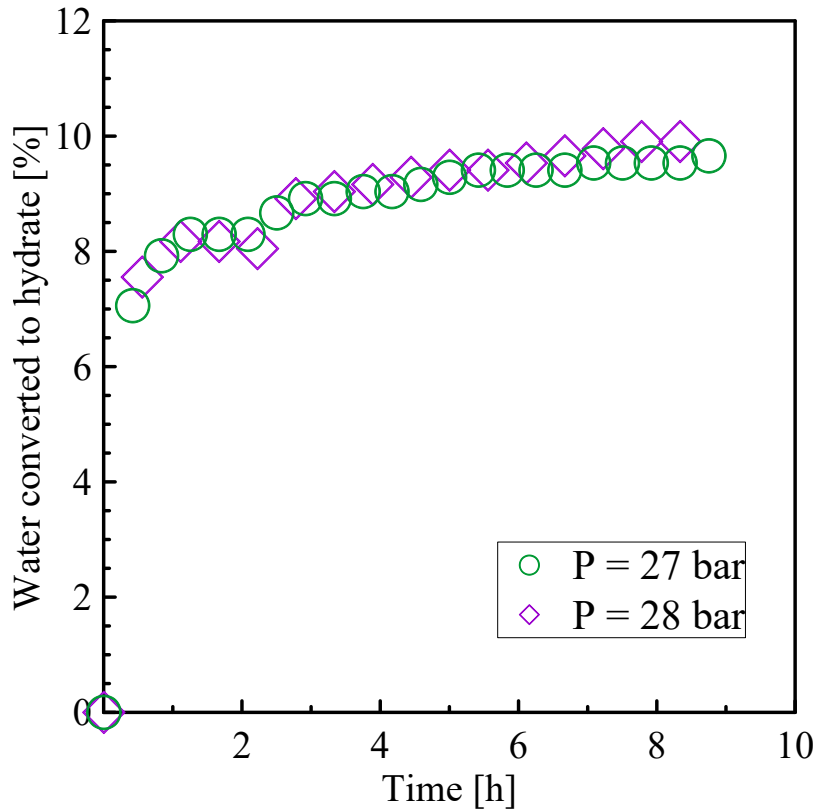


Figure 4.12: Water converted to hydrate for different pressures using the vane rotor. The water cut used was 30% and the shear rate applied was 40 s^{-1} .

4.3.2 Influence of shear rate

Fig. 4.13 below displays the amount of water converted to hydrates for different shear rates, using the data obtained in Fig. 4.6 with concentric cylinders.

The highest amount of water converted to hydrate was obtained with the test performed with $\dot{\gamma} = 800 \text{ s}^{-1}$, while the experiments with shear rates of 700 and 750 s^{-1} showed roughly the same amount of water converted. This can be contextualized based on the analysis of one factor. Bassani et. al., [116] studied that water can be trapped within the porous structure of the hydrates. So, it can be seen in Fig. 4.6b that the pressure drop was very similar between tests but the test with shear rate of 800 s^{-1} showed a less abrupt pressure drop. Therefore, the difference between tests in the amount of water converted may be associated with more water retained in porous hydrate structures than in greater gas consumption or hydrate formation [47, 116, 166].

The water converted to hydrates for the shear rates of 30 and 32 s^{-1} with the vane geometry was determined and shown in Fig. 4.14. The results were

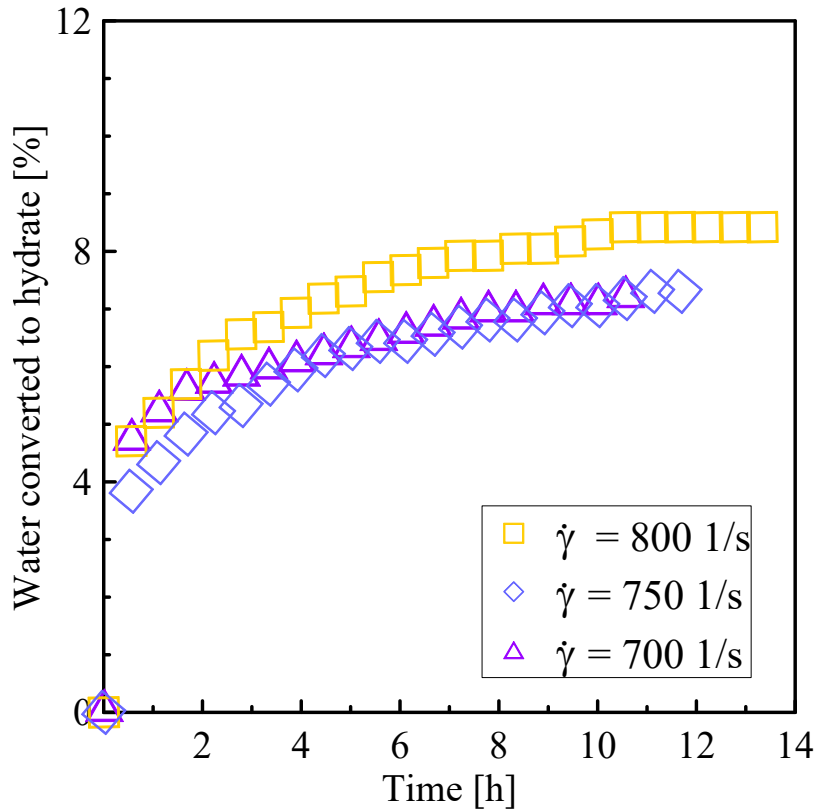


Figure 4.13: Water converted to hydrate for different shear rates. The pressure used was 31 bar with 30% of water cut in the emulsion.

similar to that found for concentric cylinders for the rates of 700 and 750 s^{-1} . As previously explained, the curve for this ratio of water converted with time will present this asymptotic characteristic. This behavior was seen for both geometries.

The pressure drop observed at the exact moment when hydrate was formed (see Fig. 4.8) was practically the same between tests, which contextualizes this similarity in the first hours of converted water. But after 8 hours, see Fig. 4.14, it was possible to notice a small difference between the amount of water converted between the tests, which can be associated with the mass transfer limit between them [47, 116, 153].

The largest amount of water converted to hydrate for the concentric cylinder geometry was around 8% (as shown in Fig. 4.13), while for the vane geometry it was around 10%. This discrepancy can be due to the difference in the gas dissolution that each geometry provides through its mixture and the different subcooling.

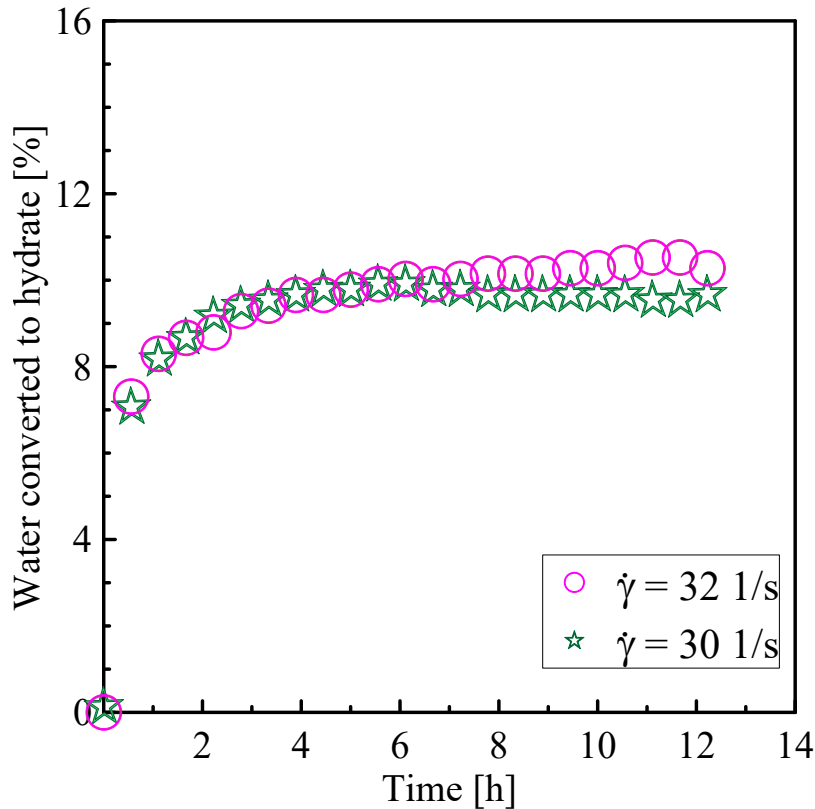


Figure 4.14: Water converted to hydrate for different shear rates. The water cut used was 30% and the pressure applied was 31 bar.

4.3.3 Influence of water volume fraction

Fig. 4.15 shows that the amount of water converted to hydrates was the same for the tests with 30 and 35% WVF. These values of water converted were a little higher than those formed for the test with 25% WVF.

It was important to note that besides the amount of hydrates formed, agglomeration also plays a role in the final slurry viscosity. This could be observed by comparing the values shown in Fig. 4.9. The difference in viscosity between the tests with 25 and 35% WVF was around 350%. Such a big discrepancy was not determined in the amount of water converted (see Fig. 4.15), since the difference was only less than 12%. The same comparison holds for the 30 and 35%, where practically the same amount of water was converted but a large difference in viscosity was noted. These comparisons indicate that most of the viscosity increase in Fig. 4.9 was likely due to hydrate particle agglomeration.

Fig. 4.16 shows the amount of water converted to hydrates for tests with 30 and 35% WVF using the vane geometry. As can be seen, the water converted

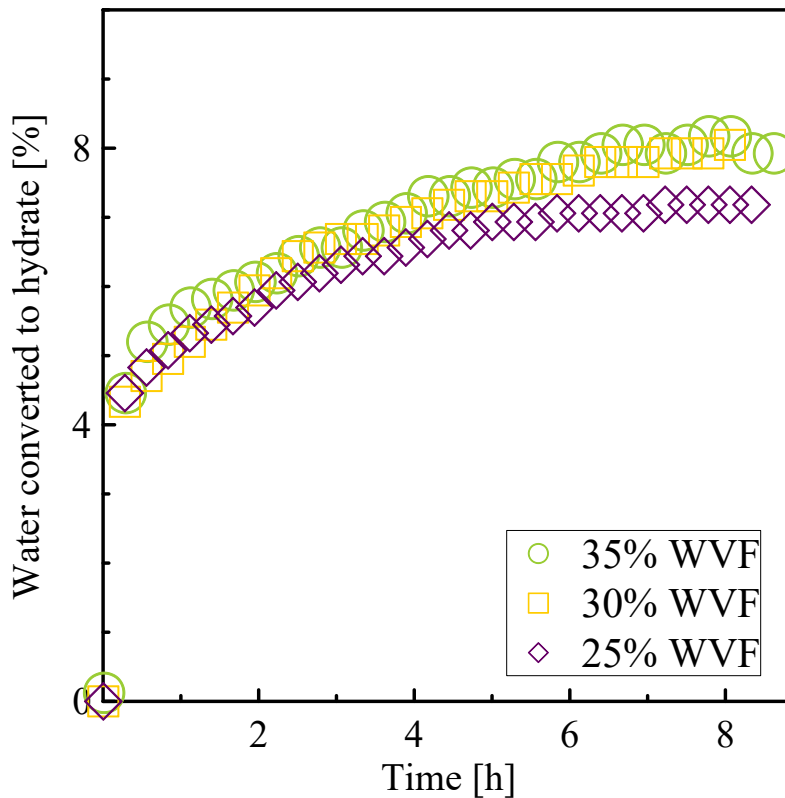


Figure 4.15: Water converted to hydrate for different amounts of water in the emulsion. The pressure used was 31 bar and the shear rate applied was 800 s^{-1} .

to hydrate formed with 35% WVF was much higher than the test with 30% WVF.

The difference between the curves using the vane rotor was larger than the ones seen for the concentric cylinders geometry (see Fig. 4.15 and Fig. 4.16). If only the tests with the vane geometry of water converted to hydrate were analyzed (see Fig. 4.12, Fig. 4.14, and Fig. 4.16) it was possible to notice that parameter that most influenced the result was the water cut. In Fig. 4.16, a difference in more than 3% of water converted between the tests was observed. Thus, different from what was observed for the concentric cylinders in terms of agglomeration, the difference in viscosity (Fig. 4.10), as well as in the water converted into hydrate (Fig. 4.16), may actually be associated with greater formation of hydrates. As Qin et. al., [5] said, the vane rotor has the ability to maintain dissolved gas content suggesting the presence of secondary axial flows, which may work to increase hydrate formation due to better fluid mixing.

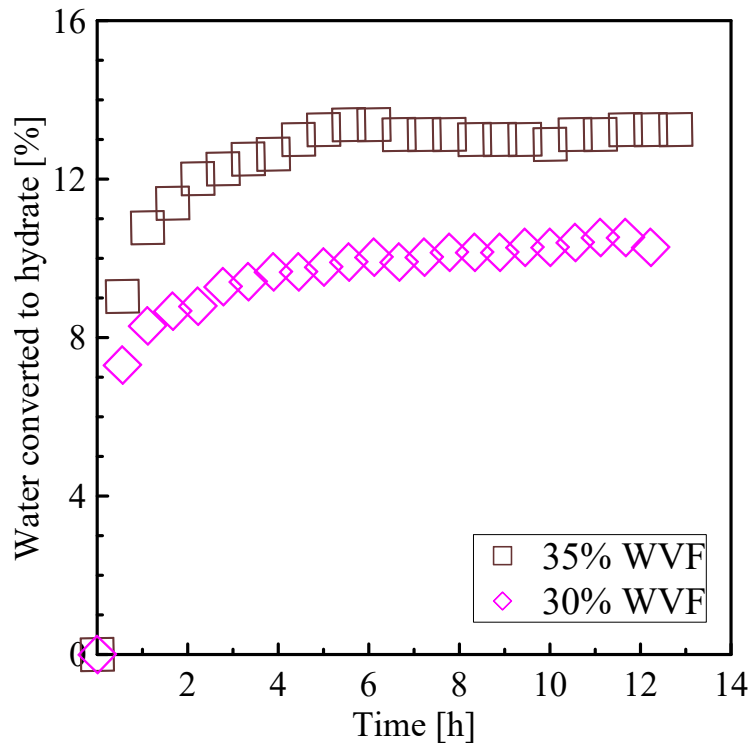


Figure 4.16: Water converted to hydrate for different emulsion compositions. The pressure used was 31 bar and the shear rate applied was 32 s^{-1} .

4.4

Correlation between relative viscosity and the amount of water converted to hydrates

The relative viscosity was correlated to the amount of water converted to hydrate for the tests with different water volume fraction for both concentric cylinder and vane geometries. The relationship was yielded with the viscosity values taken from the steady state regime. The relative viscosity refers to the phase change when hydrate formation was identified. So, the relative viscosity was defined as the ratio of the viscosity measured throughout the test to the viscosity before hydrate formation at $4 \text{ }^\circ\text{C}$, once the system reaches the established thermodynamic conditions of formation. The results obtained are depicted in Fig. 4.17 for the concentric cylinders geometry.

Different observations can be drawn from Fig. 4.17: a) the water converted into hydrate increased with increasing the water cut, and therefore, higher relative viscosity values were measured. If more water was available, higher amount of hydrate particles were formed which influences the viscosity value; b) For the highest water cut (35%), a similar percentage of water converted to hydrate was achieved, independently of the shear rate. As discussed earlier, during hydrate formation, the gas was consumed by the water

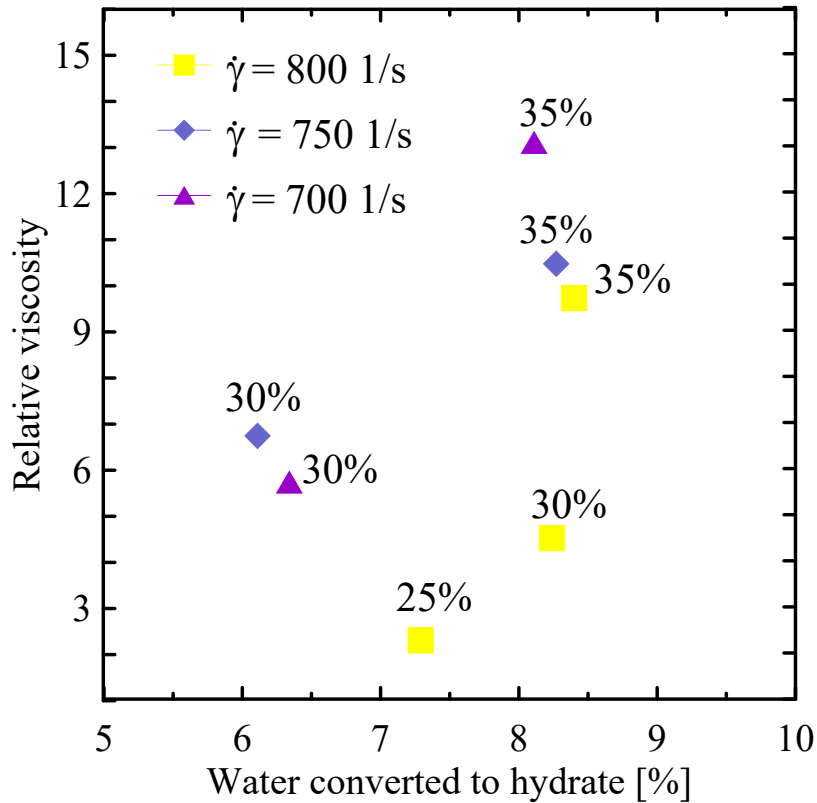


Figure 4.17: Relative viscosity *versus* water converted to hydrates for different shear rates. For each shear rate a variation of water volume fraction was applied. Pressures of 31 bar.

and an asymptotic trend was reached due to the mass transfer limitation [8]. With this, from a certain water cut value, this limitation will happen for a certain range of the applied rate; c) the amount of water converted to hydrate for the tests conducted at $\dot{\gamma} = 800 \text{ s}^{-1}$ and with 30 and 35% WVF were analogous, however, the relative viscosity values were different. This viscosity discrepancy can be related with more hydrate agglomeration caused by the presence of more available water around the hydrate particles; d) For the same water volume fraction, the relative viscosity decreases with the increment of the shear rate (with exception for a test with 30% WVF and $\dot{\gamma} = 750$ or 700 s^{-1}). That means, higher shear rates, more break down hydrate structures.

Fig. 4.18 shows the relationship between the relative viscosities and the amount of water converted into hydrates was analyzed for the vane geometry using two ranges of water cuts and shear rates (note that the experiment conducted with 20% WVF did not form hydrates and for 40% WVF the rheometer was blocked).

Based on Fig. 4.18, analogous qualitative results were obtained regarding those achieved with the concentric cylinders geometry. Firstly, the water

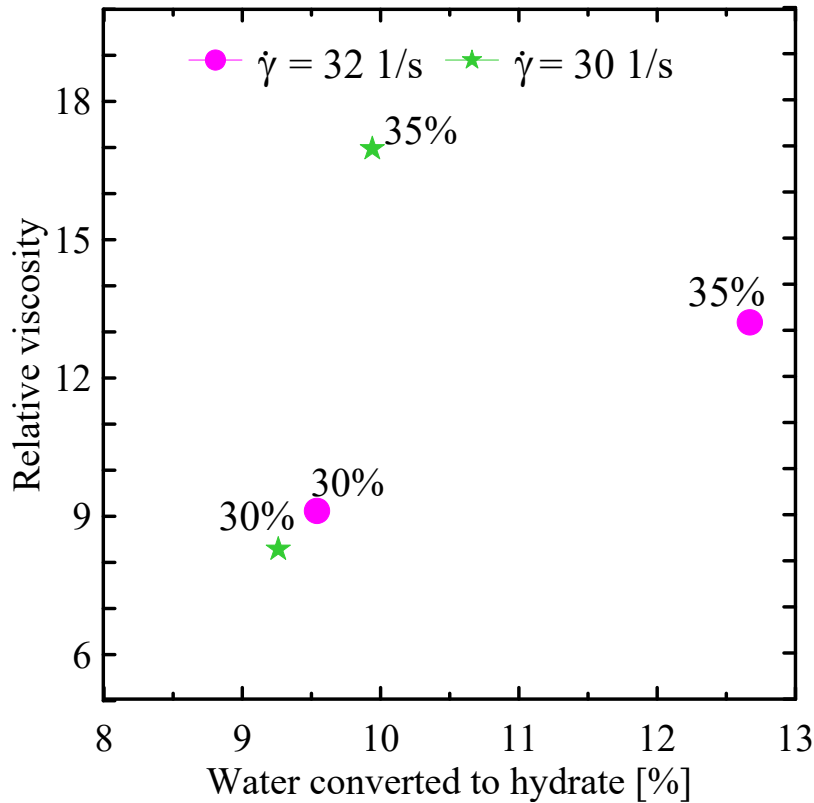


Figure 4.18: Relative viscosity *versus* water converted to hydrates for different shear rates. For each rate a variation of water cut was applied. Pressures of 31 bar.

converted to hydrates increases with increasing the water volume fraction and, therefore, a higher relative viscosity was measured. Secondly, for the same water cut, the relative viscosity decreased with the increment in the shear rate, due to higher breakage of hydrate agglomerates. For 30% of WVF, the relative viscosities were similar.

Charin et. al. [114], carried out a similar analysis but with mineral oil and kerosene. For both substances, it was observed that the higher the water volume fraction (WVF), the greater the relative viscosity achieved regardless of the shear rate.

4.5

Rheological behavior with shear rate ramp

This topic addresses an important point to complement the rheological study regarding the formation of hydrates. The shear rate ramp was applied in some tests that hydrates formation occurred. Tests with both geometries were selected that would allow a qualitative comparison. After the hydrates were formed and a steady state of viscosity was achieved, the shear rate ramp was

applied at a constant rate for a certain period of time. Then, this shear rate was decreased stepwise until a certain level, and then, programmed to return to its initial value. The influence of the shear history on the material rheology was addressed.

4.5.1 Concentric cylinders tests

All concentric cylinder tests were performed with 30% water volume fraction (WVF), a pressure of 31 bar, and a constant temperature of 4°C, which was the final temperature reached by all tests after forming the hydrate. Tests with initial shear rate of 700, 750, and 800 s⁻¹ were done. The subcooling was around 10.2°C. After more than 20 hours of testing and with the formation of the hydrate done, the shear rate ramp was applied. For the initial rate test of 800 s⁻¹, the shear rate was set to 700 s⁻¹ for 2 hours and then varied to 600, 500, and 400 s⁻¹ for the same period of time. After reaching the last rate of 400 s⁻¹, the ramp was changed again in the same rate and time interval until returning to the initial value of 800 s⁻¹ as can be seen in Fig. 4.19

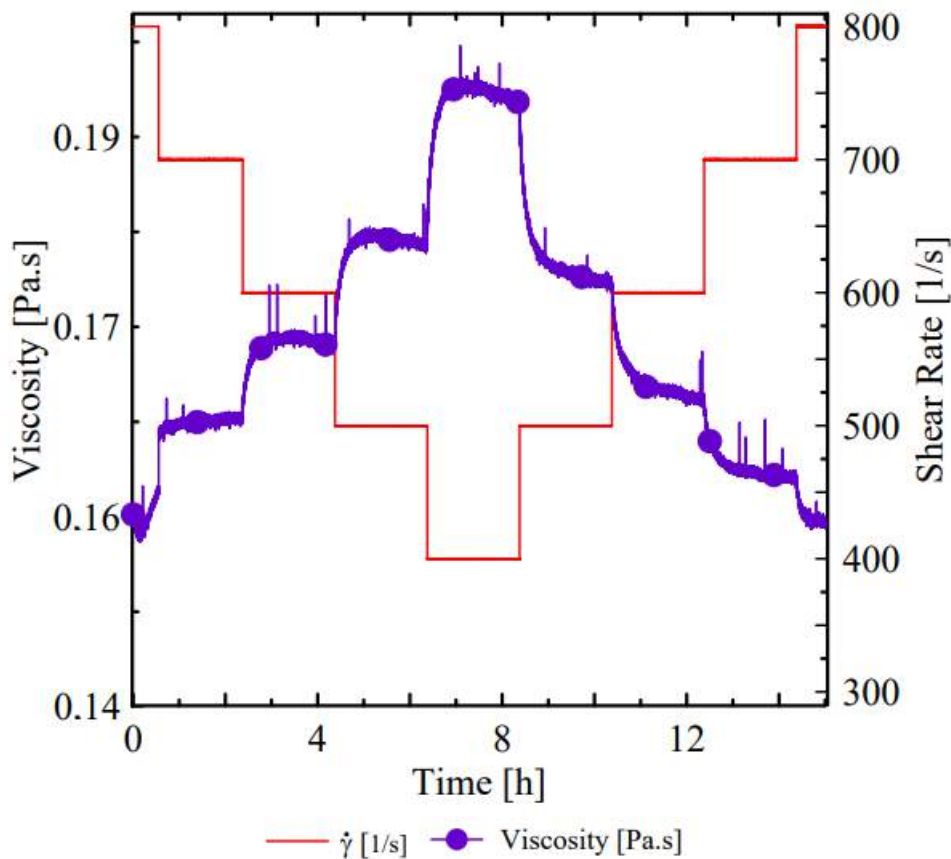


Figure 4.19: Shear rate ramp with initial rate of 800 s⁻¹ varying as a function of time.

It is possible to notice in Fig. 4.19 that the reduction on the shear rate, caused an increased on the viscosity. The reverse process also happened. As noted, the time of 2 hours was enough to achieve the steady state viscosity regime, both when the rate was decreased and when it was increased. At the end of the test it was possible to conclude that the viscosity returned to the same quantitative level that it was at the beginning of the test with $\dot{\gamma} = 800 \text{ s}^{-1}$. However, comparing at the same shear rate, a small reduction in viscosity was noted during the up ramp.

Exactly the same methodology was carried out for the tests that form hydrates at a shear rate of 750 and 700 s^{-1} . Fig. 4.20 shows the test with an initial value of 750 s^{-1} until a final shearing of 350 s^{-1} . The lower the shear rate, the higher the value of the viscosity measured. When the shear rate was increased, the viscosity decreased but the viscosity reached slower steady state values than that noticed in the first hours of testing. It was also possible to notice that the final viscosity presented a value below the initial one, that is, the slurry became less viscous after the applied ramps. This behavior is known as shear history-dependent, in which the material structure was irreversibly affected by the maximum applied shear rate [122]. This was already observed in waxy oils systems [167].

The test with an initial rate of 700 s^{-1} was performed until a final shear rate of 300 s^{-1} and also the rates were set for a period of 2 hours. Fig. 4.21 shows similarities with previous tests, where the final viscosity presented a lower value than the initial one until the same shear rate.

In general, all tests showed the same rheological behavior with the proposed time interval reaching a steady-state viscosity. All tests were conducted with a shear rate variation of 100 s^{-1} at the time the rate ramp occurred. It was noticed that, the shear rate ramps showed that hydrate slurries presented shear thinning behaviour as the viscosity decreases with the shear rate [122]. The viscosity variation did not change significantly, it was between 0.14 and 0.2 Pa.s, and all final viscosities showed lower values than the initial ones. Muhlstedt et. al., [122], explained this behavior by reporting that the shearing seems to degrade the solid structure, to disperse the hydrate particles and, consequently, to reduce the material viscosity. This result indicates that the structure of the hydrate slurry changes, in other words, the characteristic size of the hydrate agglomerates by the action of the imposed shear stress [152]. The highest viscosity reached during the shear rate ramp was during the test with a shear rate of 800 s^{-1} . But this was due to the fact that it was the test that also started with the highest viscosity. After that, it was visualized the test of 700 s^{-1} started and ended with the viscosity value greater than that

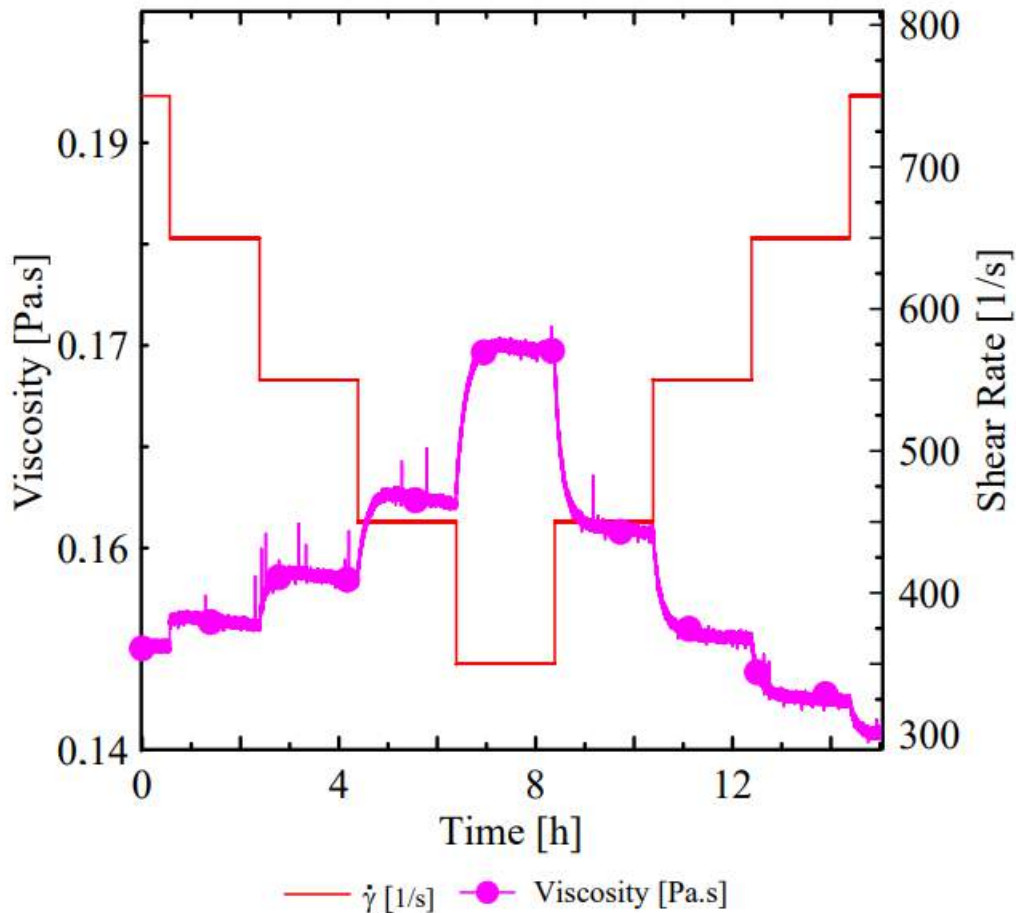


Figure 4.20: Shear rate ramp with initial rate of 750 s^{-1} varying as a function of time.

of 750 s^{-1} . In other words, the initial viscosity value also influences the final value along with the applied shear rate.

Webb et. al., [153], presented this result but using a mixing cell external to the high pressure cell. Muhlstedt et. al., [122] investigated the rheological behavior of hydrate slurries in a water-based drilling fluid formed with THF (tetrahydrofuran) as guest molecules and found similar results. They measured the stress during the step-down and step-up period and realized that never the same stress level will be obtained during for the same shear rate. The material structure can not be completely recovered during the step-down. In other words, the material breaks down the hydrate particles into smaller size aggregates.

After these analisys, the mathematical Power-law model was applied. The relationship between shear stress and shear rate (ploteed on log-log scale) for a shear-thinning fluid can often be approximated by a straight line over an experimental range of shear rate (or stress). For this part of the flow curve, an

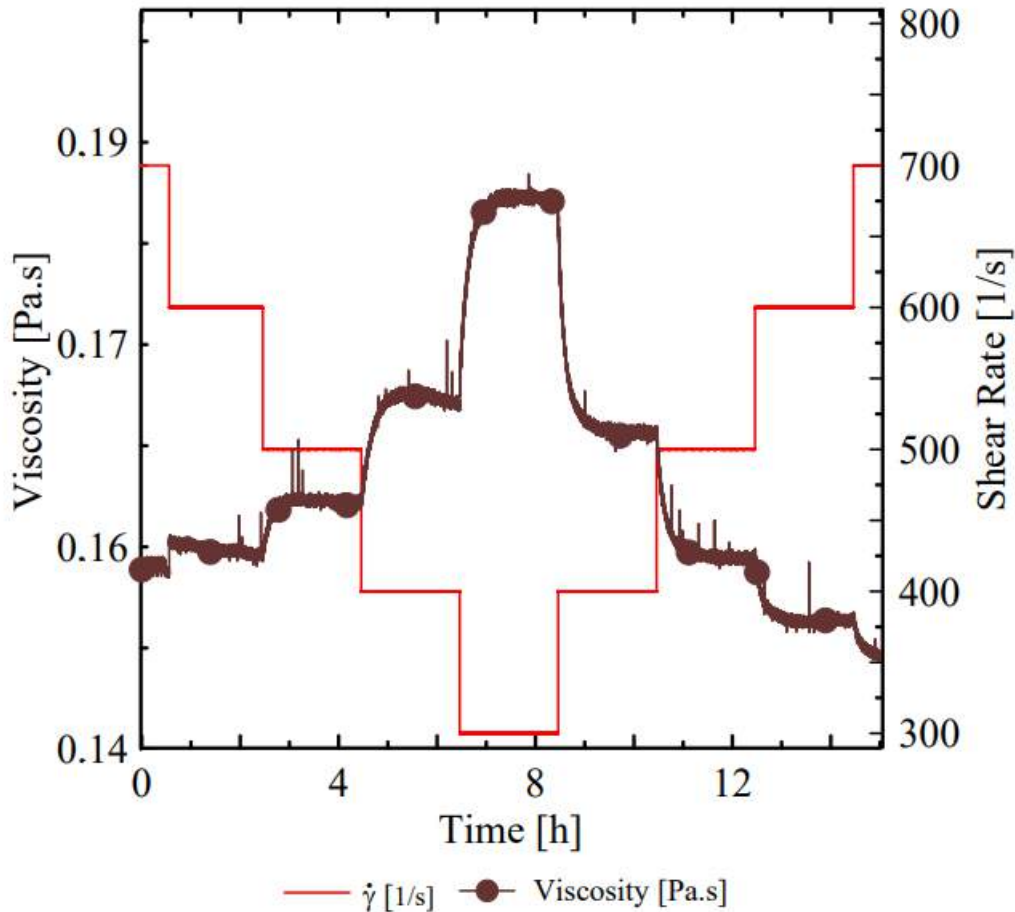


Figure 4.21: Shear rate ramp with initial rate of 700 s^{-1} varying as a function of time.

expression of the following form can be fitted by the Eq.4-1, where k is the consistency index and n is the flow index.

$$\eta = k(\dot{\gamma})^{n-1} \quad (4-1)$$

For $n < 1$, the fluid exhibits shear thinning behaviour, for $n = 1$, the fluid shows Newtonian behaviour, and for $n > 1$ the fluid shows shear thickening properties. For a shear thinning fluids, the index n ranges from 0 to 1, so that the smaller the value of n , the greater is the degree of shear thinning. It should be noted that the dimensions of the flow consistency coefficient, k , depend on the numerical value of n . On the other hand, the value of k can be viewed as the value of apparent viscosity at the shear rate of unity. Despite its limitations, this is the most widely used model in the literature dealing with process engineering applications. It is possible to notice in Fig. 4.22 , Fig. 4.23, and Fig. 4.24 the curve fittings obtained.

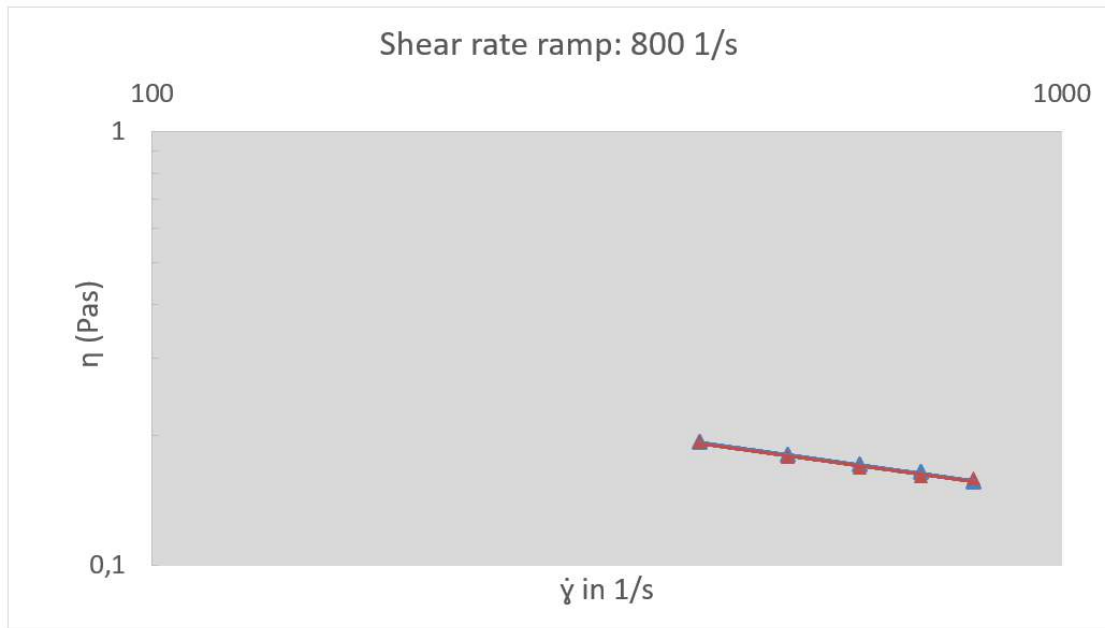


Figure 4.22: The experimental points (triangular) and the curves fitting of power-law. The blue and red color represents the shear rates decreases [A] and the shear rates increases [B] to 800 s^{-1} , respectively.

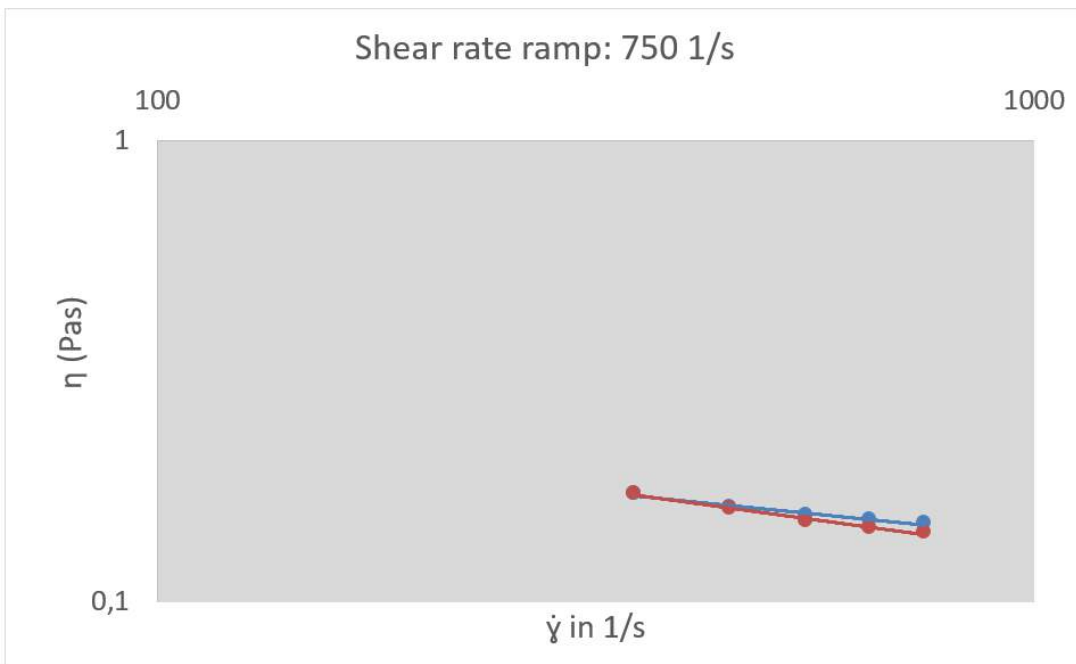


Figure 4.23: The experimental points (circular) and the curves fitting of power-law. The blue and red color represents the shear rates decreases [A] and the shear rates increases [B] to 750 s^{-1} , respectively.

Table 4.1 also shows the fitting results of the constancy index k and the power-law index n . Based on these results it was possible to conclude that the

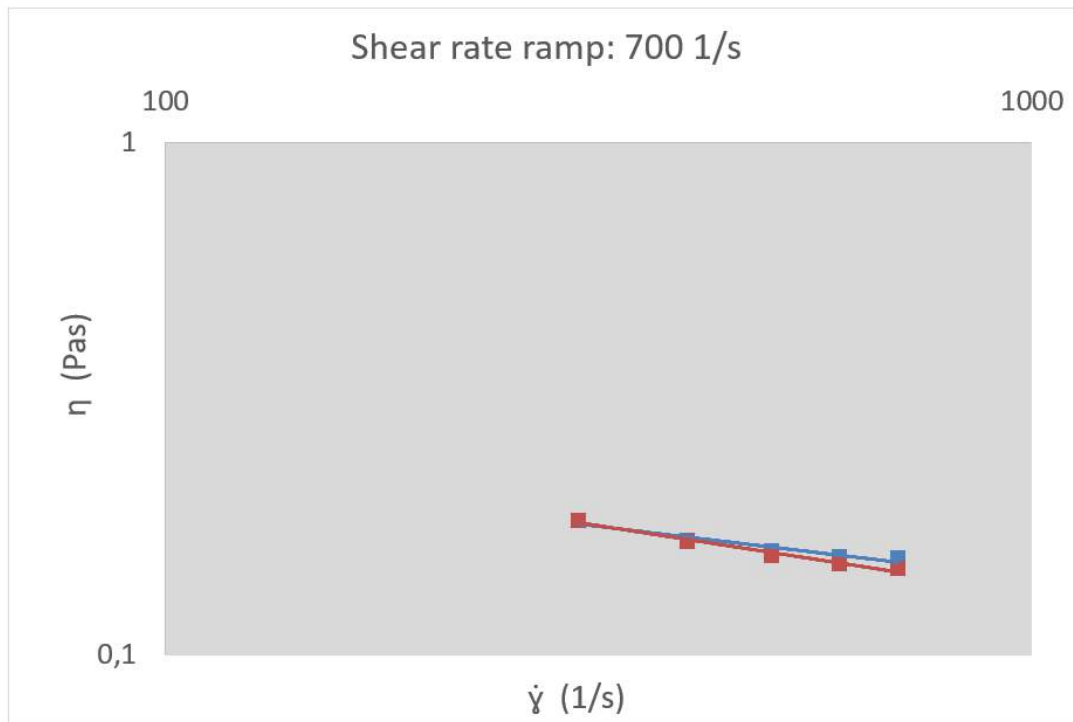


Figure 4.24: The experimental points (quadrates) and the curves fitting of power-law. The blue and red color represents the shear rates decreases [A] and the shear rates increases [B] to 700 s^{-1} , respectively.

Shear Rate (1/s)	Power-law [A]	Power-law [B]
800	$k = 1,1196 ; n = 0,706$	$k = 1,0872 ; n = 0,71$
750	$k = 0,52 ; n = 0,809$	$k = 0,783 ; n = 0,74$
700	$k = 0,5715 ; n = 0,798$	$k = 0,806 ; n = 0,739$

Table 4.1: Power law parameters obtained by curve fitting of experimental curves.

power-law was a good fit for the acquired data. The value of the exponent n in power-law [A] was lower (0.706) when compared to the values acquired on the others experiments, which indicates a more shear-thinning interface. The application of the model still reaffirms that all viscosities ended the tests with viscosities lower than the initial point, indicating again the shear history dependent.

4.5.2

Vane geometry tests

For the vane geometry, the same methodology applied for the concentric cylinder was used. The tests were performed with 30% water cut, pressure of 31 bar, and with a constant temperature of 4°C . The initial shear rates were equal to 30 and 32 s^{-1} .

The first test was performed with the shear rate of 30 s^{-1} until reach the steady state. Subsequently, the descent and ascent ramps were made with varying the shear rates of 25 and 20 s^{-1} . It was observed that the period of 2 hours set for each rate was insufficient for the viscosity to reach the steady state (see Fig. 4.25). Before 2 hours of testing it was possible to see in Fig. 4.25 that the viscosity reached a stable level but then it increased sharply when was still subjected to the same shear rate. Between 2 and 4 hours of testing, the viscosity only increased and did not stabilized. Because of this, it was decided to increase the time period between ramps to 4 hours to see if the situation would change.

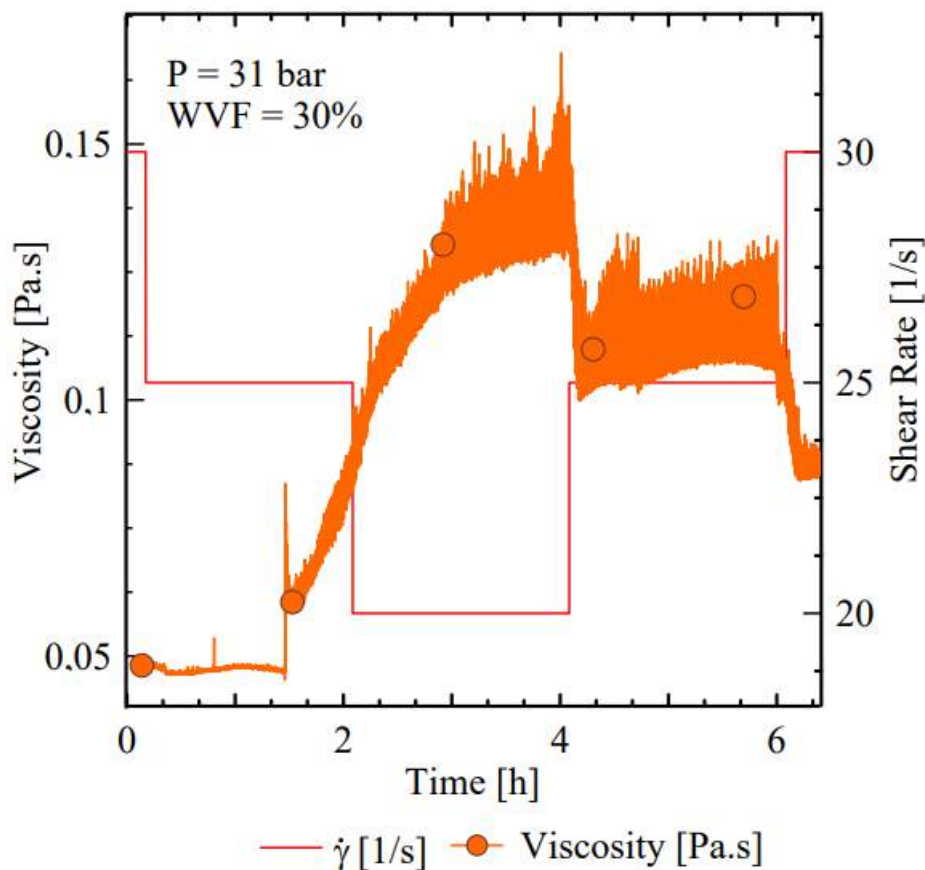


Figure 4.25: Shear rate ramp with initial rate of 30 s^{-1} and with 2 hours of a period time between rates.

Another test forming hydrates at a shear rate of 30 s^{-1} was performed, and the shear rate ramps were conducted at 25 and 20 s^{-1} . The result can be seen in Fig. 4.26. Between 2 h and 6 h of test it was possible to notice that the viscosity remained stable, but presented a slight increase between 5 h and 6 h. When the shear rate was changed to 20 s^{-1} it was noted that the viscosity increased and remained stable. When the shear rate was increased

again, it was seen that the viscosity remained stable but at slightly higher value, regarding those obtained during the decreasing ramp. The behaviour showed more oscillations in viscosity when compared to that observed with concentric cylinders. Despite this difference, it was observed a similar behavior between both geometries when the applied shear rate was increased, leading to lower viscosities. So, a material also with shear thinning behavior. That pattern has been also reported by Muhlstedt et. al., [122]. Also, it can be noticed that the viscosity variation window was small. The difference observed for concentric cylinders was that the viscosity at the end of the test was higher than at the beginning of the test. This was due to the fact that the vane geometry provides the breaking of the formed structure and at the same time the formation of more hydrate.

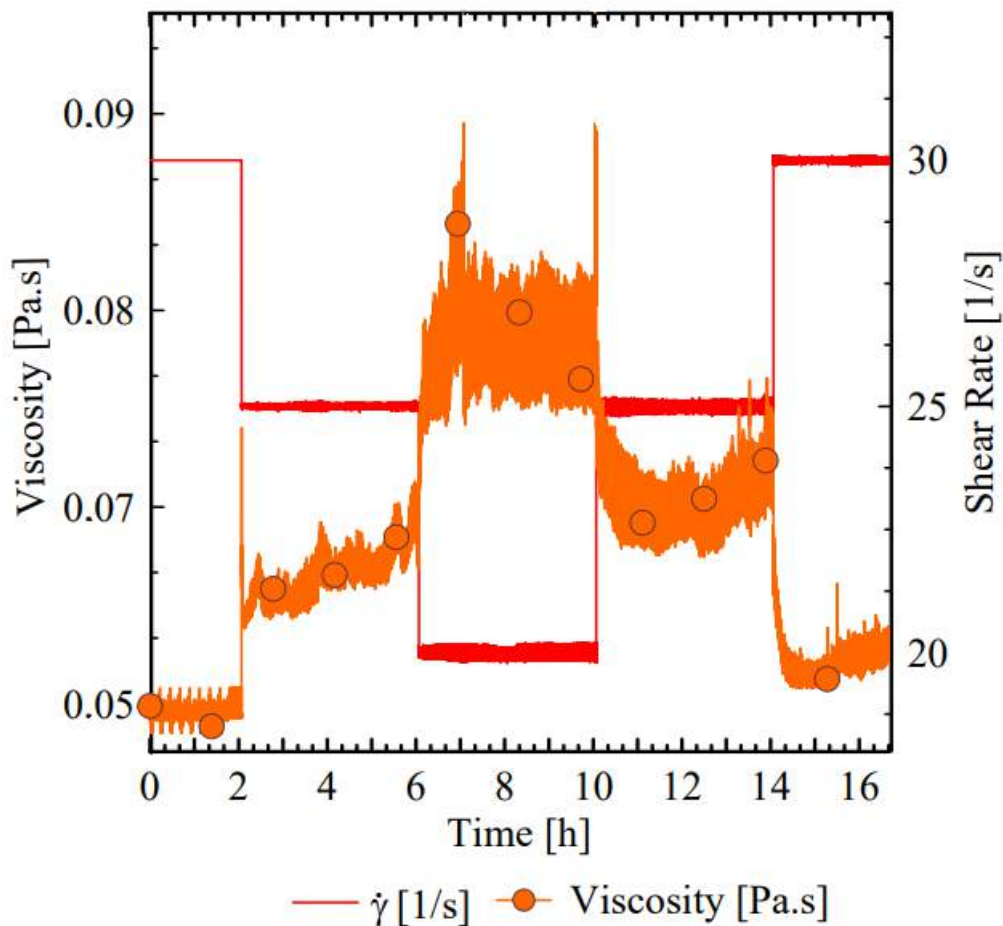


Figure 4.26: Shear rate ramp with initial rate of 30 s^{-1} and with 4 hours of a period time between rates.

To complement the understanding, another test with a shear rate hydrate formation of 32 s^{-1} was performed. A different behavior was noticed regarding the others experiments presented above. As seen in Fig. 4.27, the shear rates of 27 and 22 s^{-1} were applied during the tests ramp. The highest viscosity value

detected was around 0.65 Pa.s, while for tests with $\dot{\gamma} = 30 \text{ s}^{-1}$ the viscosity did not exceed 0.1 Pa.s. In Fig. 4.27 it was possible to see that the viscosity presented almost none variations over time even when the shear rates changed. This behavior differed from the others previously presented that showed some type of variation with the shear rates. Kakitani et. al., [168], also studied the shear rate ramp but with a modified vane geometry, that is, with the vane having a small opening to prevent particles from accumulating in a dead zone. It was observed that the slurry of the hydrate was unstable and noisy with the changing of the rotational speed as observed in Fig. 4.26 and Fig. 4.27. The large fluctuations in viscosity may be due to the non-uniform size of the hydrate clusters due to constant aggregation and breakdown, provided by the characteristics of the vane geometry [168]. This justifies the final viscosity of Fig. 4.26 and Fig. 4.27 have been larger than the initial, as well as, the fact that the vane of this previous study presented dead zones where, due to having accumulated hydrate particles during the breaks, increasing the value of the final viscosity.

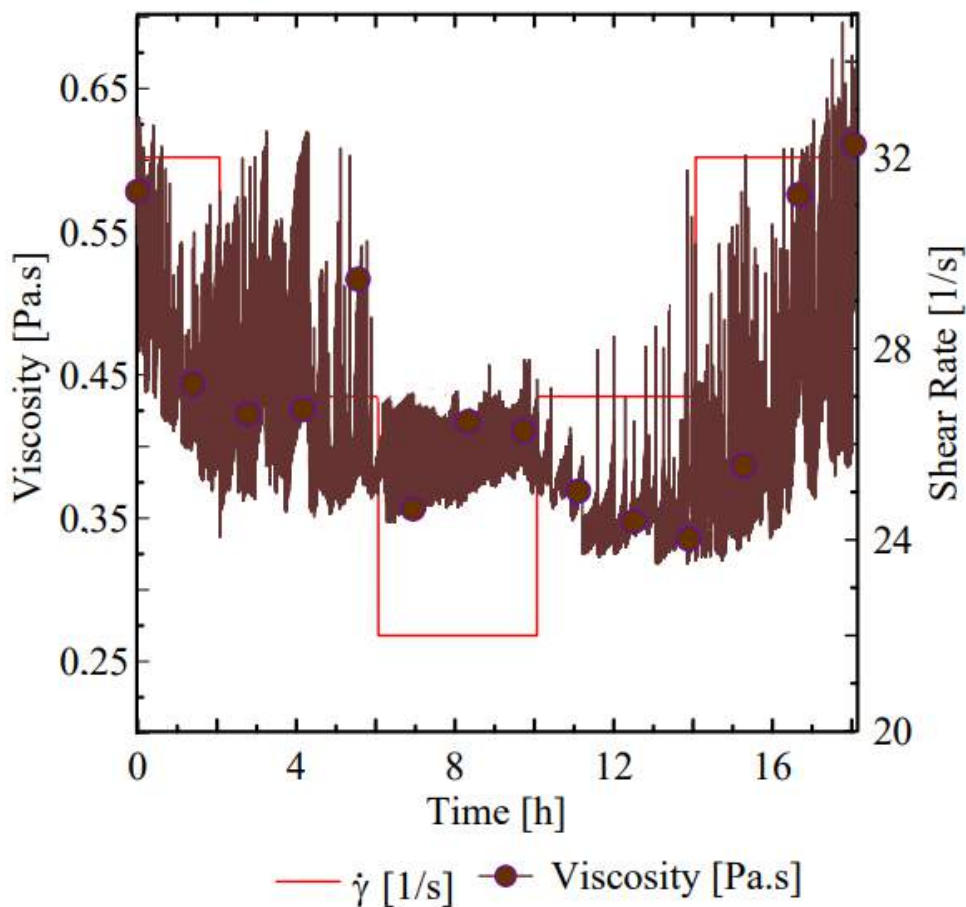


Figure 4.27: Shear rate ramp with initial rate of 32 s^{-1} and with 4 hours of a period time between rates.

In general, all tests presented a restricted viscosity variation window, that is, after the formation of hydrates and the consumption of gas, the applied shear rate no longer significantly interferes with viscosity. The tests performed with concentric cylinder geometry also showed small variation on the viscosity during the ramp tests between 0.14 and 0.2 Pa.s. As noted, the tests conducted with vane geometry showed different results. The highest shear rate of 32 s^{-1} did not show quantitatively measurable variations on viscosity, opposite to what was observed for the shear rate of 30 s^{-1} .

Ding et. al. [159], studied similar tests with natural gas and found similar results as the velocity increased from 0.39 to 1.23 m/s, the slurry viscosity decreased from 18 to 13.3 mPa.s, which demonstrated that the hydrate slurry had a shear thinning behavior. The experiments were conducted in water-in-model oil emulsion systems using a high-pressure flow loop. These results were very similar to those found for concentric cylinders and for vane geometry with a rate of 30 s^{-1} [16, 17, 164].

5

Final remarks

In the present work a rheological study of ethane gas hydrates formed from water-in-model oil emulsions was performed. The influence of subcooling, shear rate, and water volume fraction was investigated for two different rheometric geometries, concentric cylinders and the vane rotor. The results obtained were presented through viscosity and pressure curves with time. The amount of water converted to hydrates was also determined and these data were also correlated with the viscosity. To complement the rheological study of hydrate formation, tests with shear rate ramps variation after hydrate formation were performed. The ramp tests were conducted with the same pressure and water cut, only varying the shear rates and geometries. For both geometries, similar qualitative results were observed and are described below:

- For each assessed parameter, there was a hydrate formation window. Below this window, hydrates did not form because there was not enough hydrate driving forces, and above this window, the formation was so severe that the torque required at the rheometer surpasses the equipment limit and the test stops.
- The repeatability tests presented show the reliable character of the hydrate tests analyzed. However, it was observed that the induction time could vary. The repetitive behavior was also observed for tests that did not form hydrates or that showed peak formation. It is important to emphasize that the tests with concentric cylinders presented more repeatability of results.
- The subcooling condition affects the induction period. Higher subcoolings make hydrates form faster for both geometries. It is also worth noting that for the tests conducted with the vane rotor, higher steady-state viscosities were reached when larger subcooling were applied, but the amount of water converted to hydrates was essentially the same (as shown in Fig. 4.12). Therefore, such a difference in viscosity was likely caused by the agglomeration among hydrate particles.
- The higher the shear rate, the shorter the induction time. The viscosity peak reached by the tests at the moment of hydrate formation was

practically the same even when different shear rates were applied. This behavior was observed in both geometries studied. The vane geometry presented a very restricted shear rate variation window. Different results were observed for the shear rate tests of 35 and 32 s⁻¹. That is, only with a variation of $\dot{\gamma} = 3 \text{ s}^{-1}$.

- Both geometries presented similar results regarding the water volume fraction influence on hydrates formation. The higher the water volume fraction, the higher the viscosity spike reached during the hydrate growth, and when it reached the steady state regime. However, the geometries showed differences in the amount of water converted to hydrate. For the vane geometry, the increment in the water volume fraction, produced an increment in the amount of water converted to hydrates (see Figure 4.16).
- The analysis of the relative viscosities showed some compatibility between concentric cylinders and vane geometry. For the concentric cylinder system, regardless of the applied shear rate, the relative viscosity increased with increasing the water volume fraction. The same behavior was verified for the vane geometry, where the highest water volume fraction presented higher relative viscosity. This happened because the viscosity level was similar for the two shear rates assessed (see Figure 4.8). Both geometries showed higher relative viscosities with their lower shear rates and higher water converted to hydrates for the highest shear rates. This was due to a greater agglomeration between hydrate particles.
- For the shear ramp tests performed after forming hydrate, the results were similar for both geometries exhibiting shear thinning behavior. Viscosity was reduced with increasing the shear rate. However, the viscosity results obtained with the concentric cylinder geometry were always lower during the ascendant ramp than those obtained at the descendent ramp when analyzed at the same shear rate. The vane geometry presented greater difficulties to reach steady state for each step of shear rate. This was probably due to the different speeds that can occur with the use of this geometry, and due to breakdown of hydrate particles.
- Nair et. al., [18] and Pandey et. al., [16], mention in their studies that they modified the geometry of concentric cylinders because they believed that the conventional geometry was poor in mixing ability. However, when analyzing the results presented above, it was possible to notice that the conventional geometry of concentric cylinders presented satisfactory results and capacity to form hydrates with different parameters being analyzed and modified.

Finally, the results obtained show that both geometries can be used to study the kinetics of hydrates formation and to evaluate the hydrate slurry rheological properties. If the smooth concentric cylinder geometry is employed, high shear rates should be used to avoid the apparent wall slippage. Conversely, if the vane geometry is used, caution should be taken in the highest shear rates in order to avoid secondary flows.

During the performance of all these tests some difficulties were encountered. In addition to the limitations with the pressure applied in the tests, there is still a difficulty in making a study of the rheology with the formed hydrate structure, which appears as a non-homogeneous and porous compound, therefore non-uniform. This peculiarity brings great challenges in the analysis of parameters such as viscosity, yield strength, plasticity and others.

Although the results obtained bring important insight for understanding hydrate formation and its rheological behavior. Several factors were considered, showing that the knowledge of the parameters was essential for the control and mitigation of processes that could eventually be harmed with the presence of gas hydrates.

6

Future work

The study of gas hydrate formation and its dissociation has been studied for many years. Notwithstanding, a study will never become absolute on the subject. The complexity of hydrates opens several opportunities for research, study, analysis, and understanding for the present and future generations with new challenges presented. Below it is possible to see a list with suggestions with main directions that can be followed:

- Carry out the same experimental procedures shown here, but with the use of other gases such as: methane, nitrogen, and natural gas;
- Perform a rheological study, similar as was showed here, using a non-emulsify system - without surfactant;
- Use other types of measurement geometries to evaluate the hydrate slurry. Thus, it is possible to make new qualitative and quantitative comparisons of the behavior of the hydrate;
- Perform a Scanning Electron Microscope (SEM) analysis on the hydrate structure formed after the tests. Thus, it will be possible to correlate the hydrate morphology with its rheological behavior;
- Carry out a temperature ramp to evaluate the rheological behavior of the hydrate slurry;
- Calculate the yield stress found in the results to verify if it would be possible to maintain the flow with the formed hydrate structure;
- Carry out the experiments by pausing the shear to simulate the stoppage of oil and gas production. With this it will be possible to verify what happens to the already formed hydrate structure or if more hydrate would form under these static conditions;
- Make the same amount of emulsion to apply to different geometries;
- Raise the main difficulties of obtaining rheological data from the study of hydrates and what are the possible improvements.

7

Bibliography

- 1 JOZIAN, S.; VAFAJOO, L. Mathematical modeling of the gas hydrate formation in a 90 elbow utilizing cfd technique. **Chemical Engineering Transactions**, v. 70, p. 2167–2172, 2018.
- 2 IZQUIERDO-RUIZ, F. et al. Effects of the CO₂ Guest Molecule on the sl Clathrate Hydrate Structure. **Materials**, v. 9, n. 9, p. 777, 2016.
- 3 RUPPEL, C. D.; KESSLER, J. D. The interaction of climate change and methane hydrates. **Reviews of Geophysics**, Wiley Online Library, v. 55, n. 1, p. 126–168, 2017.
- 4 KIRCHNER, M. T. et al. Gas hydrate single-crystal structure analyses. **Journal of the American Chemical Society**, ACS Publications, v. 126, n. 30, p. 9407–9412, 2004.
- 5 QIN, Y. et al. High pressure rheological measurements of gas hydrate-in-oil slurries. **Journal of Non-Newtonian Fluid Mechanics**, Elsevier, v. 248, p. 40–49, 2017.
- 6 TAYLOR, C. J. et al. Micromechanical adhesion force measurements between tetrahydrofuran hydrate particles. **Journal of colloid and interface science**, Elsevier, v. 306, n. 2, p. 255–261, 2007.
- 7 BASSANI, C. L. et al. Predicting gas hydrate formation during three-phase gas-(water-in-oil) flow. In: ONEPETRO. **BHR 19th International Conference on Multiphase Production Technology**. [S.l.], 2019.
- 8 BASSANI, C. L. et al. A multiscale approach for gas hydrates considering structure, agglomeration, and transportability under multiphase flow conditions: I. phenomenological model. **Industrial & Engineering Chemistry Research**, ACS Publications, v. 58, n. 31, p. 14446–14461, 2019.
- 9 KE, W.; SVARTAAS, T. M.; CHEN, D. A review of gas hydrate nucleation theories and growth models. **Journal of Natural Gas Science and Engineering**, Elsevier, v. 61, p. 169–196, 2019.
- 10 WARRIER, P. et al. Overview: Nucleation of clathrate hydrates. **The Journal of chemical physics**, AIP Publishing LLC, v. 145, n. 21, p. 211705, 2016.
- 11 WANG, Y.; FAN, S.; LANG, X. Reviews of gas hydrate inhibitors in gas-dominant pipelines and application of kinetic hydrate inhibitors in China. **Chinese Journal of Chemical Engineering**, Elsevier, v. 27, n. 9, p. 2118–2132, 2019.

- 12 WILLENBACHER, N.; GEORGIEVA, K. Rheology of disperse systems. **Product design and engineering: Formulation of gels and pastes**, Wiley-VCH Verlag GmbH & Co. KGaA Weinheim, Germany, v. 44, 2013.
- 13 GALINDO, M. S. V. **Determinação da Viscosidade de Solos**. Tese (Doutorado) — PUC-Rio, 2013.
- 14 POHORECKI, R. et al. **Chemical Engineering and Chemical Process Technology-Volume VII: Rheology-Part II**. [S.I.]: EOLSS Publications, 2010.
- 15 BOGER, D. V. Rheology and the resource industries. **Chemical Engineering Science**, Elsevier, v. 64, n. 22, p. 4525–4536, 2009.
- 16 PANDEY, G.; LINGA, P.; SANGWAI, J. S. High pressure rheology of gas hydrate formed from multiphase systems using modified couette rheometer. **Review of scientific instruments**, AIP Publishing LLC, v. 88, n. 2, p. 025102, 2017.
- 17 WEBB, E. B.; KOH, C. A.; LIBERATORE, M. W. High pressure rheology of hydrate slurries formed from water-in-mineral oil emulsions. **Industrial & Engineering Chemistry Research**, ACS Publications, v. 53, n. 17, p. 6998–7007, 2014.
- 18 NAIR, V. C. et al. High-pressure rheology of methane hydrate sediment slurry using a modified couette geometry. **Industrial & Engineering Chemistry Research**, ACS Publications, v. 59, n. 9, p. 4079–4092, 2019.
- 19 NAZARI, B.; MOGHADDAM, R. H.; BOUSFIELD, D. A three dimensional model of a vane rheometer. **International journal of heat and fluid flow**, Elsevier, v. 42, p. 289–295, 2013.
- 20 RABIA, A. et al. Optimization of the vane geometry. **Rheologica Acta**, Springer, v. 53, n. 4, p. 357–371, 2014.
- 21 MAITI, M. et al. Inhibition effect of synthesized ionic liquids on hydrate formation: A kinetic and thermodynamic study. **Energy & Fuels**, ACS Publications, 2022.
- 22 KALE, S. N.; DEORE, S. L. Emulsion micro emulsion and nano emulsion: a review. **Systematic Reviews in Pharmacy**, Phcog. net, v. 8, n. 1, p. 39, 2017.
- 23 MYERS, D. **Surfactant science and technology**. [S.I.]: John Wiley & Sons, 2020.
- 24 DELGADO-LINARES, J. G. et al. Model water-in-oil emulsions for gas hydrate studies in oil continuous systems. **Energy & Fuels**, ACS Publications, v. 27, n. 8, p. 4564–4573, 2013.
- 25 FUJII, S. et al. Hydroxyapatite nanoparticles as particulate emulsifier: fabrication of hydroxyapatite-coated biodegradable microspheres. **Langmuir**, ACS Publications, v. 25, n. 17, p. 9759–9766, 2009.

- 26 SANDOVAL, G. A. B. **RHEOLOGICAL AND COMPOSITION ANALYSES OF CO₂ GAS HYDRATES**. Tese (Doutorado) — Universidade Federal do Rio de Janeiro, 2019.
- 27 FILHO, V. F. **Gestão de operações e logística na produção de petróleo**. [S.l.]: Elsevier Brasil, 2015.
- 28 SLOAN, E. D. **Natural gas hydrates in flow assurance**. [S.l.]: Gulf Professional Publishing, 2010.
- 29 JR, E. D. S.; KOH, C. A. **Clathrate hydrates of natural gases**. [S.l.]: CRC press, 2007.
- 30 COTO, B. et al. Experimental study of the effect of inhibitors in wax precipitation by different techniques. **Energy Science & Engineering**, Wiley Online Library, v. 2, n. 4, p. 196–203, 2014.
- 31 GOUAL, L. Petroleum asphaltenes. **Crude oil emulsions-Composition stability and characterization**, InTech, p. 28–43, 2012.
- 32 MOHAMMED, I. et al. Asphaltene precipitation and deposition: A critical review. **Journal of Petroleum Science and Engineering**, Elsevier, v. 197, p. 107956, 2021.
- 33 JR, E. D. S. Fundamental principles and applications of natural gas hydrates. **Nature**, Nature Publishing Group UK London, v. 426, n. 6964, p. 353–359, 2003.
- 34 KVENVOLDEN, K. Methane hydrates resources in the near future? **JNOC-TRC of Japan, October 20-22.(1998)**, 1998.
- 35 MILKOV, A.; SASSEN, R. Resource and economic potential of gas hydrates in the northwestern gulf of mexico. In: **Proc. 4th Int. Conf. Gas Hydrates**. [S.l.: s.n.], 2002. p. 111–114.
- 36 KHOKHAR, A.; GUDMUNDSSON, J.; SLOAN, E. Gas storage in structure h hydrates. **Fluid Phase Equilibria**, Elsevier, v. 150, p. 383–392, 1998.
- 37 BOTH, A. K. et al. Gas hydrates in confined space of nanoporous materials: new frontier in gas storage technology. **Nanoscale**, Royal Society of Chemistry, v. 13, n. 16, p. 7447–7470, 2021.
- 38 RUPPEL, C. D. Methane hydrates and contemporary climate change. **Nature Education Knowledge**, v. 2, n. 12, p. 12, 2011.
- 39 HAMMERSCHMIDT, E. G. Formation of gas hydrates in natural gas transmission lines. **Industrial Engineering Chemistry**, ACS Publications, v. 26, n. 8, p. 851–855, 1934.
- 40 DAVIDSON, D. et al. Some structural studies of clathrate hydrates. **Le Journal de Physique Colloques**, EDP Sciences, v. 48, n. C1, p. C1–537, 1987.
- 41 SLOAN, E. D. Clathrate hydrates of natural gases, 2nd ed. **Energy fuels**, ACS Publications, v. 12, n. 2, p. 191–196, 1998.

- 42 LU, H. et al. Complex gas hydrate from the cascadia margin. **Nature**, Nature Publishing Group, v. 445, n. 7125, p. 303–306, 2007.
- 43 HIRAI, H. et al. Structural changes in gas hydrates and existence of a filled ice structure of methane hydrate above 40 gpa. **Journal of Physics and Chemistry of Solids**, Elsevier, v. 65, n. 8-9, p. 1555–1559, 2004.
- 44 KOH, C. A. et al. Fundamentals and applications of gas hydrates. **Annu. Rev. Chem. Biomol. Eng**, v. 2, n. 1, p. 237–257, 2011.
- 45 PASO, K. et al. Characterization of the formation, flowability, and resolution of brazilian crude oil emulsions. **Energy & Fuels**, ACS Publications, v. 23, n. 1, p. 471–480, 2009.
- 46 PAEZ, J. Problems in hydrates: mechanisms and elimination methods. In: ONEPETRO. **SPE Production and Operations Symposium**. [S.l.], 2001.
- 47 TURNER, D. J.; MILLER, K. T.; SLOAN, E. D. Methane hydrate formation and an inward growing shell model in water-in-oil dispersions. **Chemical Engineering Science**, Elsevier, v. 64, n. 18, p. 3996–4004, 2009.
- 48 SHI, B.-H. et al. An inward and outward natural gas hydrates growth shell model considering intrinsic kinetics, mass and heat transfer. **Chemical engineering journal**, Elsevier, v. 171, n. 3, p. 1308–1316, 2011.
- 49 LORENZO, M. D. et al. Modelling hydrate deposition and sloughing in gas-dominant pipelines. **The Journal of Chemical Thermodynamics**, Elsevier, v. 117, p. 81–90, 2018.
- 50 ZERPA, L. E. et al. Overview of csmhyk: A transient hydrate formation model. **Journal of Petroleum Science and Engineering**, Elsevier, v. 98, p. 122–129, 2012.
- 51 YAMASHIRO, B. D.; TOMAC, I. Particle clustering dynamics in dense-phase particle-fluid slurries. **Computers and Geotechnics**, Elsevier, v. 132, p. 104038, 2021.
- 52 KASHCHIEV, D.; FIROOZABADI, A. Nucleation of gas hydrates. **Journal of crystal growth**, Elsevier, v. 243, n. 3-4, p. 476–489, 2002.
- 53 LI, Z. et al. Advances in molecular dynamics simulation on heterogeneous nucleation of gas hydrate. **Functional Materials Letters**, World Scientific, v. 14, n. 07, p. 2130010, 2021.
- 54 BALLARD, A.; JR, E. S. The next generation of hydrate prediction: Part iii. gibbs energy minimization formalism. **Fluid phase equilibria**, Elsevier, v. 218, n. 1, p. 15–31, 2004.
- 55 SLOAN, D.; KOH, C. Clathrate hydrates of natural gases third edition. **Earth Sciences, Engineering Technology**, MARCEL DEKKER AG, v. 119, 2008.
- 56 LIANG, S.; KUSALIK, P. G. Nucleation of gas hydrates within constant energy systems. **The Journal of Physical Chemistry B**, ACS Publications, v. 117, n. 5, p. 1403–1410, 2013.

- 57 HENLEY, H.; THOMAS, E.; LUCIA, A. Density and phase equilibrium for ice and structure i hydrates using the gibbs–helmholtz constrained equation of state. **Chemical Engineering Research and Design**, Elsevier, v. 92, n. 12, p. 2977–2991, 2014.
- 58 BALLARD, A.; JR, E. S. The next generation of hydrate prediction: An overview. **Journal of Supramolecular Chemistry**, Elsevier, v. 2, n. 4-5, p. 385–392, 2002.
- 59 MULLIN, J. W. **Crystallization**. [S.l.]: Elsevier, 2001.
- 60 ATKINS, P.; PAULA, J. D. **Elements of physical chemistry**. [S.l.]: Oxford University Press, USA, 2013.
- 61 LUBAS´, J.; DARŁAK, B. Metastability of natural gas hydrates in the presence of n 2 and h 2 s. **J. Energy Resour. Technol.**, v. 126, n. 2, p. 125–132, 2004.
- 62 SUN, R. et al. Metastable state of gas hydrate during decomposition: A novel phenomenon. **Chinese Journal of Chemical Engineering**, Elsevier, v. 28, n. 4, p. 949–954, 2020.
- 63 BAEK, S. et al. Hydrate seeding effect on the metastability of ch4 hydrate. **Korean Journal of Chemical Engineering**, Springer, v. 37, n. 2, p. 341–349, 2020.
- 64 HEIDARYAN, E. et al. A new high performance gas hydrate inhibitor. **Journal of natural gas chemistry**, Elsevier, v. 19, n. 3, p. 323–326, 2010.
- 65 WANG, X. et al. Fatty acid-asphaltene interactions at oil/water interface. **Colloids and Surfaces A: Physicochemical and Engineering Aspects**, v. 513, p. 168–177, 2017.
- 66 WANG, B. et al. Evaluation of thermal stimulation on gas production from depressurized methane hydrate deposits. **Applied Energy**, Elsevier, v. 227, p. 710–718, 2018.
- 67 KIM, H. et al. Economic evaluation of meg injection and regeneration process for oil fpo. **Journal of Petroleum Science and Engineering**, Elsevier, v. 164, p. 417–426, 2018.
- 68 ZHANG, L. et al. Hydrate risks and prevention solutions for a high pressure gas field offshore in south china sea. **International Journal of Oil, Gas and Coal Technology**, Inderscience Publishers Ltd, v. 6, n. 6, p. 613–623, 2013.
- 69 LI, K. et al. Dissociation mechanism of propane hydrate with methanol additive: A molecular dynamics simulation. **Computational and Theoretical Chemistry**, Elsevier, v. 1123, p. 79–86, 2018.
- 70 SONG, G. et al. Experimental study of hydrate dissociation in oil-dominated systems using a high-pressure visual cell. **Journal of Natural Gas Science and Engineering**, Elsevier, v. 45, p. 26–37, 2017.

- 71 AMINNAJI, M. et al. Gas hydrate blockage removal using chemical injection in vertical pipes. **Journal of Natural Gas Science and Engineering**, Elsevier, v. 40, p. 17–23, 2017.
- 72 AMINNAJI, M. et al. Effect of injected chemical density on hydrate blockage removal in vertical pipes: Use of meg/meoh mixture to remove hydrate blockage. **Journal of Natural Gas Science and Engineering**, Elsevier, v. 45, p. 840–847, 2017.
- 73 HU, Y.; LEE, B. R.; SUM, A. K. Phase equilibrium data of methane hydrates in mixed brine solutions. **Journal of Natural Gas Science and Engineering**, Elsevier, v. 46, p. 750–755, 2017.
- 74 LEDERHOS, J. et al. Effective kinetic inhibitors for natural gas hydrates. **Chemical Engineering Science**, Elsevier, v. 51, n. 8, p. 1221–1229, 1996.
- 75 YEH, Y.; FEENEY, R. E. Antifreeze proteins: structures and mechanisms of function. **Chemical reviews**, ACS Publications, v. 96, n. 2, p. 601–618, 1996.
- 76 KLOMP, U.; CLERQ, M. L.; KINS, S. V. The first use of hydrate anti-agglomerant for a fresh water producing gas/condensate field. In: **Petromin Deepwater Conference, Kuala Lumpur**. [S.l.: s.n.], 2004.
- 77 CLARK, L. W.; FROSTMAN, L. M.; ANDERSON, J. Low dosage hydrate inhibitors (ldhi): Advances in flow assurance technology for offshore gas production systems. In: ONEPETRO. **International petroleum technology conference**. [S.l.], 2005.
- 78 CLARK, L. W.; AANDERSON, J. Low dosage hydrate inhibitors (ldhi): Advances in flow assurance technology for gas production systems. In: ONEPETRO. **International Petroleum Technology Conference**. [S.l.], 2007.
- 79 FROSTMAN, L. M.; CROSBY, D. L. Flow assurance using ldhis: Deepwater experience, ultradeep challenges. In: **Deep Offshore Technology Conference, Marseille, Nov**. [S.l.: s.n.], 2003. p. 19–21.
- 80 LAMBOURNE, R.; STRIVENS, T. A. **Paint and surface coatings: theory and practice**. [S.l.]: Elsevier, 1999.
- 81 DOBRASZCZYK, B.; MORGENSTERN, M. Rheology and the breadmaking process. **Journal of cereal Science**, Elsevier, v. 38, n. 3, p. 229–245, 2003.
- 82 ASTARITA, G. **Rheology: Volume 2: Fluids**. [S.l.]: Springer Science & Business Media, 2013.
- 83 TANNER, R. I. **Engineering rheology**. [S.l.]: OUP Oxford, 2000. v. 52.
- 84 MALKIN, A.; MALKIN, A. Y. **Rheology fundamentals**. [S.l.]: ChemTec publishing, 1994.
- 85 RUEDA, M. M. et al. Rheology and applications of highly filled polymers: A review of current understanding. **Progress in Polymer Science**, Elsevier, v. 66, p. 22–53, 2017.

- 86 VLACHOPOULOS, J.; POLYCHRONOPOULOS, N. D. **Understanding rheology and technology of polymer extrusion**. [S.l.]: Polydynamics Inc, 2019.
- 87 CHHABRA, R. P.; COMITI, J.; MACHAČ, I. Flow of non-newtonian fluids in fixed and fluidised beds. **Chemical Engineering Science**, Elsevier, v. 56, n. 1, p. 1–27, 2001.
- 88 AGWU, O. E. et al. A critical review of drilling mud rheological models. **Journal of petroleum science and engineering**, Elsevier, v. 203, p. 108659, 2021.
- 89 SOCHI, T. Non-newtonian flow in porous media. **Polymer**, Elsevier, v. 51, n. 22, p. 5007–5023, 2010.
- 90 COLLYER, A. Time dependent fluids. **Physics Education**, IOP Publishing, v. 9, n. 1, p. 38, 1974.
- 91 FALL, A. et al. Shear thickening of cornstarch suspensions as a reentrant jamming transition. **Physical review letters**, APS, v. 100, n. 1, p. 018301, 2008.
- 92 LOOTENS, D. et al. Dilatant flow of concentrated suspensions of rough particles. **Physical review letters**, APS, v. 95, n. 26, p. 268302, 2005.
- 93 WAGNER, N. J.; BRADY, J. F. Shear thickening in colloidal dispersions. **Physics Today**, American Institute of Physics, v. 62, n. 10, p. 27–32, 2009.
- 94 SYRAKOS, A.; GEORGIU, G. C.; ALEXANDROU, A. N. Solution of the square lid-driven cavity flow of a bingham plastic using the finite volume method. **Journal of Non-Newtonian Fluid Mechanics**, Elsevier, v. 195, p. 19–31, 2013.
- 95 SWAMEE, P. K.; AGGARWAL, N. Explicit equations for laminar flow of bingham plastic fluids. **Journal of Petroleum Science and Engineering**, Elsevier, v. 76, n. 3-4, p. 178–184, 2011.
- 96 BIRD, R. B.; ARMSTRONG, R. C.; HASSAGER, O. Dynamics of polymeric liquids. vol. 1: Fluid mechanics. John Wiley and Sons Inc., New York, NY, 1987.
- 97 MIGHRI, F.; AJJI, A.; CARREAU, P. Influence of elastic properties on drop deformation in elongational flow. **Journal of rheology**, The Society of Rheology, v. 41, n. 5, p. 1183–1201, 1997.
- 98 DELGADO, M. et al. Experimental study of grease flow in pipelines: wall slip and air entrainment effects. **Chemical Engineering and Processing: Process Intensification**, Elsevier, v. 44, n. 7, p. 805–817, 2005.
- 99 BINGHAM, E. C. **Fluidity and plasticity**. [S.l.]: McGraw-Hill, 1922. v. 2.
- 100 BLACKWELL, B. C.; EWOLDT, R. H. A simple thixotropic–viscoelastic constitutive model produces unique signatures in large-amplitude oscillatory shear (laos). **Journal of Non-Newtonian Fluid Mechanics**, Elsevier, v. 208, p. 27–41, 2014.
- 101 BARNES, H. A. Thixotropy—a review. **Journal of Non-Newtonian fluid mechanics**, Elsevier, v. 70, n. 1-2, p. 1–33, 1997.

- 102 LARSON, R. Constitutive equations for thixotropic fluids. **Journal of Rheology**, Society of Rheology, v. 59, n. 3, p. 595–611, 2015.
- 103 MEWIS, J. Thixotropy-a general review. **Journal of Non-Newtonian Fluid Mechanics**, Elsevier, v. 6, n. 1, p. 1–20, 1979.
- 104 TANNER, R. I.; WALTERS, K. **Rheology: an historical perspective**. [S.l.]: Elsevier, 1998. v. 7.
- 105 OATES, K. M. et al. Rheology of synovial fluid and protein aggregation. **Journal of the royal society interface**, The Royal Society London, v. 3, n. 6, p. 167–174, 2006.
- 106 FERRY, J. D. **Viscoelastic properties of polymers**. [S.l.]: John Wiley & Sons, 1980.
- 107 LAKES, R.; LAKES, R. S. **Viscoelastic materials**. [S.l.]: Cambridge university press, 2009.
- 108 LAUN, H. M. Capillary rheometry for polymer melts revisited. **Rheologica acta**, Springer, v. 43, n. 5, p. 509–528, 2004.
- 109 ARIFF, Z. M. et al. Rheological behaviour of polypropylene through extrusion and capillary rheometry. **Polypropylene**, InTech Rijeka, Croatia, p. 29–49, 2012.
- 110 OSSWALD, T.; RUDOLPH, N. Polymer rheology. **Carl Hanser, München**, 2015.
- 111 EVAGELIOU, V. Shear and extensional rheology of selected polysaccharides. **International Journal of Food Science & Technology**, Wiley Online Library, v. 55, n. 5, p. 1853–1861, 2020.
- 112 CARDOSO, F. et al. Characterisation of rendering mortars by squeeze-flow and rotational rheometry. **Cement and concrete research**, Elsevier, v. 57, p. 79–87, 2014.
- 113 SILVA, P. H. de L. et al. Rheology of thf hydrate slurries at high pressure. **Oil & Gas Science and Technology–Revue d'IFP Energies nouvelles**, EDP Sciences, v. 75, p. 16, 2020.
- 114 CHARIN, R. M.; SUM, A. K. Steady-state and transient studies of gas hydrates formation in non-emulsifying oil systems. **Energy & Fuels**, ACS Publications, v. 31, n. 3, p. 2548–2556, 2017.
- 115 WEBB, E. B. et al. High-pressure rheology of hydrate slurries formed from water-in-oil emulsions. **Energy & fuels**, ACS Publications, v. 26, n. 6, p. 3504–3509, 2012.
- 116 BASSANI, C. L. et al. A multiscale approach for gas hydrates considering structure, agglomeration, and transportability under multiphase flow conditions: I. phenomenological model. **Industrial & Engineering Chemistry Research**, ACS Publications, v. 58, n. 31, p. 14446–14461, 2019.

- 117 MELCHUNA, A. et al. Topological modeling of methane hydrate crystallization from low to high water cut emulsion systems. **Fluid Phase Equilibria**, Elsevier, v. 413, p. 158–169, 2016.
- 118 JOSHI, S. V. et al. Experimental flowloop investigations of gas hydrate formation in high water cut systems. **Chemical Engineering Science**, Elsevier, v. 97, p. 198–209, 2013.
- 119 LIM, V. W. et al. Subcooling and induction time measurements of probabilistic hydrate formation. In: ONEPETRO. **Offshore Technology Conference Asia**. [S.l.], 2018.
- 120 ZHENG, H. et al. Induction time of hydrate formation in water-in-oil emulsions. **Industrial & Engineering Chemistry Research**, ACS Publications, v. 56, n. 29, p. 8330–8339, 2017.
- 121 DOUÏEB, S. et al. Effect of the fluid shear rate on the induction time of co₂-thf hydrate formation. **The Canadian Journal of Chemical Engineering**, Wiley Online Library, v. 95, n. 1, p. 187–198, 2017.
- 122 MUHLSTEDT, G. et al. Rheological properties of hydrate slurry in the water-based drilling fluid. **Energy & Fuels**, ACS Publications, v. 35, n. 13, p. 10488–10497, 2021.
- 123 ROGERS, R. D.; VOTH, G. A. Ionic liquids. **Accounts of chemical research**, ACS Publications, v. 40, n. 11, p. 1077–1078, 2007.
- 124 MACFARLANE, D. R.; SEDDON, K. R. Ionic liquids—progress on the fundamental issues. **Australian journal of chemistry**, CSIRO Publishing, v. 60, n. 1, p. 3–5, 2007.
- 125 KARANJKAR, P. U. et al. Rheology of cyclopentane hydrate slurry in a model oil-continuous emulsion. **Rheologica Acta**, Springer, v. 55, n. 3, p. 235–243, 2016.
- 126 KILPATRICK, P. K. Water-in-crude oil emulsion stabilization: review and unanswered questions. **Energy & Fuels**, ACS Publications, v. 26, n. 7, p. 4017–4026, 2012.
- 127 YARRANTON, H.; URRUTIA, P.; SZTUKOWSKI, D. Effect of interfacial rheology on model emulsion coalescence: li. emulsion coalescence. **Journal of colloid and interface science**, Elsevier, v. 310, n. 1, p. 253–259, 2007.
- 128 YARRANTON, H. W.; SZTUKOWSKI, D. M.; URRUTIA, P. Effect of interfacial rheology on model emulsion coalescence: I. interfacial rheology. **Journal of colloid and interface science**, Elsevier, v. 310, n. 1, p. 246–252, 2007.
- 129 PERRY, R. B. Principles of colloid and surface chemistry, (hiemenz, pc). **Journal of Chemical Education**, ACS Publications, v. 64, n. 12, p. A328, 1987.
- 130 TADROS, T. F. **Formulation of disperse systems: Science and Technology**. [S.l.]: John Wiley & Sons, 2014.

- 131 LIU, C. et al. Rheology of water-in-oil emulsions with different drop sizes. **Journal of Dispersion Science and Technology**, Taylor & Francis, v. 37, n. 3, p. 333–344, 2016.
- 132 GOODARZI, F.; ZENDEHBOUDI, S. A comprehensive review on emulsions and emulsion stability in chemical and energy industries. **The Canadian Journal of Chemical Engineering**, Wiley Online Library, v. 97, n. 1, p. 281–309, 2019.
- 133 UMAR, A. A. et al. A review of petroleum emulsions and recent progress on water-in-crude oil emulsions stabilized by natural surfactants and solids. **Journal of Petroleum Science and Engineering**, Elsevier, v. 165, p. 673–690, 2018.
- 134 DALMAZZONE, C. et al. Development of a methodology for the optimization of dehydration of extraheavy-oil emulsions. **SPE Journal**, OnePetro, v. 15, n. 03, p. 726–736, 2010.
- 135 KOKAL, S.; AL-JURAIID, J. Reducing emulsion problems by controlling asphaltene solubility and precipitation. In: ONEPETRO. **SPE Annual Technical Conference and Exhibition**. [S.l.], 1998.
- 136 MENON, V.; WASAN, D. Particle—fluid interactions with applications to solid-stabilized emulsions part iii. asphaltene adsorption in the presence of quinaldine and 1, 2-dimethylindole. **Colloids and surfaces**, Elsevier, v. 23, n. 4, p. 353–362, 1987.
- 137 BINKS, B. P.; DONG, J.; REBOLJ, N. Equilibrium phase behaviour and emulsion stability in silicone oil+ water+ aot mixtures. **Physical Chemistry Chemical Physics**, Royal Society of Chemistry, v. 1, n. 9, p. 2335–2344, 1999.
- 138 MALDONADO-VALDERRAMA, J.; PATINO, J. M. R. Interfacial rheology of protein–surfactant mixtures. **Current Opinion in Colloid & Interface Science**, Elsevier, v. 15, n. 4, p. 271–282, 2010.
- 139 DICKINSON, E. Hydrocolloids as emulsifiers and emulsion stabilizers. **Food hydrocolloids**, Elsevier, v. 23, n. 6, p. 1473–1482, 2009.
- 140 URBINA-VILLALBA, G. et al. Influence of flocculation and coalescence on the evolution of the average radius of an o/w emulsion. is a linear slope of r [combining macron] ³ vs. t an unmistakable signature of ostwald ripening? **Physical Chemistry Chemical Physics**, Royal Society of Chemistry, v. 11, n. 47, p. 11184–11195, 2009.
- 141 PEIXINHO, J. et al. Rheology of hydrate forming emulsions. **Langmuir**, ACS Publications, v. 26, n. 14, p. 11699–11704, 2010.
- 142 SCHRAMM, L. L. **Emulsions, foams, and suspensions: fundamentals and applications**. [S.l.]: John Wiley & Sons, 2006.
- 143 DUKHIN, A.; GOETZ, P. Evolution of water-in-oil emulsion controlled by droplet-bulk ion exchange: acoustic, electroacoustic, conductivity and image analysis. **Colloids and Surfaces A: Physicochemical and Engineering Aspects**, Elsevier, v. 253, n. 1-3, p. 51–64, 2005.

- 144 CHRISMAN, E.; LIMA, V.; MENECHINI, P. Asphaltenes—problems and solutions in e&p of brazilian crude oils. **Abdel-Raouf, ME-S. Crude Oil Emulsions-Composition Stability and Characterization**. London: **IntechOpen**, v. 2, p. 1–26, 2012.
- 145 BARNES, H. A.; NGUYEN, Q. D. Rotating vane rheometry—a review. **Journal of non-Newtonian fluid mechanics**, Elsevier, v. 98, n. 1, p. 1–14, 2001.
- 146 WRIGHT, P. The variation of viscosity with temperature. **Physics Education**, IOP Publishing, v. 12, n. 5, p. 323, 1977.
- 147 SCHMELZER, J. W.; ZANOTTO, E. D.; FOKIN, V. M. Pressure dependence of viscosity. **The Journal of chemical physics**, American Institute of Physics, v. 122, n. 7, p. 074511, 2005.
- 148 GUERRA, A. et al. Dynamic viscosity of methane and carbon dioxide hydrate systems from pure water at high-pressure driving forces. **Chemical Engineering Science**, Elsevier, v. 252, p. 117282, 2022.
- 149 SA, J.-H.; SUM, A. K. Promoting gas hydrate formation with ice-nucleating additives for hydrate-based applications. **Applied Energy**, Elsevier, v. 251, p. 113352, 2019.
- 150 LI, S.-L. et al. Factors controlling hydrate film growth at water/oil interfaces. **Chemical Engineering Science**, Elsevier, v. 135, p. 412–420, 2015.
- 151 LIU, Y. et al. Investigation of hydrate agglomeration and plugging mechanism in low-wax-content water-in-oil emulsion systems. **Energy & Fuels**, ACS Publications, v. 32, n. 9, p. 8986–9000, 2018.
- 152 SANDOVAL, G. A. et al. A rheological study of parameters that influence the formation of cyclopentane hydrates. **Energy & Fuels**, ACS Publications, v. 35, n. 22, p. 18467–18477, 2021.
- 153 WEBB, E. B.; KOH, C. A.; LIBERATORE, M. W. Rheological properties of methane hydrate slurries formed from aot+ water+ oil microemulsions. **Langmuir**, ACS Publications, v. 29, n. 35, p. 10997–11004, 2013.
- 154 WEBB, E. B.; KOH, C. A.; LIBERATORE, M. W. High pressure rheology of hydrate slurries formed from water-in-mineral oil emulsions. **Industrial & Engineering Chemistry Research**, ACS Publications, v. 53, n. 17, p. 6998–7007, 2014.
- 155 PANDEY, G.; SANGWAI, J. S. High pressure rheological studies of methane hydrate slurries formed from water-hexane, water-heptane, and water-decane multiphase systems. **Journal of Natural Gas Science and Engineering**, Elsevier, v. 81, p. 103365, 2020.
- 156 ARJMANDI, M. et al. Is subcooling the right driving force for testing low-dosage hydrate inhibitors? **Chemical engineering science**, Elsevier, v. 60, n. 5, p. 1313–1321, 2005.

- 157 ANKLAM, M. R.; FIROOZABADI, A. Driving force and composition for multicomponent gas hydrate nucleation from supersaturated aqueous solutions. **The Journal of chemical physics**, American Institute of Physics, v. 121, n. 23, p. 11867–11875, 2004.
- 158 ANDERECK, C. D.; LIU, S.; SWINNEY, H. L. Flow regimes in a circular couette system with independently rotating cylinders. **Journal of fluid mechanics**, Cambridge University Press, v. 164, p. 155–183, 1986.
- 159 DING, L. et al. Rheology of natural gas hydrate slurry: Effect of hydrate agglomeration and deposition. **Fuel**, Elsevier, v. 239, p. 126–137, 2019.
- 160 TANAKA, R.; SAKEMOTO, R.; OHMURA, R. Crystal growth of clathrate hydrates formed at the interface of liquid water and gaseous methane, ethane, or propane: variations in crystal morphology. **Crystal Growth and Design**, ACS Publications, v. 9, n. 5, p. 2529–2536, 2009.
- 161 SILVA, P. H. de L. et al. Rheology of tetrahydrofuran hydrate slurries. **Energy & Fuels**, ACS Publications, v. 31, n. 12, p. 14385–14392, 2017.
- 162 BARNES, H. A. **A handbook of elementary rheology**. [S.l.]: University of Wales, Institute of Non-Newtonian Fluid Mechanics Aberystwyth, 2000. v. 1.
- 163 YANG, S.-o. et al. Temperature dependence of particle–particle adherence forces in ice and clathrate hydrates. **Journal of colloid and interface science**, Elsevier, v. 277, n. 2, p. 335–341, 2004.
- 164 MAJID, A. A.; WU, D. T.; KOH, C. A. New in situ measurements of the viscosity of gas clathrate hydrate slurries formed from model water-in-oil emulsions. **Langmuir**, ACS Publications, v. 33, n. 42, p. 11436–11445, 2017.
- 165 AHUJA, A.; ZYLYFTARI, G.; MORRIS, J. F. Yield stress measurements of cyclopentane hydrate slurry. **Journal of Non-Newtonian Fluid Mechanics**, Elsevier, v. 220, p. 116–125, 2015.
- 166 SUN, X. et al. A new model for hydrodynamics and mass transfer of hydrated bubble rising in deep water. **Chemical Engineering Science**, Elsevier, v. 173, p. 168–178, 2017.
- 167 LEGNANI, A. et al. Waxy oils: deformation-dependent materials. **Journal of Non-Newtonian Fluid Mechanics**, Elsevier, v. 285, p. 104378, 2020.
- 168 KAKITANI, C. et al. Measurements of hydrate formation behavior in shut-in and restart conditions. **Energy & Fuels**, ACS Publications, v. 33, n. 10, p. 9457–9465, 2019.